Charge Radii Measurements of Chromium Nuclei by Laser Spectroscopy at IGISOL-IV

Submitted in fulfillment of the requirements

of

Doctorate of Philosophy

in

Nuclear Physics

Ross Alexander Mathieson

Under the supervision of

Professor Bradley Cheal

Department of Physics

School of Physical Sciences

University of Liverpool

June 8, 2023

Acknowledgements

There are so many people that I would like to acknowledge for their contribution to my post-graduate experience: Professor Bradley Cheal, Dr Charlie Devlin, the Nuclear Group at Liverpool, the JYFL collaboration, the PHYS106 team, my friends both in the PhD office and at home in Sheffield, and of course my mum and dad.

Reflecting upon my time at Liverpool, I struggle to put into words how fortunate I feel to have worked with such amazing people, and as such, I will keep my acknowledgements brief. Without the support, guidance, and friendship of everybody mentioned above, I would not be where I am today, and for that, I am incredibly grateful to all of you.

Once again, thank you.

"A day can really slip by when you're deliberately avoiding what you're supposed to do."

– Calvin, Calvin and Hobbes.

Abstract

This thesis presents the results of an experiment in which high-precision measurements of the atomic hyperfine structure of chromium isotopes were made via an experimental technique known as collinear laser spectroscopy. This thesis presents the previously unknown changes in nuclear mean-square charge radii relative to stable ^{52}Cr for three isotopes of chromium: ^{48}Cr, ^{49}Cr, and ^{51}Cr. Additionally, the changes in mean-square charge radii relative to ^{52}Cr for the stable isotopes of chromium (^{50}Cr, ^{53}Cr, and ^{54}Cr) have been remeasured, as have the magnetic dipole moments of the odd-A chromium isotopes mentioned above.

For the first time laser spectroscopy experiments have been performed on unstable isotopes of chromium. All measurements made during this work were performed at the IGISOL-IV facility at the University of Jyväskylä, Finland. This experimental operation was formed of three individual campaigns: an initial offline campaign performed to determine the spectroscopic efficiencies of several atomic transitions in chromium; the main online campaign during which measurements of both the short-lived and stable isotopes of chromium were made on two lines: the 358 nm ($3d^5$ $(^6S)4s$ $^7S_3 \rightarrow 3d^4$ $(^5D)4s4p(^3P)$ $^7P_4$) and 425 nm ($3d^5$ $(^6S)4s$ $^7S_3 \rightarrow 3d^5$ $(^6S)4p$ $^7P_4$) atomic transitions; a second offline campaign during which additional measurements of the stable isotopes were made on the 425 nm line.

The trends in the changes of mean-square charge radii for isotopes of chromium, titanium, and calcium, relative to their $N = 28$ isotope are compared, and from the available data, it is shown that the magnitude of odd-even staggering along each isotope chain decreases as pairs of protons are added to the $1f_{7/2}$ orbital. The newly obtained changes in mean-square charge radii are then compared to recently published, theoretical predictions made using state-of-the-art ab-initio and density functional theory calculations, which were developed to model the previously observed regional systematics.

Contents

List of Figures

List of Tables

Chapter 1

Introduction

Nuclear physics is one of the cornerstones of modern physics. With applications spanning from diagnosis and treatment of disease to radio-dating in archaeology, energy production via nuclear power, and defence, it is clear that the underlying importance of nuclear research for society cannot be understated. These applications of nuclear physics could not have been developed if not for the extensive research already performed by physicists working to achieve a better understanding of nuclear phenomena, and in turn, the fundamental interactions that bind a nucleus together.

The basis of all scientific endeavour is experimentation, and nuclear physics is no exception. The field itself is organised into many different, but inter-related disciplines, for example, those which relate to measuring the disintegration of nuclei such as decay spectroscopy, and those which are concerned with measuring the properties of a nucleus in a given state: notably high precision mass measurements and optical spectroscopy techniques like those employed in this work.

1.1 Laser Spectroscopy in Nuclear Physics Research

The work reported in this thesis is based on an experimental technique known as laser spectroscopy, an incredibly powerful tool available to nuclear physicists, which allows for model-independent determination of four nuclear properties: the magnetic dipole moment, the spectroscopic electric quadrupole moment, the change in mean-square charge radius relative to another isotope, and the nuclear spin [1].

In order to understand the phenomenology of nuclear systems, it is imperative that the struc-

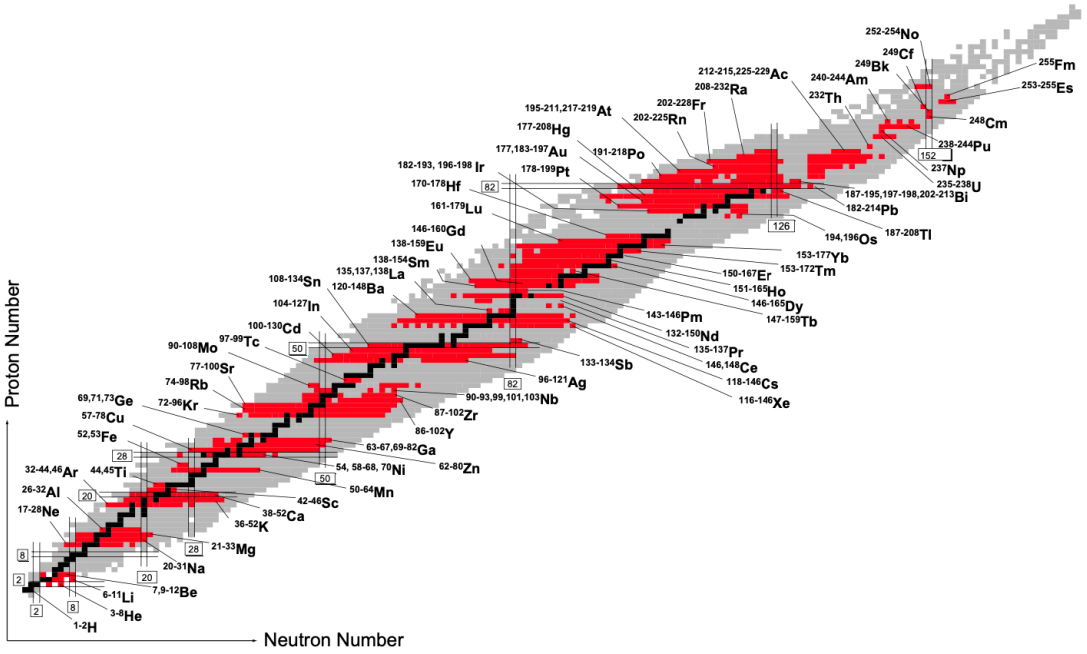

Figure 1.1: A diagram showing all of the known nuclides. Black squares represent stable nuclides, grey squares represent the known radioactive nuclides, and red squares represent radioactive isotopes which have been investigated by online optical spectroscopy experiments as of September 2022 [2].

ture of both stable and radioactive nuclei are studied. One of the challenges of studying these radioactive isotopes is that they often have very short half-lives, and as such, it may be difficult to isolate a sufficient number of them to prepare a sample in a given period of time to be studied before they decay. Radioactive ion beam factories can be used to overcome this challenge by producing short-lived isotopes of interest onsite and delivering them to an appropriate experimental station almost instantaneously. Figure 1.1 shows which isotopes have been investigated using online optical spectroscopy techniques. It is clear that optical spectroscopy techniques are very successful at studying nuclei far from stability, but that there are also gaps along the chart of nuclides where studies have yet to take place, for example, the elements spanning calcium to nickel.

Laser spectroscopy experiments are performed at facilities across the globe (see figure 1.2), and the experimental data used in this work were obtained at the IGISOL-IV facility at the University of Jyväskylä, Finland, which houses an ISOL (Isotope Separator OnLine) facility and utilises a method of laser spectroscopy known as anti-collinear laser spectroscopy.

The purpose of this work is to investigate the evolution of nuclear properties in a region of the chart of nuclides spanning between $Z = 20$ and $Z = 28$, henceforth referred to as the calcium-nickel region, specifically changes of the charge-radii along the chromium isotope chain. There

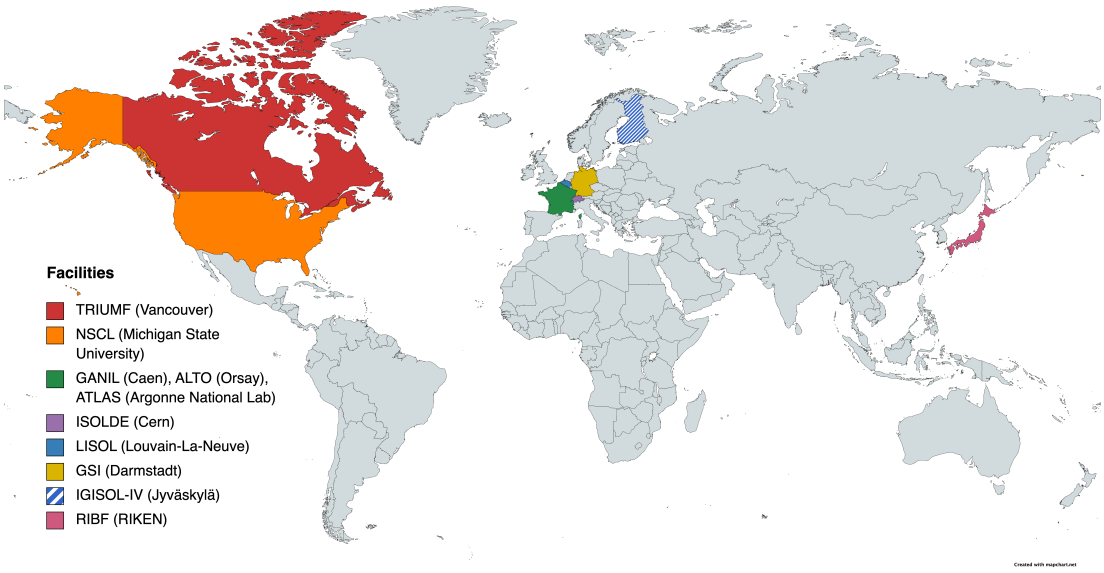

Figure 1.2: A map to show the nations home to facilities capable of performing laser spectroscopy experiments for nuclear structure studies as of 2010 [1].

is a very limited amount of experimental data available in this region, namely due to the difficulty in producing the refractory elements that form it, particularly the short-lived radioactive species. The isotope production method employed at IGISOL is able to overcome this hurdle, and as such a campaign is currently underway to make more spectroscopic measurements of these elements. Recent experimental runs include those for chromium (the focus of this work), iron, and cobalt.

A more detailed discussion of the behaviours observed in this region of the chart of nuclides is provided in the next sub-section, however, the main motivation of this work can be summarised very concisely: more experimental data, particularly relating to nuclear charge radii, is required to test and further develop the models currently used to describe the trends in nuclei properties observed between the $Z = 20$ and $Z = 28$ shell closures.

This thesis presents charge radii measurements of unstable isotopes of chromium for the first time, in addition to re-measurements of the nuclear magnetic dipole moments of ^{49}Cr and ^{51}Cr and the charge radii of the four stable isotopes of chromium. The charge radii and nuclear moments were calculated using isotope shifts and hyperfine parameters, respectively, these themselves being obtained through analysis of experimentally obtained hyperfine spectra. Table 1.1 presents the chromium isotopes investigated as part of this work.

Isotope (A)	$t_{1/2}$	Mole Fraction	$\langle r^2 \rangle$ (fm^2)	μ (μ_N)
48	21.56 h	-	new	-
49	42.3 m	-	new	re-measurement
50	stable	0.04345(13)	re-measurement	-
51	27.7015 d	-	new	re-measurement
52	stable	0.83789(18)	reference	-
53	stable	0.09501(17)	re-measurement	reference
54	stable	0.02365(7)	re-measurement	-

Table 1.1: A table to show the isotopes of chromium investigated in this work. The table outlines which properties are being reported for the first time and which are re-measurements or were used as references. It is not possible to determine the magnetic moment of even-A isotopes due to their lack of nuclear spin. Half-lives are taken from the NUBASE2020 evaluation of nuclear physics properties [3], and mole fractions are taken from de Laeter *et al.* [4].

1.2 Physics Motivation

The calcium-nickel region has been sparsely explored, particularly as one approaches the $N = 20$ neutron shell closure. That being said, the limited data available for this region is very interesting. For example, data obtained from recent laser spectroscopy experiments on neutron-rich calcium isotopes at ISOLDE, CERN [5] and proton-rich calcium isotopes at Michigan State University [6] have been added to the known mean-square charge radii, and the isotope chain now extends beyond both of the doubly-magic calcium nuclei. This isotope chain is the only one in the region for which charge radii measurements have been made across both the $N = 20$ and $N = 28$ shell closures. The observed trend in the charge radii, which follow a parabola between the two shell closures, is as far as we know, unique to the calcium isotope chain. Figure 1.3 shows that below the $N = 28$ neutron shell closure, the proton dependence of the charge radii for nuclei in the region is significant, whereas, above the shell closure, there is little dependence.

As can be seen in figure 1.3, each of the $N = 28$ isotones in the calcium-nickel region exhibits enhanced shell-closure effects: a kink in the course of the charge radii is observed as one crosses the shell closure. Above this shell closure, the changes in mean-square charge radii appear to increase steeply and relatively uniformly for each isotope chain, regardless of the number of protons. This trend of steadily and steeply increasing charge radii above shell closures is observed in other regions of the chart of nuclides, for example, the $N = 50, 82$ shell closures. The uniformity of the increase in the charge radii above the $N = 28$ shell closure is explained in the work of Kreim *et al.* [7] when reporting on the charge radii of potassium isotopes: above the shell closure, neutrons fill the $2p_{3/2}$ orbital and the increase in charge radii is dependent wholly

on the collective polarization of the protons by the neutrons, rather than by any particular configuration of protons.

An understanding of regional systematics developed by means of experimentation is invaluable as it allows for cogent predictions of the properties of other nuclei in the region to be made based on a minimal number of assumptions. For example, in the work of Heylen *et al.* [8], when determining the experimental charge radii along the manganese isotope chain from isotope shift measurements, it was not possible to perform a King plot analysis using non-optical data to calibrate the atomic parameters due to the lack of known charge radii. The absolute charge radius of only one isotope of manganese is known from non-optical methods. Accordingly, it was necessary to take a theoretical approach to calculate appropriate atomic parameters: these often have large uncertainties (mainly that associated with the mass shift factor), which are carried through to the calculated charge radii. As each isotope chain measured above the $N = 28$ shell closure appears to follow the same trend, and there is a consensus as to why this is, it was possible to explore what changes could be made to the theoretically determined atomic parameters to ensure the best agreement between the changes in charge radii along the manganese isotope chain and those of neighbouring isotope chains. This pseudo-calibration showed that by scaling the atomic mass shift factor by 1.05, the changes of the manganese charge radii then closely mirrored those in neighbouring isotope chains immediately after the $N = 28$ shell closure. A similar issue to that discussed above will be encountered during the studies of cobalt and vanadium, therefore understanding the regional systematics is pertinent and falls within the scope of the work performed here.

As one moves into the $1f_{7/2}$ neutron shell, the calcium charge radii follow a parabolic trend: moving from the $N = 28$ shell closure to the mid-shell the charge radii increase, moving from the mid shell to the $N = 20$ shell closure they decrease. It is noteworthy that ^{40}Ca and ^{48}Ca have the same charge radii despite the latter nucleus containing eight additional nucleons. The parabolic trend in charge radii is also present in the $Z < 20$ isotope chains, but with the $N = 20$ isotopes smaller than at $N = 28$. It is not presently possible to conclude whether or not the observed parabolic trend persists as proton occupation of the $1f_{7/2}$ orbital increases for even-Z elements; the charge radii of titanium isotopes generally appear to increase as one moves to lower neutron numbers and the chain does not exhibit any sign of being parabolic.

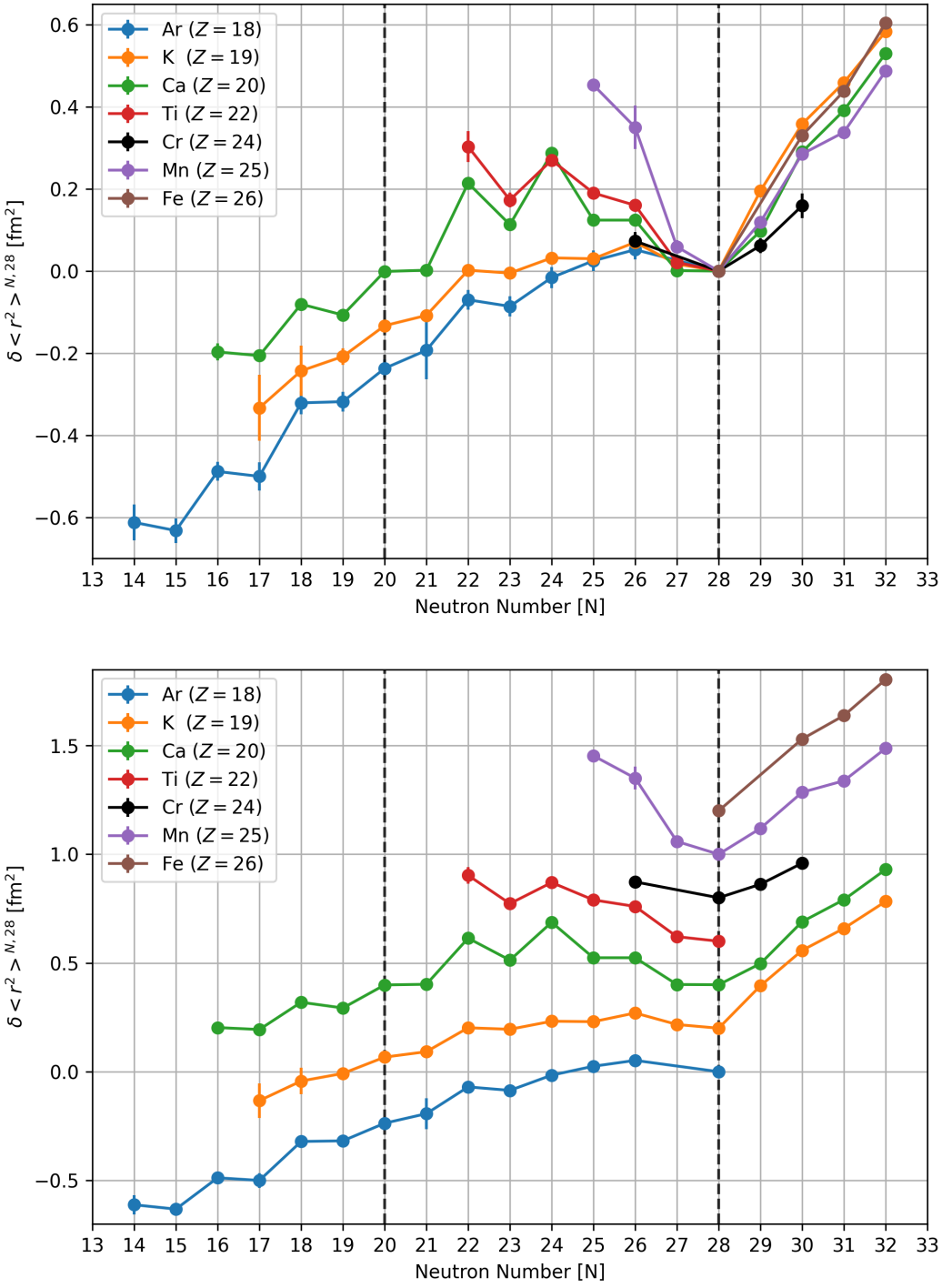

Figure 1.3: Top: A plot to show the changes in means square charge radii of various isotopes in the calcium-nickel region. Bottom: The same plot as above with an arbitrary offset applied to better visualise trends. The dashed lines represent the $N = 20$ and $N = 28$ shell neutron closures. Statistical errors are presented where the reference material reported both statistical and systematic uncertainties. Values obtained from Koszorus *et al.* [9] (K), Garcia Ruiz *et al.* [5] (Ca), Miller *et al.* [6] (Ca), Aufmuth *et al.* [10] (Cr), Heylen *et al* [8] (Mn), and Angeli and Marinova [11].

In addition to the parabola, the trend in calcium charge radii shows significant odd-even staggering (OES). This is the phenomenon where the even-A nuclei along an isotope chain have a larger charge radius than the average of their odd-A neighbours, resulting in deviations from a smooth pattern in the charge radii. A blocking effect in odd-N nuclei leads to a reduced neutron pairing density, which affects the proton pairing density and thus the charge radius. This odd-even staggering pattern is not unique to the calcium isotope chain, it is observed across the nuclear chart and in this region is exhibited in the argon ($Z = 18$), potassium ($Z = 19$), scandium ($Z = 21$), and titanium ($Z = 22$) isotope chains. The magnitude of the staggering is enhanced in the even-Z chains and appears to be the most pronounced in the calcium chain. At present, there is insufficient data to determine how the odd-even staggering evolves as a function of increasing proton number in even-Z isotopes.

Following from the discussion above, it becomes apparent that additional charge radii measurements are required to better understand the behaviours observed in the calcium-nickel region. Chromium, which has a half-full $1f_{7/2}$ proton shell, is an ideal candidate for study. Only the four stable isotopes of chromium have known charge radii, but the trend observed deviates from those of the calcium and titanium isotope chains: the slope of the charge radii is much steeper for these elements as one moves to either side of the shell closure. Moreover, with measurements of neutron-deficient chromium isotopes it will become possible to compare the magnitude of any odd-even staggering to that observed in the calcium and titanium chains.

Moreover, the scope of this work includes determining the charge-radius of the self-conjugate nucleus ^{48}Cr. Self-conjugate nuclei such as this may be used to investigate isospin pairing mechanisms within nuclear systems. A consequence of isospin pairing is that the proton-neutron pair of an odd-odd, $N = Z$ nucleus should behave the same as a like-nucleon pair in an even-even $N = Z$ nucleus if both are in the $T = 1$ ($I = 0$) state. This charge-independent pairing of nucleons is a prominent feature of shell model calculations, however, proton-neutron pairing interactions remain an area of research interest as mean-field descriptions of the nucleus continue to be developed. The experimentally determined charge radii of these types of nuclei may be used to verify the charge independence of this nucleon pairing mechanism. For example, if one were to plot the change in mean-square charge radius (relative to an arbitrary nuclide) of $N = Z$ isotopes, the $T = 1$ ($I = 0$) state of an odd-odd nucleus should lie exactly on the line connecting the $T = 1$ ($I = 0$) states of its even-even neighbours. Recent studies investigating these types of nuclei in the calcium-nickel region include those of Bissell *et al.* [12] and Koszorus *et al.* [13], which established this was in fact the case for ^{38}K and ^{42}Sc, respectively. The

determination of the charge radius of ^{48}Cr would add to the data available when developing our understanding of these pairing mechanisms by acting as one of the even-even anchor points for the self-conjugate isotopes of vanadium and manganese.

Finally, new measurements can be used to test the ability of the Density Functional Theory (DFT) to accurately reproduce the charge radii of nuclei. This functional theory approach is at the forefront of research being performed in the field at present and has been tested in studies spanning many different regions of the nuclear chart. DFT has proven to be able to successfully predict the charge radii of cadmium (2018) [14], calcium (2019) [6], tin (2019) [15], and copper (2020) [16], and has shown limited success when being used to model exotic nuclei such as neutron-rich isotopes of potassium [9] (2021), and deformed open-shell nuclei such as palladium [17] (2022). For example, in the investigation of exotic potassium nuclei performed by Koszorus *et al.* [9], DFT was only able to reproduce global trends rather than accurately determine the individual charge radii. In the work relating to palladium performed by Geldhof *et al.* [17], all the functionals tested were able to describe the parabolic trend of the measured charge radii, but each had its own limitation, for example, either underestimating the absolute charge radii, overestimating the magnitude of the odd-even staggering, or predicting odd-even staggering patterns opposite to those observed. It may be the case that due to the half-filled proton shell, deformation becomes a more significant driver in the evolution of the chromium charge radii. If the chromium nuclei exhibit significant deformation, as would be indicated by the electric quadrupole moments or alternatively the mean-square charge radii measured, this work would provide an excellent testbed for further evaluation of this theoretical approach for modelling the nucleus.

Chapter 2

Nuclear Models

In 1909 Hans Geiger and Ernest Marsden performed the famous "Gold Foil Experiment". The experiment measured the angular distribution of alpha particles deflected by the atoms within a piece of gold foil. It was observed that a small number of the alpha particles were deflected through large angles, and in some instances, back towards the direction they came from [18]. This observation could not be explained using the model of the atom accepted at the time - the plum-pudding model proposed by Sir Joseph John Thompson. In 1911, Ernest Rutherford proposed a new model of the atom to be able to explain this observation, known now as the Rutherford model. The Rutherford model assumed that the atom is mainly empty space and that the majority of the mass of the atom is contained within a central, positively charged body, surrounded by a distribution of electrons [19]. Thus the nuclear model of the atom was born.

The discovery of the nucleus was one of the most significant discoveries of early 20th-century physics and marked the start of a novel branch of physics: nuclear physics. Our understanding of the nucleus has continued to evolve since its discovery, and so have the many models used to describe it. Three of the most important are discussed in this chapter: the liquid drop model, the single particle spherical-shell model, and the deformed shell model, known as the Nilsson model. There will also be a brief discussion of two contemporary theories: the ab-initio approach, and density functional theories.

2.1 The Liquid Drop Model

The liquid drop model and related semi-empirical mass formula are used to describe global trends in nuclear size, mass and binding energy. The model assumes that the nucleus can be described as an incompressible droplet of nuclear fluid [20].

To a first approximation the binding energy of the nucleus is proportional to the number of nucleons, A, thus $E_B \propto a_V A$ where a_v is the nuclear volume term:

$$E_B = a_v A. \tag{2.1.1}$$

Corrections to the binding energy must be made to replicate experimental findings. For example, if one assumed that each nucleon was attracted to every other nucleon, the binding energy would be proportional to $A(A-1)$, which is not the case. The binding energy appears to scale linearly with A, suggesting that a nucleon only interacts with its nearest neighbours. As such, additional corrections must be made as equation 2.1.1 to better replicate experimental data.

Equation 2.1.1 treats the contribution to binding energy by nucleons at the centre of the nucleus to be the same as those at the surface. This is not the case as nucleons on the surface of the nucleus have fewer neighbouring nucleons and are therefore less tightly bound to the nucleus. The number of nucleons at the surface scales with the surface area of the nucleus, which itself increases with $A^{2/3}$. Accordingly, the surface term correction, $a_s(A^{2/3})$, is subtracted from the binding energy:

$$E_B = a_v A - a_s(A^{2/3}). \tag{2.1.2}$$

A correction to account for the reduction in binding resulting from the Coulomb repulsion between protons must also be considered. As the electromagnetic force is a long-range interaction, the correction must account for all of the interactions between every proton with every other proton; hence the magnitude of this Coulomb correction scales with $Z(Z-1)$, and the binding energy equation becomes:

$$E_B = a_v A - a_s(A^{2/3}) - \frac{a_c Z(Z-1)}{A^{1/3}}. \tag{2.1.3}$$

A further consideration made for this model of nuclear binding accounts for the fact that for light, stable nuclei $Z \approx A/2$; this trend becomes less significant in heavier nuclei as the Coulomb repulsion rapidly increases and further neutrons are required to maintain stability. A symmetry correction accounts for this phenomenon by becoming increasingly weak as the proton number increases:

$$E_B = a_v A - a_s(A^{2/3}) - \frac{a_c Z(Z-1)}{A^{1/3}} - a_{sym} \cdot \frac{(A-2Z)^2}{A}. \tag{2.1.4}$$

The final correction to the binding energy formula is one which accounts for the fact that like nucleons preferentially pair together resulting in increased stability. An even-even nucleus will have additional binding energy as each proton and each neutron has a partner with whom to spin-couple, whereas an odd-odd nucleus will have reduced binding as there are two unpaired nucleons in this configuration (i.e. neither the odd proton nor odd neutron has a partner to spin-couple with). The final equation for binding energy becomes:

$$E_B = a_v A - a_s(A^{2/3}) - \frac{a_c Z(Z-1)}{A^{1/3}} - a_{sym} \cdot \frac{(A-2Z)^2}{A} \pm \delta. \tag{2.1.5}$$

The binding energy determination leads to the semi-empirical mass formula [20]:

$$M(Z,A) = Z m_{^1H} + N m_n - \frac{E_B}{c^2}, \tag{2.1.6}$$

where m_H is the mass of a ^{1}H atom, and m_n is the neutron mass.

Although the liquid drop model is successful in predicting the general trend of masses and binding energies, it fails to describe the sudden upticks in binding energies for nuclei with particular proton and neutron numbers - known as magic numbers. In order to understand these magic nuclei, a model which uses the teaching of quantum mechanics had to be developed. The inspiration of this new model builds upon the understanding of electron shells in atomic systems, which themselves are attributed to the observed peaks in the ionisation potentials of atoms.

2.2 The Single Particle Spherical Shell Model

The single particle model, also known as the nuclear shell model, takes a quantum mechanical approach to the description of the nucleus. Much like the model of atomic electrons, this model describes the nucleus in terms of orbitals at specific energies that can only house a particular number of particles. Furthermore, using this model the properties of the nucleus may be determined by looking only at the valence nucleon(s), as in this model the properties of the nucleus are dictated by the interactions between the valence nucleon and the average nuclear field produced by the rest of the nucleons which reside in fully occupied shells; again, this is analogous to the valence electron of an atom largely dictating the chemical properties of an element.

The single particle model is derived by solving the three-dimensional Schrödinger equation for a given potential, most commonly the Woods-Saxon potential [21], which has been modified to

correct for the nuclear spin-orbit interaction.

The Woods-Saxon potential is a spherical potential that takes the form:

$$V = \frac{V_0}{1 + e^{\frac{R - r_0}{a}}}, \tag{2.2.1}$$

where V_0 is the depth of the potential at the centre of the nucleus, a is the diffuseness parameter, and r_0 is the radius of the nucleus given by equation 2.2.2 [20]:

$$r_0 = 1.25 \times 10^{-15} \cdot A^{1/3}. \tag{2.2.2}$$

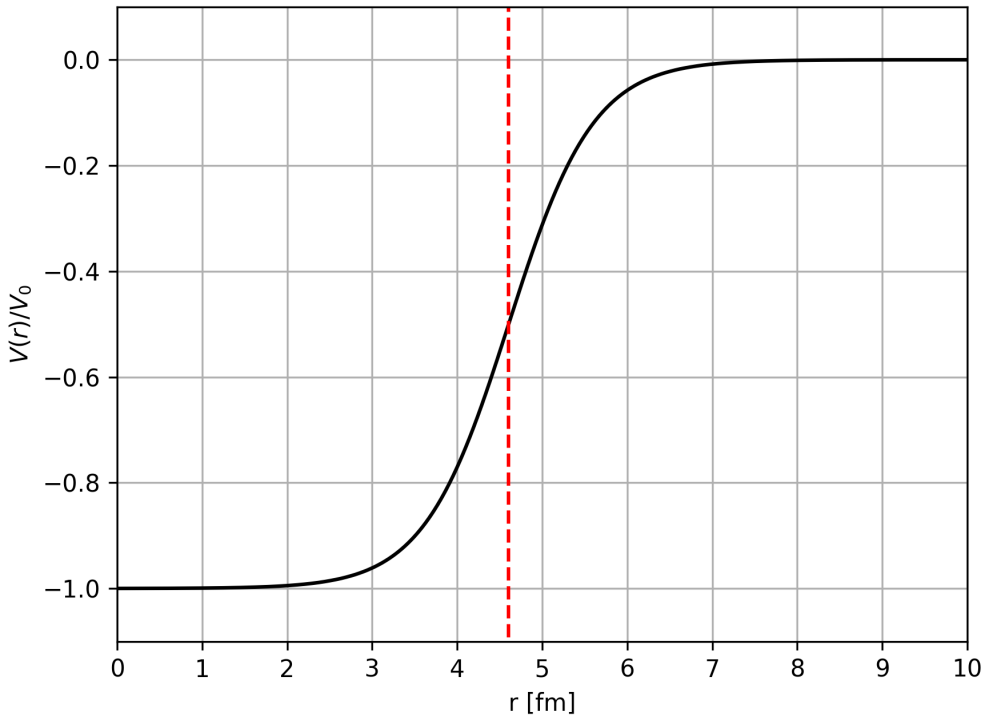

Figure 2.1: A plot of the Woods-Saxon potential (black curve) for a nucleus with $A = 50$ and $a = 0.5\,\text{fm}$, where the red line indicates R.

The modified spin-orbit potential, $V_{SO}\mathbf{l} \cdot \mathbf{s}$, increases the number of nuclear orbitals, and necessitates the adoption of atomic spectroscopic notation for individual orbitals to be easily referenced. Orbitals are referenced using their level number, n, orbital angular momentum, l, and total angular momentum, j.

For a nucleon with spin, $s = 1/2$, and orbital angular momentum, l, the possible j values are: $j = l + s$ and $j = l - s$. Therefore, for each value of orbital angular momentum, there are two

orbitals in which a nucleon can reside. The degeneracy of each orbital is given by $(2j + 1)$. These orbitals are referred to as spin-orbit doublets, and the energy separation between the doublet states is proportional to:

$$\langle l \cdot s \rangle_{j=l+1/2} - \langle l \cdot s \rangle_{j=l-1/2} = \frac{1}{2}(2l + 1)\hbar^2, \tag{2.2.3}$$

therefore, as l increases, so does the energy separation between the states of the doublet. When the spin-orbit potential is taken to be negative, the state with the larger total angular momentum is assigned a lower energy. This redistribution of states leads to a banded structure of states, known as shells, with large separations in energy between each shell. Fully occupied shells occur at the known magic numbers: 2, 8, 20, 28, 50, 82, and 126 [20]. Figure 2.2 illustrates how the spin-orbit correction leads to the emergence of the nuclear magic numbers.

The emergence of the nuclear magic numbers from the single particle model is remarkable, and the model has proven to be very successful at predicting and reproducing the properties of nuclei close to closed shells of nucleons. Evidence in support of the single particle model includes an above-average number of stable isotopes for $Z = 20$ and $Z = 50$ and isotones for $N = 50$ and $N = 82$, a relative increase in the binding energy per nucleon for magic nuclei, and sharp discontinuities in trends of two-neutron separation energies for magic nuclei [22].

There are limitations to the single particle model, for example away from closed shells where nuclear deformation is more prevalent (e.g. $150 < A < 194$), the single particle model is less successful at reproducing nuclear properties. This is because the model assumes a spherical nuclear potential and deformed nuclei have deformed potentials. In order to make accurate predictions of the properties of these deformed nuclei, a model that accounts for deformation needed to be developed.

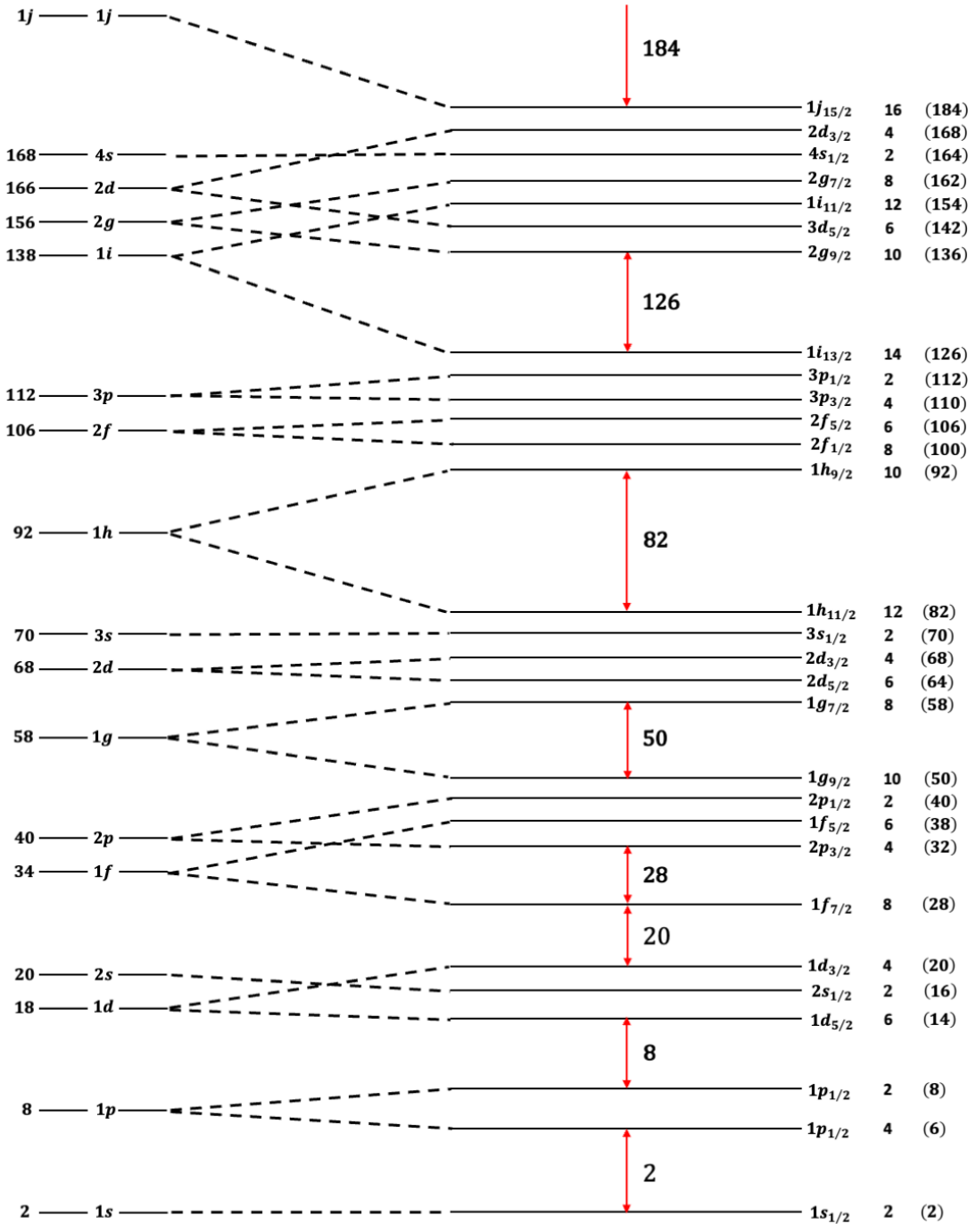

Figure 2.2: A visual representation of the shell model of the nucleus. The numbers on the far right represent the cumulative number of protons/neutrons as the orbitals are filled, the numbers second from the right show the degeneracy of each orbital, and the numbers between the shells represent the nuclear magic numbers.

2.3 The Nilsson Model

The Nilsson model, often referred to as the deformed single particle or deformed shell model, was formulated in the 1950s following the understanding of collective rotational motion in nuclei [23]. A spherical nucleus is unable to have rotational bands as a consequence of its symmetrical geometry, and thus, a spherical potential like the Woods-Saxon of the nuclear shell model is insufficient when describing deformed nuclei.

The potential used in the Nilsson model is an anisotropic oscillator potential, which has an axis of symmetry along the z axis. This potential is shaped similarly to that of a quadrupole-deformed nucleus and may be written as:

$$V(r) = \frac{1}{2}m(\omega_x^2 x^2 + \omega_y^2 y^2 + \omega_z^2 z^2) - C\mathbf{l}\cdot\mathbf{s} - D\mathbf{l}^2, \tag{2.3.1}$$

where the potential vibrates in the x, y and z directions with a frequency of ω_x, ω_y, and ω_z respectively, and where $\omega_x = \omega_y$ [24]. The volume of the nucleus is assumed to remain constant throughout the oscillations. The $C\mathbf{l}\cdot\mathbf{s}$ term accounts for the spin-orbit correction discussed previously, and the $D\mathbf{l}^2$ term is a correction added to flatten the potential well so that it better resembles the nuclear shape [25].

With reference to figure 2.3, it can be seen that the magnitude of the deformation parameter, denoted as ε_2 in this figure, heavily influences the structure of the nucleon orbitals, and that when the measure of deformation is greater than zero, the quantum number j is no longer a good quantum number. Instead, it is appropriate to use the individual projections of j onto the z axis, Ω, to describe nucleon orbitals, each of which has a maximum occupancy of either two protons or two neutrons. The complete notation to describe an orbital in the Nilsson scheme is $\Omega^\pi[Nn_3\Lambda]$, where:

$$\Lambda = l_z, \tag{2.3.2}$$

$$\Sigma = s_z = \pm\frac{1}{2}, \tag{2.3.3}$$

$$\Omega = j_z, = \Lambda + \Sigma, \tag{2.3.4}$$

$$\pi = (-1)^l \text{ or } (-1)^N, \tag{2.3.5}$$

$$N = n_1 + n_2 + n_3. \tag{2.3.6}$$

N is the oscillator quantum number and $n_{1,2,3}$ denote the x, y and z axes components of N.

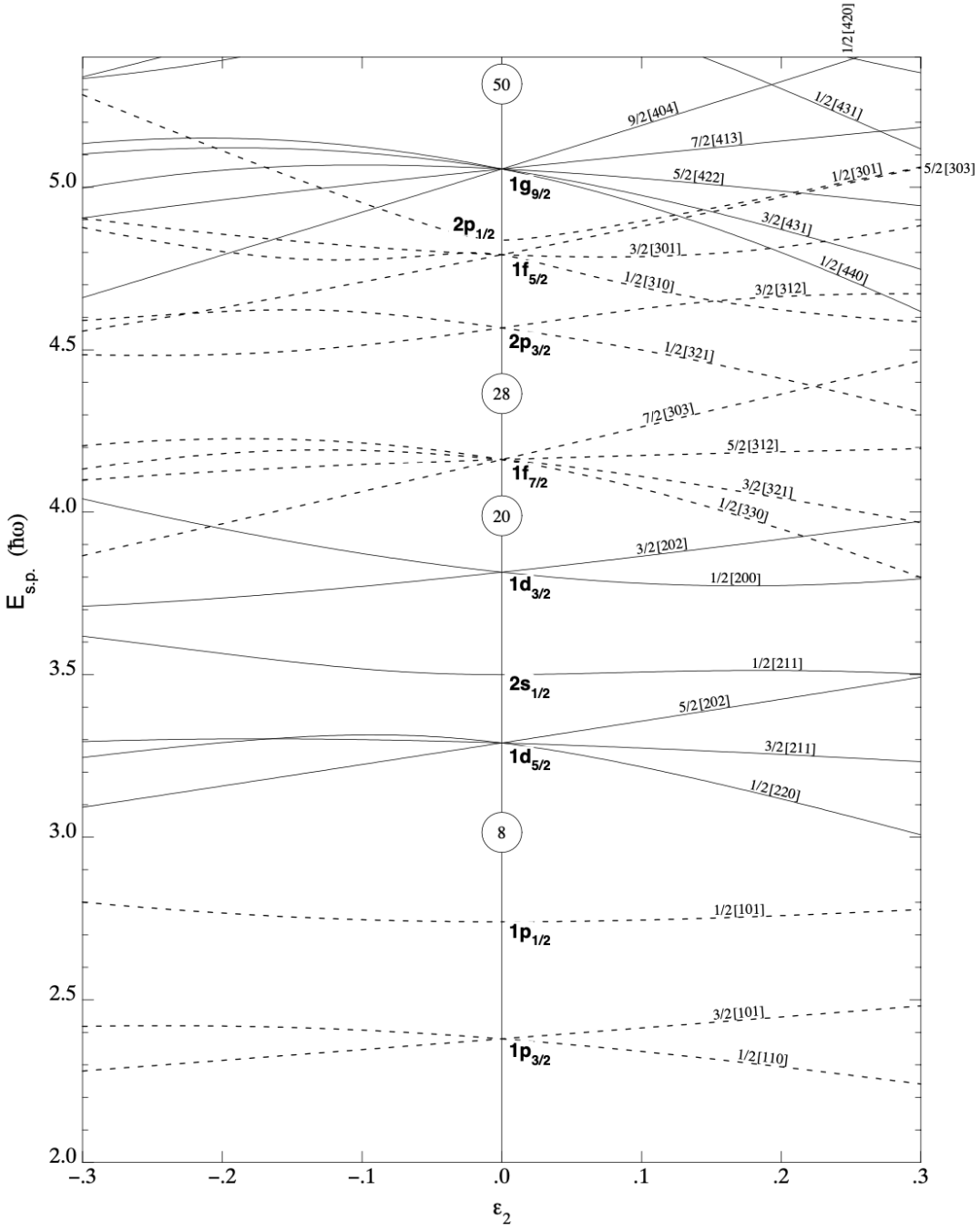

Figure 2.3: A diagram of the energies of nuclear sub-shells as a function of nuclear deformation as predicted by the Nilsson model up to $N = 50$ [26].

Another noteworthy consequence of the Nilsson model is that the distribution of energy levels for a given single-particle state is dependent not only on the magnitude of the deformation, but also on the type of deformation. This can be explained with reference to figure 2.4, which shows the individual j_z projections for $J = 7/2$, and the associated nucleon orbitals for both an oblate and prolate nucleus. In either case, the angle between the z axis and the orbital planes is greatest for the $j_z = 1/2$. Therefore, in the case of a prolate nucleus, the $j_z = 1/2$ orbital has a greater spatial overlap with the nuclear volume, and as a consequence, the nucleons in this orbital are more tightly bound compared to those in the other orbitals. The opposite is true for the oblate nucleus, as the $j_z = 7/2$ orbital will have the greatest spatial overlap with the nuclear volume. The more strongly bound a nucleon is to the nucleus, the lower the energy of the orbital it occupies.

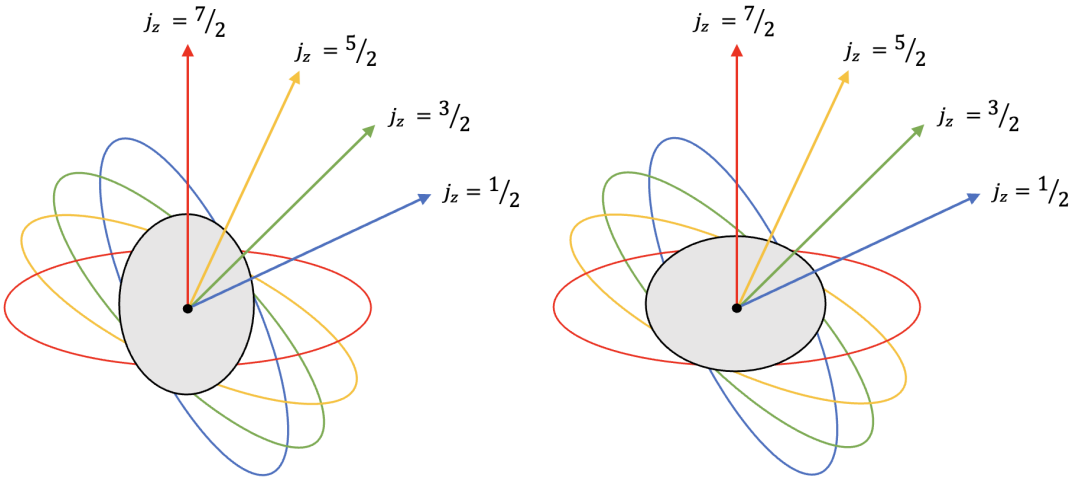

Figure 2.4: A diagram to show the different j_z projections and the associated nucleon orbitals for a prolate (left) and an oblate (right) nuclear core.

As the magnitude of deformation increases, the more complex the orbital structure becomes due to increased band-crossing. With reference to the Nilsson diagram in figure 2.3, it becomes clear that the large energy separations between shells predicted by the single particle model diminish as the nucleus becomes sufficiently deformed; explaining why magicity is less common for deformed nuclei.

2.4 Contemporary Nuclear Models

In addition to the classical models discussed above, modern approaches that rely on the calculation power of computers have been developed. Two of these modern approaches are discussed below: the ab-initio approach and the density functional theory. Nuclear charge radii may be

directly calculated using either approach.

2.4.1 The ab-initio Approach

An alternative approach to modelling a nucleus is to consider the individual constituent nucleons and the strong, weak, and electromagnetic interactions between them. This proves to be very difficult due to the non-perturbative nature of the strong force at low energies (the energies at which nuclei exist), coupled with the fact that protons and neutrons have their own substructure of interacting quarks, anti-quarks and gluons. It is clear that modelling each individual interaction is a complex problem and one that grows exponentially with the addition of nucleons.

Due to the complexity of modelling individual nucleon interactions, effective field theories, such as chiral effective field theory, are employed instead. The field theories act as a starting point for modelling the fundamental forces that govern nucleon interactions. The ab-initio calculations involve solving the relativistic many-body Schrödinger equation starting from only the interactions between nucleons. These models are then used to predict the properties of nuclei and have proven to be very successful when modelling the lightest of nuclei. As ab-initio calculations become more sophisticated, they are also beginning to be able to accurately predict the properties of heavier, more complex systems [27]. Modelling heavier systems is only possible in the vicinity of good shell closures where it may be assumed that there are no particle excitations beyond the shell closure.

A recent example of using ab-initio approaches to model heavier nuclei can be found in the work of Malbrunot-Ettenauer *et al.* [28], where the charge radii of nickel isotopes were modelled using the following methods: the self-consistent Green's function (SCGF) approach, the valence-space in medium similarity renormalization group (VS-IMSRG) method, and the coupled cluster (CC) method. This work showed that remarkable agreement between the absolute charge radii and changes in mean-square charge radii predicted by theory and measured experimentally could be achieved when using the chiral effective field theory based nuclear potential NNLO_{sat} (next-to-next-to leading order) [29] in any of the above-mentioned ab-initio approaches. Furthermore, $NN + 3N(lnl)$ [30] and 1.8/2.0(EM) [31] interactions were used in the SCGF and VS-IMSRG calculations, respectively, and strong agreement was again achieved between the theoretically and experimentally determined changes in mean-square charge radii, however, these methods were unable to reproduce the absolute charge radii.

2.4.2 Density Functional Theories

A second ground-up approach to modelling nuclei is the nuclear Density Functional Theory (DFT). DFT is based upon a theorem proposed in 1964 by Hohenberg and Kohn [32], who were attempting to model the ground state of an electron gas interacting with an external field, $v(r)$. They discovered that it was possible to do so using a universal functional of the electron density, $F[n(r)]$, which was independent of the external field, and reproduced the correct ground state energy for a given external potential when used in the expression:

$$E = \int v(r)n(r)dr + F[n(r)]. \tag{2.4.1}$$

It is apparent that this functional approach is very powerful: for a complex N-body system it is possible to deduce all ground state properties from just three variables, rather than perform calculations accounting for all possible interactions between the N constituents [33]. This functional approach was extended to describe the properties of nuclei by developing nuclear density functionals which account for the differences between nuclear matter and electron gases. For example, in the case of a system of electrons there is an external potential, however, this is not true for a nucleus, which is itself a self-bound entity. The nuclear functional approach must also account for the fact that nuclear interactions will dominate the system, whereas in the system of electrons it is the Coulomb force that dominates. Nuclear interactions are also strongly dependent on spin, and the short-range nature of the strong force means that the constituent nucleons do not often share mutual interactions [34].

There are various energy density functionals such as the Skyrme type, the Gogny type and the Relativistic Mean Field (RMF) model with classical meson fields, but the most relevant in the field at present is the Fayans density functional [35]. This functional was developed as an attempt towards a universal nuclear density functional capable of describing nuclei across the entire chart of nuclides. The relevance of DFT was highlighted in the introduction of this thesis with reference to many recent experimental campaigns; it is particularly noteworthy that in all of the works referenced ([6], [9], [14], [15], [16], and [17]) a variation, or variations of the Fayans density functional were used.

The advantage the Fayans density functional has over other functionals is its ability to accurately predict the charge radii along semi-magic isotope chains of spherical nuclei. For example, and with particular relevance to this work, the Fayans functional has successfully been used to accurately model the charge radii along the calcium isotope chain, which as discussed in the

introduction has many complex features. Alternative functionals are able to reproduce the charge radii along isotope chains reasonably well, but often fail to reproduce localised features or severely underestimate the magnitude of any odd-even staggering [36].

Chapter 3

The Hyperfine Structure and Isotope Shift

Laser spectroscopy is based fundamentally on two principles: electron excitation by resonant photon absorption and detection of the subsequent de-excitation via photon emission. Resonant excitation occurs when the energy of a photon is equal to that which separates two electron energy states:

$$E_{photon} = \Delta E = E_2 - E_1. \tag{3.0.1}$$

Upon excitation, an electron will only occupy an excited state for a brief period of time (typically in the order of nanoseconds) before it de-excites into a lower energy state via photon emission. This principle is illustrated in figure 3.1. One may investigate the electronic structure of an atomic system by using an external source of radiation such as a laser. The frequency of the laser is varied and the photons emitted following resonant absorption are detected and counted to generate a spectrum. The peaks of the spectrum correspond to the electron transition energies, and therefore the electronic structure of an atom is determined.

At high resolution, the distribution of electron states is influenced by the properties of the nucleus to which they are bound - this is known as the hyperfine structure. Studies of the hyperfine structure allow for direct determination of these nuclear properties. The fine structure transition energies are known and tabulated for all elements up to and including nobelium [37], meaning that the transitions can be conveniently located for study at higher resolution in order to probe their associated hyperfine transitions.

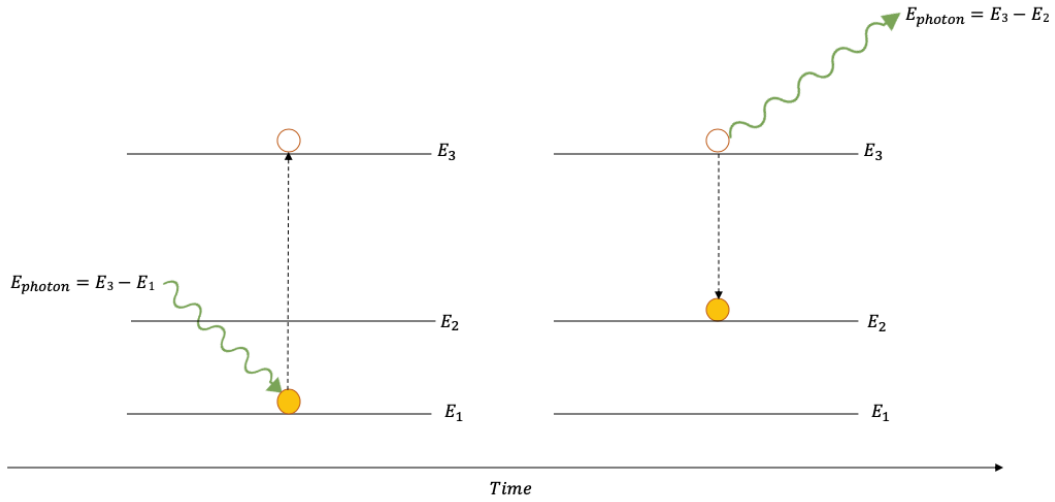

Figure 3.1: A diagram to show the promotion of an electron to a higher energy level via photon absorption, followed by electron de-excitation to a different energy level via photon emission.

3.1 Physical Origins of the Hyperfine Structure

The fine structure of an atomic system allows for effects such as the spin-orbit coupling of an electron to be observed, manifesting itself as the splitting of electron energy levels into sub-states. The fine structure defines the total electronic angular momentum, **J**, as the sum of the orbital and intrinsic angular momentum of the electrons, denoted as **L** and **S**, respectively: $\mathbf{J} = \mathbf{L} + \mathbf{S}$. At the precision of the fine structure, the electron transition energies are independent of the isotope being probed, well known, and tabulated in databases.

The hyperfine structure is the level of substructure that follows the fine structure resulting from the isotope dependent properties of the constituent nucleus. It may be observed by studying the fine structure at higher precision. The quantum mechanical formulae used to describe the hyperfine structure are analogous to those used for the fine structure. For example, in the hyperfine structure, a new total angular momentum, **F**, is defined by the coupling of **J** and **I**, where **I** is the spin of the nucleus: $\mathbf{F} = \mathbf{J} + \mathbf{I}$. Figure 3.2 illustrates the coupling of the nuclear spin and total electronic angular momentum.

The vector coupling of **I** and **J** to form **F** is illustrated below and is once again analogous to the coupling of **L** and **S** to form **J**. For example, by taking the square of **F** ($\mathbf{F}^2 = \mathbf{J}^2 + 2\mathbf{J}\cdot\mathbf{I} + \mathbf{I}^2$) it is possible to isolate $\mathbf{I}\cdot\mathbf{J}$:

$$\mathbf{I}\cdot\mathbf{J} = \frac{1}{2}[\mathbf{F}^2 - \mathbf{J}^2 - \mathbf{I}^2], \tag{3.1.1}$$

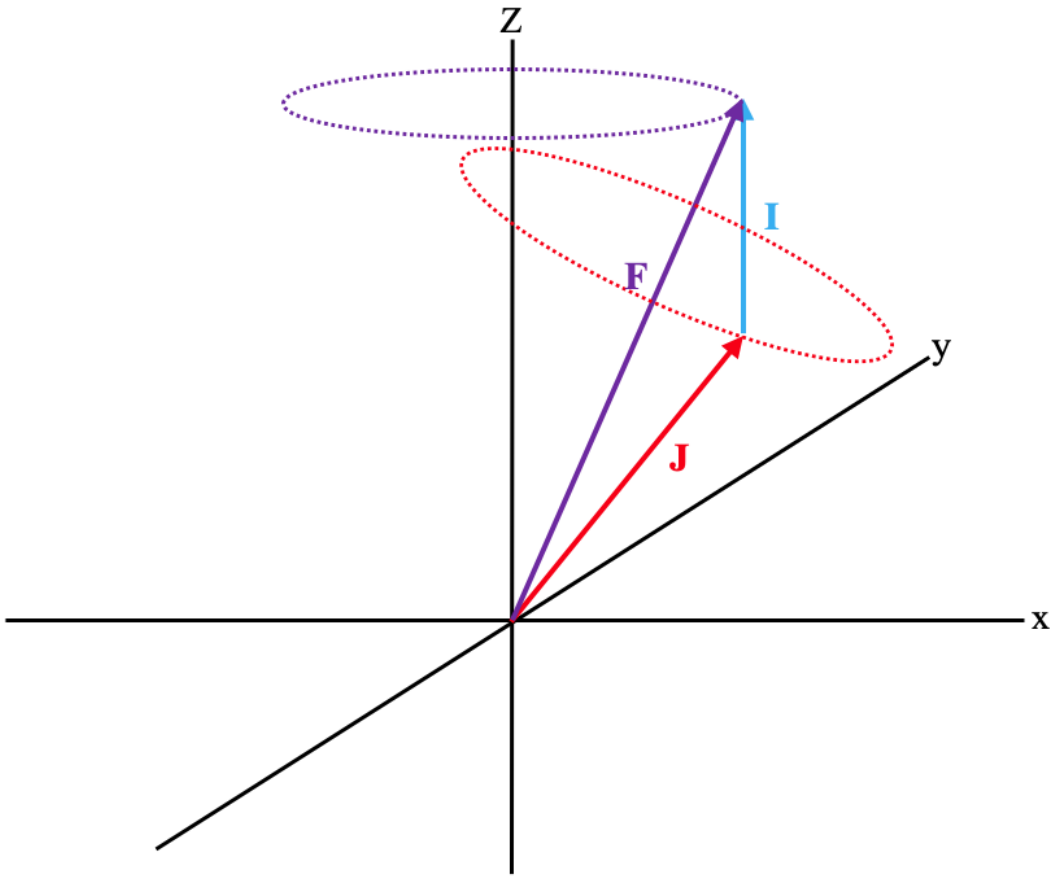

Figure 3.2: An illustration of the vector coupling of the total electronic angular momentum vector **J** and the nuclear spin vector **I**, where **I** and **J** precess around **F**.

$$\therefore \langle I \cdot J \rangle = \frac{\hbar^2}{2}[F(F+1) - I(I+1) - J(J+1)] = \frac{\hbar^2}{2}K, \tag{3.1.2}$$

where,

$$K = F(F+1) - J(J+1) - I(I+1). \tag{3.1.3}$$

The number of F states is given by:

$$F = J + I, (J+I) - 1, ..., |J - I|. \tag{3.1.4}$$

The allowable transitions between the F states of the upper and lower J states are dictated by the hyperfine selection rules [20]:

$$\Delta F = 0, \pm 1, \tag{3.1.5}$$

but where,

$$F = 0 \rightarrow F = 0, \tag{3.1.6}$$

is a forbidden transition. These selection rules arise from the principle of conservation of angular momentum and the fact that electrons transition between hyperfine states via absorption and emission of electric dipole photons, which carry one unit of angular momentum.

Two fine structure transitions were used when probing the hyperfine structure in this work. Both transitions originate from the atomic ground state, $J = 3$, and for both the excitation is to an upper state with $J = 4$. These transitions were selected for use in this study owing to their high spectroscopic efficiencies. These transitions will henceforth be referred to the 358 nm and 425 nm lines. The properties of each transition are presented in table 3.1.

Transition (nm)	Lower State	Lower State Energy (cm^{-1})	Upper State	Upper State Energy (cm^{-1})	A coefficient ($10^7 s^{-1}$)
357.87	$3d^5(^6S)4s\ ^7S_3$	0	$3d^4(^5D)4s4p(^3P)\ ^7P_4$	27935.2412	14.83
425.43	$3d^5(^6S)4s\ ^7S_3$	0	$3d^5(^6S)4p\ ^7P_4$	23498.8156	3.148

Table 3.1: A table to present the properties of the two atomic transitions used to probe the hyperfine structure in this work. Information taken from Kurucz spectral line database [38] and National Institute of Standards and Technology spectral line database [39].

Figure 3.3 serves to illustrate the hyperfine splitting of the aforementioned J states into their respective F states and the allowable transitions between F states when probing ^{53}Cr ($I = 3/2$) via the 425 nm transition.

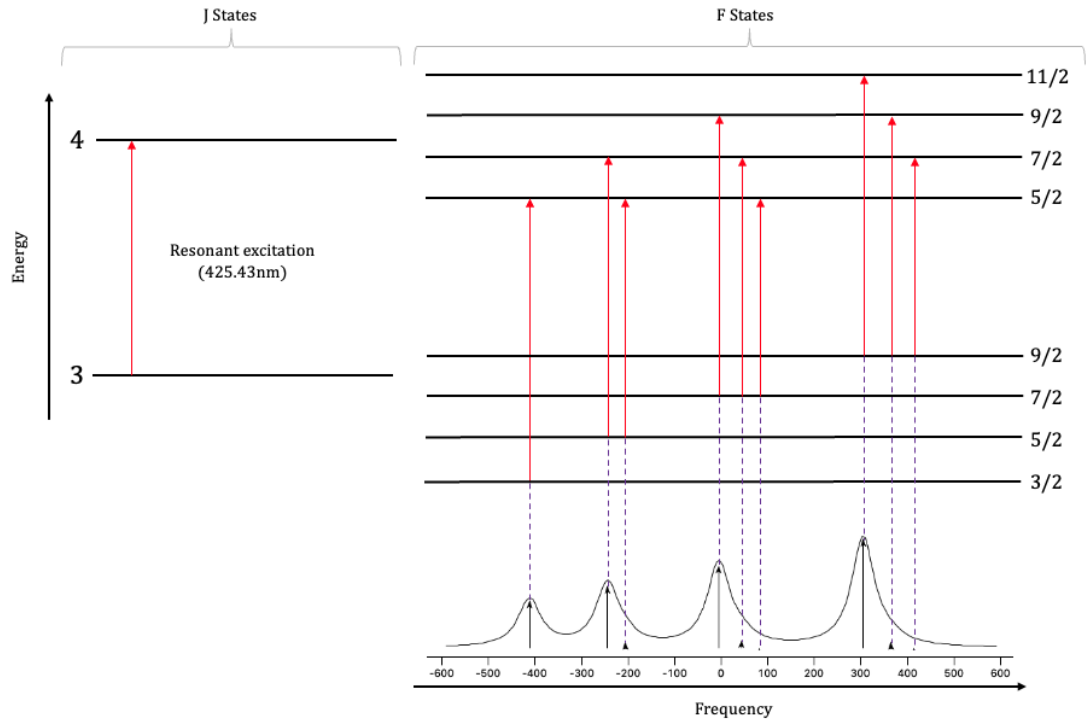

Figure 3.3: A diagram to show the hyperfine Splitting in ^{53}Cr ($I = 3/2$) of the $J = 3, 4$ states into their respective F states. The red lines show the allowable transitions between the F states and the purple dashed lines lead to the corresponding peaks in the modelled hyperfine spectrum.

There are two contributing properties of the nucleus which dictate the relative distribution of the F states and thus the hyperfine structure: the magnetic dipole moment and the electric quadrupole moment.

3.1.1 The Magnetic Dipole Moment

The magnetic dipole moment of the nucleus originates from the motion of the charged particles that form the nuclear substructure. The movement of the charged particles is akin to a current moving through a wire, therefore a vector potential, $\boldsymbol{A}(\boldsymbol{r})$, can be formed by summing the individual currents:

$$\boldsymbol{A}(\boldsymbol{r}) = \frac{\mu_0}{4\pi} \int \frac{\boldsymbol{j}(\boldsymbol{r}')dv'}{|\boldsymbol{r} - \boldsymbol{r}'|}, \tag{3.1.7}$$

where $\boldsymbol{j}(\boldsymbol{r}')$ is the current density, $\boldsymbol{r}'$ is a vector defining a point of the nucleus relative to a fixed origin, and $\boldsymbol{r}$ is the vector defining the point of observation relative to the origin. This vector potential may be rewritten as:

$$\boldsymbol{A}(\boldsymbol{r}) = \frac{\mu_0}{4\pi}\left[\frac{1}{r}\int \boldsymbol{j}(\boldsymbol{r}')dv' + \frac{1}{r^3}\int (\boldsymbol{j}(\boldsymbol{r}')(\boldsymbol{r}\cdot\boldsymbol{r}')dv' + ...+\right], \tag{3.1.8}$$

$$\therefore \boldsymbol{A}(\boldsymbol{r}) = \frac{\mu_0}{4\pi}\frac{\boldsymbol{\mu}\times\boldsymbol{r}}{r^3} + ...+, \tag{3.1.9}$$

when

$$\boldsymbol{\mu} = \frac{1}{2}\int \boldsymbol{r}'\times\boldsymbol{j}(\boldsymbol{r}')dv'. \tag{3.1.10}$$

The primary term in this multi-polar expansion corresponds to the magnetic dipole moment of the nucleus. Accounting for the fact that the cross product of r' and v' is simply equal to l/m for a particle of mass m, where l is the dimensionless orbital angular momentum quantum number, and that the charge density may be expressed in terms of a probability function, the expression above may be rewritten as:

$$\boldsymbol{\mu} = \frac{e}{2m}\int \psi^*(\boldsymbol{r}')l\psi(\boldsymbol{r}')dv'. \tag{3.1.11}$$

Assuming that this wave-function represents a definite component of l_z, the only none vanishing term is the one which corresponds to the z component of the integral, therefore:

$$\mu_z = \frac{e}{2m}\int \psi^*(r')l_z\psi(r')dv', \tag{3.1.12}$$

and

$$\therefore \mu_z = \frac{e\hbar}{2m}m_l, \tag{3.1.13}$$

where $l_z = m_l\hbar$. The magnetic dipole moment is defined to correspond to the maximum value of m_l. Accordingly, the magnetic moment of an individual nucleon and is given by:

$$\mu = \frac{e\hbar}{2m}l, \tag{3.1.14}$$

as the maximum value m_l can adopt is $+l$. The $e\hbar/2m$ coefficient accounts the dimensions of the magnetic moment. When m adopts the value of the proton mass, this quantity is known as the nuclear magneton:

$$\mu_N = \frac{e\hbar}{2m_p} = 3.15245\cdot 10^{-8} \quad \text{eV/T}. \tag{3.1.15}$$

A more conventional way to express the magnetic moment of a nucleon in terms of the nuclear

magneton is:

$$\mu = \frac{g_l l}{\mu_N}, \tag{3.1.16}$$

where g_l is the orbital gyromagnetic factor or 'g-factor' of a free nucleon. The value of g_l is 0 and 1 for a proton and neutron, respectively. The l term only accounts for the orbital contribution to the magnetic moment, in order to account for the contribution from the intrinsic spin of nucleons, equation 3.1.16 is modified to become:

$$\boldsymbol{\mu} = \boldsymbol{\mu_l} + \boldsymbol{\mu_s} = (g_l \boldsymbol{l} + g_s \boldsymbol{s}) \frac{\mu_N}{\hbar}, \tag{3.1.17}$$

where g_s is the gyromagnetic spin factor, which can only be determined for free particles and is measured to be equal to 5.5856912 for a proton and -3.8260837 for a neutron. When considering the contribution from each of the constituent nucleons, the magnetic moment of the nucleus may be calculated as the sum of the magnetic moments of its individual constituent nucleons:

$$\boldsymbol{\mu_I} = \sum_{i=1}^{A} \left[g_{l,i} \boldsymbol{l_i} + g_{s,i} \boldsymbol{s_i} \right] \frac{\mu_N}{\hbar}. \tag{3.1.18}$$

Unfortunately, the magnetic moment of a nucleus cannot be calculated this trivially as a result of the complex nature of the strong nuclear interactions and relative spin orientations of the constituent nucleons, rather model-based assumptions must be used. For example, using the single particle model, we assume that in odd-A nuclei $A-1$ nucleons pair together to form spin-zero duads, which do not contribute to the magnetic moment, and that the orbital and spin angular momentum of the remaining nucleon dictates the magnetic moment of the nucleus.

In more complex cases in which the bulk nucleons do not pair into spin zero-duads, it is necessary to assign to them a collective g-factor, g_R, so that their contribution to the nuclear magnetic moment is not neglected. In these cases the magnetic moment may be calculated using:

$$\boldsymbol{\mu_I} = \left[g_R \boldsymbol{I_c} + \sum_{i=1}^{A} \left(g_{l,i} \boldsymbol{l_i} + g_{s,i} \boldsymbol{s_i} \right) \right] \frac{\mu_N}{\hbar}. \tag{3.1.19}$$

The motion of electrons in their atomic orbits can be considered to be an electrical current, which consequently produces a magnetic field. This magnetic field interacts with the magnetic dipole moment of the nucleus causing the fine structure energy states to split into multiple distinct hyperfine energy states. The magnitude of the hyperfine structure splitting is given by:

$$\Delta E_M = -\boldsymbol{\mu_I} \cdot \boldsymbol{B_e}, \tag{3.1.20}$$

where $\boldsymbol{B_e}$ is the magnetic field produced by the orbital electrons.

The magnitude of the magnetic field generated by an electron is proportional to its total angular momentum. As such, equation 3.1.20 may also be expressed as:

$$\Delta E_M = \frac{A}{2}[F(F+1) - I(I+1) - J(J+1)] = \frac{AK}{2}, \tag{3.1.21}$$

where A is the magnetic dipole hyperfine parameter.

From equation 3.1.21, it can be understood that there is no energy level splitting due to the magnetic dipole contribution when $I = 0$ (as is the case for the ground states of all even-even nuclei), or when $J = 0$ [20].

3.1.2 The Electric Quadrupole Moment

The electric quadrupole moment provides an insight into the deformation of a nucleus from a spherical shape. Spherical nuclei are the exception (such as those found at magic numbers), and therefore the quadrupole moment is an incredibly powerful indicator that can be used to gauge the trends in deformation along isotope chains. The charge distribution of the nucleus generates an electric potential, which from an external vantage point takes the form of [20]:

$$V(\boldsymbol{r}) = \frac{1}{4\pi\epsilon_0}\int \frac{\rho(\boldsymbol{r'})dv'}{|\boldsymbol{r} - \boldsymbol{r'}|}, \tag{3.1.22}$$

where $\rho(\boldsymbol{r'})$ is the nuclear charge density, $\boldsymbol{r}$ is the vector between an origin and an external vantage point, and $\boldsymbol{r'}$ is the vector defining the distance between the origin and the distribution of nuclear charges. The denominator of the integrand can be expressed as a multi-polar expansion of the electric field:

$$\begin{aligned} |\boldsymbol{r} - \boldsymbol{r'}|^{-1} &= r^{-1}\left[1 + \frac{r'^2}{r^2} - 2\frac{r'}{r}\cos\theta\right]^{-1/2} \\ &\approx \frac{1}{r}\left[1 - \frac{1}{2}\left(\frac{r'^2}{r^2} - 2\frac{r'}{r}\cos\theta\right) + \frac{3}{8}\left(r'^2r^2 - 2\frac{r'}{r}\cos\theta\right)^2 + ...\right], \end{aligned} \tag{3.1.23}$$

where θ is the angle between r and r'. Substituting the expansion into the original potential gives:

$$V(\boldsymbol{r}) = \frac{1}{4\pi\epsilon_0}\left[\frac{1}{r}\int \rho(\boldsymbol{r}')dv' + \frac{1}{r^2}\int \rho(\boldsymbol{r}')\cos\theta dv' + \frac{1}{r^3}\int \rho(\boldsymbol{r}')r'^2 \cdot \frac{1}{2}(3\cos^2\theta - 1)dv' + ...\right]. \tag{3.1.24}$$

The integral of the first term in the expansion provides the total charge of the nucleus, the second term of the expansion becomes zero in regular circumstances as the nucleus does not exhibit an electric dipole moment, and the third term in the expansion is related to the electric quadrupole moment, Q, which we define as:

$$eQ = \int \rho(\boldsymbol{r}')r^2(3\cos^2\theta - 1)dv' = \int \rho(\boldsymbol{r}')(3z'^2 - r'^2)dv'. \tag{3.1.25}$$

A quadrupole moment equal to zero is characteristic of a spherical nuclear configuration. If the quadrupole moment is positive, the $3z^2$ term dominates as the charge density is concentrated along the z axis, and the nucleus has a prolate (cigar) shape. A negative electric quadrupole occurs when the r^2 term dominates, meaning that the charge distribution extends along the equatorial plane perpendicular to the z axis and that the nucleus is oblate (discus) in shape [40]. The magnitude of the quadrupole moment indicates to what extent the nucleus is deformed.

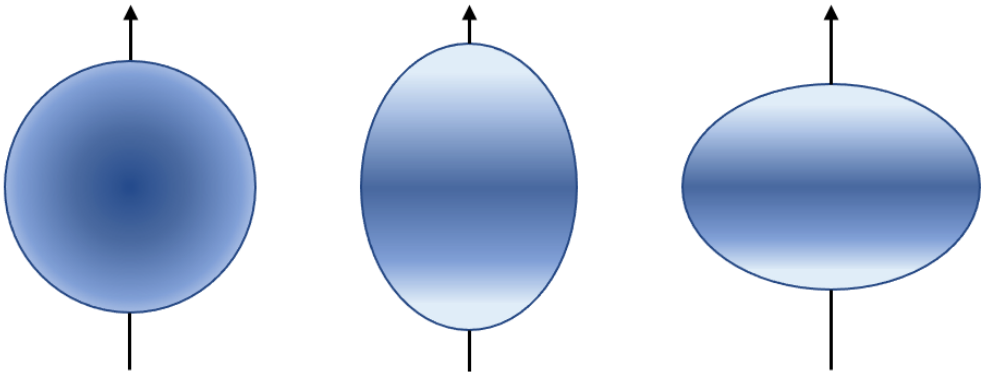

Figure 3.4: A pictorial representation of a spherical nucleus (left), a prolate nucleus (centre), and an oblate nucleus (right), each with a retained axis of symmetry.

The contribution of the electric quadrupole moment to the hyperfine structure originates from the quadrupole moment of the nucleus interacting with the gradient of the electric field produced by the orbital electrons, $\frac{\partial^2 V}{\partial z^2}$. The magnitude of the hyperfine structure splitting due to the spectroscopic quadrupole moment, Q_s is given by [20]:

$$\Delta E_Q = eQ_s \cdot \left\langle \frac{\partial^2 V}{\partial z^2} \right\rangle \cdot \frac{3K(K+1) - I(I+1)J(J+1)}{8I(2I-1)J(2J-1)}. \tag{3.1.26}$$

From equation 3.1.26, it can be understood that there is no energy level splitting due to the

electric quadrupole contribution when I or $J \leq 1/2$.

The spectroscopic electric quadrupole moment is related to the intrinsic quadrupole moment via the relationship [1]:

$$Q_s = Q\left(\frac{3\Omega^2 - I(I+1)}{(I+1)(2I+3)}\right), \tag{3.1.27}$$

where Ω is the projection of nuclear spin along the intrinsic axis of symmetry. The intrinsic quadrupole moment may be expressed in terms of the static deformation parameter, $\langle\beta_2\rangle$, using the approximation:

$$Q \approx \frac{5Z\left\langle r^2\right\rangle_0}{\sqrt{5\pi}}\langle\beta_2\rangle\left(1 + 0.36\langle\beta_2\rangle\right), \tag{3.1.28}$$

where $\left\langle r^2\right\rangle_0$ is the mean-square charge radius of a spherical nucleus, which when modelled using the liquid drop model assuming a homogeneous distribution of nuclear material is given by [41]:

$$\left\langle r^2\right\rangle_0 = \frac{3}{5}r_0^2 A^{2/3}. \tag{3.1.29}$$

3.1.3 Combined Hyperfine Contributions

The combined contribution to the fine structure splitting by the magnetic dipole moment and electric quadrupole moment is given by:

$$E_{hfs} = \frac{A}{2}K + \frac{B}{4}\cdot\frac{3K(K+1) - 4I(I+1)J(J+1)}{2I(2I-1)J(2J-1)}. \tag{3.1.30}$$

A is the magnetic dipole moment hyperfine parameter and B is the electric quadrupole moment hyperfine parameter. A and B are related to their corresponding nuclear moments by the following equations [42]:

$$A = \frac{\mu_I B_e}{IJ}, \tag{3.1.31}$$

$$B = eQ_s\left\langle\frac{\partial^2 V}{\partial z^2}\right\rangle. \tag{3.1.32}$$

Equations 3.1.31 and 3.1.32 illustrate that, for a given fine structure level, $A \propto \frac{\mu}{I}$ and $B \propto Q_s$. Accordingly, these relationships can be used to determine unknown magnetic dipole and electric quadrupole moments using appropriate reference hyperfine parameters and moments:

$$\mu = \mu_{ref}\frac{IA}{I_{ref}A_{ref}}, \tag{3.1.33}$$

$$Q_s = Q_{s,ref}\frac{B}{B_{ref}}. \tag{3.1.34}$$

Furthermore, equations 3.1.35 and 3.1.36 show that the ratio of the A or B hyperfine parameter of an upper J state to that of a lower J state is isotope independent and remains constant for a given fine structure transition:

$$\frac{A_l}{A_u} = \frac{\left(\frac{\mu B_e}{IJ}\right)_l}{\left(\frac{\mu B_e}{IJ}\right)_u} = \frac{(B_e/J)_l}{(B_e/J)_u} = \text{constant}, \tag{3.1.35}$$

and

$$\frac{B_l}{B_u} = \frac{\left(eQ_s\left\langle\frac{\partial^2 V}{\partial z^2}\right\rangle\right)_l}{\left(eQ_s\left\langle\frac{\partial^2 V}{\partial z^2}\right\rangle\right)_u} = \text{constant}. \tag{3.1.36}$$

3.1.4 Defining Hyperfine Transitions

A resonance peak in a hyperfine spectrum may be defined according to the difference in energy between the two F states the transition occurs between [1]:

$$\gamma = v + \alpha_u A_u + \beta_u B_u - \alpha_l A_l - \beta_l B_l, \tag{3.1.37}$$

where the quantum numbers and hyperfine parameters of the upper and lower states are indicated by their respective subscripts, v is the centroid frequency of the central point around which the hyperfine splitting is based,

$$\alpha = \frac{K}{2}, \tag{3.1.38}$$

and

$$\beta = \frac{3K(K+1) - 4I(I+1)J(J+1)}{8I(2I-1)(2J-1)}. \tag{3.1.39}$$

3.2 The Nuclear Mean-Square Charge Radius

The mean-square charge radius of a nucleus, $\langle r^2\rangle$, is an observable that provides information about the spatial extension of the nucleus (more specifically the constituent protons), and the deformation and rigidity of the nucleus. A general expression for the mean-square charge radius for a nucleus with a charge density function, $\rho(\mathbf{r})$, is [41]:

$$\left\langle r^2 \right\rangle = \frac{\int \rho(\mathbf{r}) r^2 dV}{\int \rho(\mathbf{r}) dV}, \tag{3.2.1}$$

where the total charge of the nucleus is given by the denominator. If one were to describe the mean-square charge radius of a deformed nucleus, the expression above is modified to account for the deviation from sphericity:

$$\left\langle r^2 \right\rangle = \left\langle r^2 \right\rangle_0 \left(1 + \frac{5}{4\pi} \sum_{i=2}^{\infty} \left\langle \beta_i^2 \right\rangle \right), \tag{3.2.2}$$

where $\left\langle \beta_i^2 \right\rangle$ is the deformation parameter of the order i. Due to the dominance of the contribution from the quadrupole deformation, the expression above is often approximated as:

$$\left\langle r^2 \right\rangle \approx \left\langle r^2 \right\rangle_0 \left(1 + \frac{5}{4\pi} \left\langle \beta_2^2 \right\rangle \right), \tag{3.2.3}$$

where $\left\langle r^2 \right\rangle_0$ is the mean-square charge radius of a spherical nucleus.

The dynamic nature of the deformation of a nucleus may be interpreted via a comparison between the square of the static deformation parameter, $\langle \beta_2 \rangle^2$, and the quadrupole deformation parameter, $\left\langle \beta_2^2 \right\rangle$, using the relationship [1]:

$$\left\langle \beta_2^2 \right\rangle = \langle \beta_2 \rangle^2 + \left(\left\langle \beta_2^2 \right\rangle - \langle \beta_2 \rangle^2 \right) = \beta_{static}^2 + \beta_{dynamic}^2. \tag{3.2.4}$$

Once one has determined the static component of the electric quadrupole deformation, the rigidity of the deformation may be determined by using the square of β_{static}^2 in place of $\left\langle \beta_2^2 \right\rangle$ in equation 3.2.3. If the value of the mean-square charge radius calculated differs from that determined experimentally, and other contributions towards deformation are not present, this is emblematic of β-softness [1].

3.3 Isotope Shifts

The spectrum of one isotope is always shifted in frequency relative to that of a neighbouring isotope. This phenomenon is known as the isotope shift, δv. Whilst all isotopes with non-zero spin exhibit hyperfine resonances due to their nuclear moments, the isotope shift is a phenomenon observed in all isotopes regardless of spin, meaning that laser spectroscopy still yields useful information even without the presence of a hyperfine structure to probe. There are two independent contributions to the isotope shift: the mass shift contribution and the field shift contribution. These will be discussed in more detail in the following subsections.

Historically, there has been a lack of consistency in the literature as to what is the best convention for stating the isotope shift between two isotopes as well as the notation for doing so. For example, some define the isotope shift as:

$$\delta\nu = \nu^{A} - \nu^{A'}, \tag{3.3.1}$$

where $\nu^{A'}$ is the centroid frequency of the heavier of the two isotopes, and ν^{A} is the centroid frequency of the lighter, reference isotope. Others define the isotope shift as:

$$\delta\nu = \nu^{A} - \nu^{A'} > 0, \tag{3.3.2}$$

meaning that the isotope shift is always positive. Both of these conventions can become inconvenient as the reference isotope may differ for each isotope of interest, and therefore additional calculations are required in order to compare the isotope shifts relative to a single isotope. A more convenient way of defining the isotope shift, and the approach adopted in modern laser spectroscopy, is:

$$\delta\nu^{A,A'} = \nu^{A'} - \nu^{A}, \tag{3.3.3}$$

where $\nu^{A'}$ is the centroid frequency of the isotope of interest and ν^{A} is the centroid frequency of the reference isotope. This definition does not require the isotope shift to be positive, and the same reference may be used for all isotopes along an isotope chain, regardless of whether they are heavier or lighter than the isotope of interest.

As mentioned previously, different notation conventions are also adopted by different authors. For example, Cheal and Flanagan define the isotope shift using equation 3.3.3 [1], whereas Berengut *et al.* define the isotope shift as [43]:

$$\delta\nu^{A',A} = \nu^{A'} - \nu^{A}, \tag{3.3.4}$$

where $\nu^{A'}$ is the centroid frequency of the isotope of interest and ν^{A} is the centroid frequency of the reference isotope. In these examples, the order of the superscript is reversed on the $\delta\nu$ term.

The convention and notation adopted for this work and used throughout this thesis is:

$$\delta\nu^{A,A'} = \nu^{A} - \nu^{A'}, \tag{3.3.5}$$

where v^A is the centroid frequency of the isotope of interest and $v^{A'}$ is the centroid frequency of the reference isotope. Note that using this notation convention, the prime notation is used oppositely to the examples outlined above.

3.3.1 The Mass Shift Contribution

In an atomic system, in response to the motion of orbital electrons, the nucleus is forced to recoil with a momentum equal and opposite to the momenta of the electrons. The recoil energy of the nucleus is therefore calculable using the following expression [44]:

$$E_{MS} = \frac{1}{2M}\left(\sum_i \mathbf{p}_i\right)^2 = \frac{1}{2M}\sum_i \mathbf{p}_i^2 + \frac{1}{2M}\sum_{i>j}(2\mathbf{p}_i \cdot \mathbf{p}_j), \tag{3.3.6}$$

where p_i is the momentum of a given electron, and M is the mass of the nucleus. Accordingly, there is a discrepancy between the recoil energies of nuclei with different masses. This discrepancy is given by:

$$\delta E_{MS} = \frac{1}{2m_u}\left(\frac{A - A'}{AA'}\right)\left(\sum_i \mathbf{p}_i^2 + \sum_{i>j}(2\mathbf{p}_i \cdot \mathbf{p}_j),\right). \tag{3.3.7}$$

The mass shift contribution to the isotope shift may therefore be expressed by the following equation:

$$\delta v_{MS}^{A,A'} = M\frac{A - A'}{AA'}, \tag{3.3.8}$$

where,

$$M = k_{NMS} + k_{SMS}. \tag{3.3.9}$$

M is the mass shift factor, k_{NMS} and k_{SMS} are the normal and specific mass shift factors, respectively, and A and A' represent the atomic masses of an isotope and a reference isotope, respectively. The prime notation here mirrors that of the notation used for the isotope shift. The masses of the isotopes have generally been measured to very high precision using Penning traps [45].

While the specific mass shift factor is complex to calculate, the normal mass shift factor can be calculated relatively easily using the following equation:

$$k_{NMS} = \frac{m_e}{m_u}v, \tag{3.3.10}$$

where m_e is the electron mass, m_u is the atomic mass unit, and v is the transition frequency [43].

In essence, the normal mass shift accounts for the fact that the centre of mass of an atom does not lie at the centre of the nucleus due to the presence of the orbital electrons, whereas the specific mass shift accounts for the collective momenta of multiple atomic electrons. When atomic electrons are evenly distributed around the nucleus, the centre of mass between the nucleus and the electrons lies more centrally with respect to the atom as a whole, whereas when the distribution of electrons is asymmetric, the centre of mass lies less centrally. This shift in the centre of mass either acts to enhance or reduce the contribution of the normal mass shift to the total isotope shift. A schematic example of the specific mass shift is illustrated in figure 3.5. Simply put, a change in the centre of mass will modify the kinematics of the atomic system, leading to the energies of electron states shifting, and resulting in a shift of the central frequency of the spectrum.

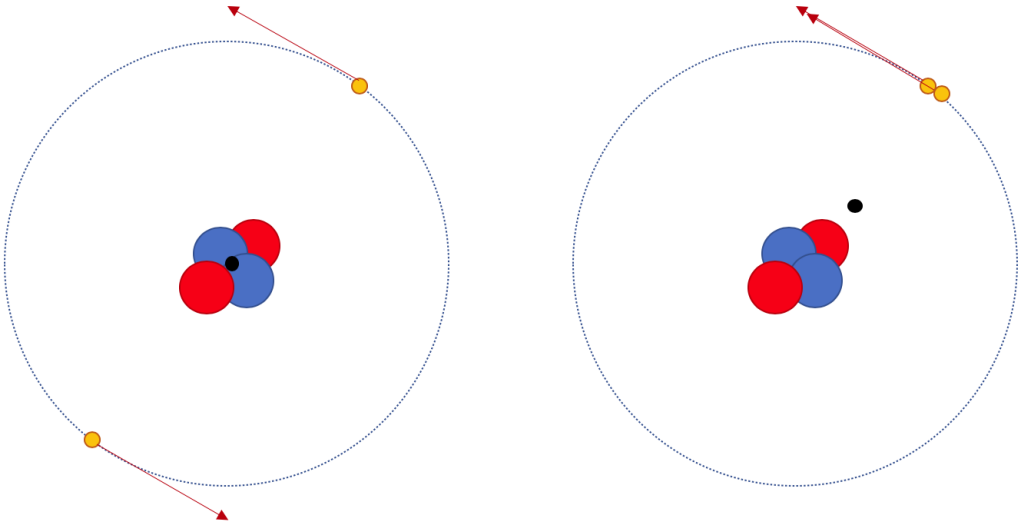

Figure 3.5: A diagram showing how the centre of mass of an atom (black point) may be shifted from the centre of the nucleus depending on the electron configuration of the atom.

3.3.2 The Field Shift Contribution

The second contribution to the isotope shift is the field shift contribution. The field shift contribution can be understood in terms of the electrostatic potential produced by a nucleus, which itself is dictated by the configuration of nucleons within the nucleus. Each isotope or isomer has a unique nuclear charge distribution, which produces a unique electrostatic potential for

electrons to interact with. The magnitude of the perturbations to the electron structure differs for each electrostatic potential, and thus so to does the energy at which hyperfine resonances become detectable.

The electrostatic potential outside of the nucleus can be considered to be the same as that of a point-like nucleus and is therefore the same for each isotope. It is inside the nucleus where the difference in electrostatics between different isotopes plays a role in the field shift contribution; only the electrons which spend time within the vicinity of the nuclear volume, those which occupy the s orbitals, are perturbed directly by the nucleus, however, the rest of the energy levels in the atomic system are indirectly perturbed by electron screening effects.

The change in the energy of an atomic electron due to the field shift is estimated to be the following using non-relativistic first-order perturbation theory [44]:

$$\delta E_i = \int \psi_i^*(r) e \delta V_c \psi_i(r) d\tau, \tag{3.3.11}$$

where $\psi_i(r)$ is the wave-function of an atomic electron, and δV_c is the difference in the Coulomb potential experienced by an electron within the vicinity of the nuclear charge distribution for two isotopes. The contribution of the field shift to the isotope shift can be expressed as:

$$\delta v_{FS} = \frac{Ze^2}{6h\epsilon_0} \Delta|\psi(0)|^2 \delta\langle r^2 \rangle, \tag{3.3.12}$$

where $\Delta|\psi(0)|^2$ represents the change in electron density between the two atomic states being probed, and $\delta \left\langle r^2 \right\rangle^{A,A'}$ is the difference between the nuclear mean-square charge radii of each isotope. Equation 3.3.12 is often expressed as:

$$\delta v_{FS}^{A,A'} = F \delta \left\langle r^2 \right\rangle^{A,A'}. \tag{3.3.13}$$

The change in mean-square charge radius provides information not only about the nuclear size, but also the shape [42]. This is particularly useful as information about the size and shape of nuclei which do not exhibit a spectroscopic quadrupole moment (i.e nuclei with spins $I = 0, 1/2$) can still be garnered.

3.3.3 Combined Isotope Shift

The total shift between two isotopes of the same element is the sum of the mass shift contribution and the field shift contribution:

$$\delta v^{A,A'} = M\frac{A-A'}{AA'} + F\delta\left\langle r^2\right\rangle^{A,A'}, \tag{3.3.14}$$

where A represents the isotope of interest, and A' represents the reference isotope, therefore the change in mean-square charge radius is calculated relative to the isotope of interest, hence why the prime notation mirrors that adopted when defining the isotope shift in equation 3.3.5.

It can be understood that for a given transition between J states, the mass shift factor and field shift factor are isotope independent and thus remain constant along an isotope chain as they are determined purely based on the electronic properties of the atom. Therefore, the mean-square charge radii along an isotope chain are calculable from the measured isotope shifts once the mass and field shift factors have been calibrated.

3.4 The King Plot

Mass and field shift factors are difficult to determine by calculation alone, however, as they are constant for a given transition between two J states and independent of the isotopes being investigated, a convenient way of determining mass and field shift factors is by using a King plot [46]. The mass and field shift factors may be calibrated using one of two different types of King plot: those that use optical data and those that use non-optical data. The King plot that uses non-optical data uses known changes in mean-square charge radii and modified isotope shifts for a given transition to directly extract the mass and field shift factors. The King plot that uses optical data allows for indirect determination of the mass and field shift factors by plotting the modified isotope shifts of two transitions against one another, where the mass and field shift factors of one transition are already known.

Regardless of which type of King plots is used, a modification factor, μ, must be applied to the isotope shifts and/or changes in mean-square charge radii; μ is defined as:

$$\mu = \frac{AA'}{A-A'}, \tag{3.4.1}$$

where A and A' are the atomic masses of the isotope of interest and the reference isotope respectively.

For the King plot that uses non-optical data, each term of equation 3.3.14 is multiplied by μ. The equation is then conveniently already in a $y = mx + c$ format:

$$\frac{AA'}{A-A'}\delta v^{A,A'} = F\frac{AA'}{A-A'}\delta\left\langle r^2\right\rangle^{A,A'} + M. \tag{3.4.2}$$

From equation 3.4.2 it becomes apparent that plotting the modified changes in mean-square charge radii against the corresponding modified isotope shifts allows for determination of the mass and field shift factors, as they are equal to the intercept and gradient of a line of best fit, respectively.

In the case of the King plot that uses optical data, the mass and field shift factors are again determined using equation 3.3.14. This equation is used twice; one for each of the two transitions being investigated:

$$\delta v_i^{A,A'} = M_i\frac{A-A'}{AA'} + F_i\delta\left\langle r^2\right\rangle^{A,A'}, \tag{3.4.3}$$

$$\delta v_j^{A,A'} = M_j\frac{A-A'}{AA'} + F_j\delta\left\langle r^2\right\rangle^{A,A'}. \tag{3.4.4}$$

These equations are again multiplied by the modification factor μ:

$$\mu\delta v_i^{A,A'} = \mu M_i\frac{A-A'}{AA'} + \mu F_i\delta\left\langle r^2\right\rangle^{A,A'}, \tag{3.4.5}$$

$$\mu\delta v_j^{A,A'} = \mu M_j\frac{A-A'}{AA'} + \mu F_j\delta\left\langle r^2\right\rangle^{A,A'}. \tag{3.4.6}$$

As the difference in mean-square charge radii is independent of the transition being investigated, the two equations are related by this commonality:

$$\frac{\mu\delta v_i^{A,A'} - M_i}{\mu F_i} = \frac{\mu\delta v_j^{A,A'} - M_j}{\mu F_j}. \tag{3.4.7}$$

A simple rearrangement equation 3.4.7 yields another that resembles the equation of a straight line:

$$\frac{\delta v_i}{F_i} - \frac{M_i}{\mu F_i} = \frac{\delta v_j}{F_j} - \frac{M_j}{\mu F_j}, \tag{3.4.8}$$

$$\therefore \frac{\delta v_j}{F_j} = \frac{\delta v_i}{F_i} - \frac{M_i}{\mu F_i} + \frac{M_j}{\mu F_j}, \tag{3.4.9}$$

$$\therefore \delta v_j = \frac{F_j}{F_i}\delta v_i - \frac{F_j}{F_i}\frac{M_i}{\mu} + \frac{M_j}{\mu}, \tag{3.4.10}$$

$$\therefore \mu\delta v_j = \mu\frac{F_j}{F_i}\delta v_i - \frac{F_j}{F_i}M_i + M_j, \tag{3.4.11}$$

$$\therefore \mu\delta v_j = \frac{F_j}{F_i}\mu\delta v_i + \left[M_j - \frac{F_j}{F_i}M_i\right]. \tag{3.4.12}$$

From the derivation above it becomes clear that by plotting the modified isotope shifts of two transitions against one another, the mass and field shift factors of one transition are determinable, should the factors for the other be known. As in the previous case (see equation 3.4.2), the field shift factor may be determined from the gradient, m, of the line of best fit, and the mass shift factor from the intercept, c:

$$m = \frac{F_j}{F_i}, \tag{3.4.13}$$

and

$$c = M_j - \frac{F_j}{F_i}M_i. \tag{3.4.14}$$

3.5 Spectral Line Shapes

When fitting the hyperfine spectra, it is important that the shapes of the peaks modelled to the data are representative of the line shapes found in nature. For this reason, it is important to understand the phenomena that contribute to the line shape.

3.5.1 The Natural Line Width

Each hyperfine resonance peak will have a natural line width attributed to the lifetime of the decaying state. The lifetime of the state is related to the energy of the transition between two states in accordance with the Heisenberg uncertainty principle:

$$\Delta E \Delta t \geq \frac{\hbar}{2}, \tag{3.5.1}$$

where E is the transition energy, t is the lifetime of the state, and $\hbar$ is the reduced Planck constant. Therefore, the shorter the lifetime of the state, the more enhanced the natural line width will be. The natural line width may be modelled using a Lorentzian line shape. The simplest way to understand why this is to consider an electron moving from one energy state to another via spontaneous emission, where the lifetime of the state is τ. This two-level system may be described by the wave function:

$$\Psi = a_0\Psi_0 + a_1\Psi_1, \tag{3.5.2}$$

where a_0 and a_1 are constants in the absence of any external electromagnetic radiation. When the electron is promoted to the higher energy state, for example via absorption of a resonant photon, a dipole moment is generated, this being the electric dipole moment (change of electromagnetic polarity within the system) associated with the transition between the two states. This dipole moment can be determined using the dipole moment operator [47]:

$$\boldsymbol{M} = \langle\Psi|\,\boldsymbol{d}\,|\Psi\rangle\,. \tag{3.5.3}$$

When considering only the real contributions to the dipole moment, and accounting for the fact that the dipole moment oscillates at the natural transition frequency of the system, ω_{10}, $\boldsymbol{M}$ becomes:

$$\therefore \boldsymbol{M} = 2\boldsymbol{d_{1,0}}a_0a_1\cos(\omega_{10}t), \tag{3.5.4}$$

where $\boldsymbol{d_{1,0}}$ is the transition dipole moment. The amount of population in the higher energy state must decrease as a consequence of spontaneous emission, and accordingly, the magnitude of the dipole moment also decreases, thus behaving as a damped harmonic oscillator:

$$\boldsymbol{M} = \boldsymbol{M_0}e^{-At/2}\cos(\omega_{10}t), \tag{3.5.5}$$

where $\boldsymbol{M_0}$ is the initial amplitude of the oscillating dipole moment and A is the Einstein coefficient, which represents the transition probability per unit time for spontaneous emission [48]:

$$A = 1/\tau. \tag{3.5.6}$$

In order to determine the distribution of frequencies that when summed together give the damped harmonic oscillator waveform a Fourier analysis may be performed. Performing a Fourier transform on the time-dependent part of M gives [47]:

$$F(\omega) = \int_{-\infty}^{\infty} e^{-At/2}\cdot\cos(\omega_{10}t)\cdot e^{-i\omega t})dt \tag{3.5.7}$$

$$\therefore F(\omega) = \frac{1}{2}\int_{0}^{\infty} e^{-At/2}\cdot\left(e^{-i(\omega-\omega_{10}t)} + e^{-i(\omega+\omega_{10}t)}\right)dt \tag{3.5.8}$$

$$\therefore F(\omega) = \frac{1}{2}\left(\frac{1}{A/2 + i(\omega - \omega_{10})} + \frac{1}{A/2 + i(\omega + \omega_{10})}\right), \tag{3.5.9}$$

which to good approximation may be written as:

$$F(\omega) \approx \frac{1}{2}\frac{1}{A/2 + i(\omega - \omega_{10})}, \tag{3.5.10}$$

as when using the rotating wave approximation the non-resonant term is negligible in comparison to the resonant term. The function used to describe the line shape is proportional to the rate at which the oscillating transition dipole radiates power:

$$|F(\omega)^2| \propto \frac{1}{A^2/4 + (\omega - \omega_{10})^2}, \tag{3.5.11}$$

which when normalized using the condition:

$$\int_{-\infty}^{\infty} g(\omega - \omega_{10})d\omega = \int_{-\infty}^{\infty} g(v - v_{10})dv = 1, \tag{3.5.12}$$

gives a Lorentzian profile:

$$g(v - v_{10}) = \frac{A}{(A/2)^2 + 4\pi^2(v - v_{10})^2}, \tag{3.5.13}$$

using the relation

$$v = 2\pi\omega. \tag{3.5.14}$$

The full-width-half-maximum of this function, Δv_l, can be expressed as:

$$\Delta v_l = \frac{A}{2\pi} = \frac{1}{2\pi t}, \tag{3.5.15}$$

and therefore the normalized Lorentzian function may be expressed as:

$$g(v - v_{10}) = \frac{\Delta v_L}{\pi/2(\Delta v_l^2) + 2\pi(v - v_{10})^2}. \tag{3.5.16}$$

This normalized Lorentzian function can be applied to all atoms and ions. For this reason, natural line broadening is referred to as a homogeneous broadening phenomenon [47].

3.5.2 Doppler Broadening

Doppler broadening is an inhomogeneous broadening phenomenon. In the lab frame, an atom with a velocity, u, approaching a laser of fixed frequency, v_s, will achieve resonance at a fre-

quency of v_0. If the atom is travelling with a different velocity, u', its resonance frequency will become v_0' according to the relativistic Doppler transformation:

$$v_0' = \frac{v_0}{1 \pm u'/c}. \tag{3.5.17}$$

In spectroscopy experiments the atoms or ions of interest will have a non-uniform velocity profile for a given axis (in this case the axis of beam propagation), which follows the Maxwell-Boltzmann distribution:

$$\rho_v dv = \left(\frac{m}{2\pi kT}\right)^2 e^{-mv^2/2kT} dv, \tag{3.5.18}$$

where m is the mass of the atom/ion, k is the Boltzmann constant, and T is the temperature of the system. Accordingly, there will be a distribution of resonance frequencies, which correspond to the Maxwell-Boltzmann velocity distribution. The line shape function used to describe this is: [47]:

$$g_D(v - v_0) = \frac{1}{v_0}\left(\frac{mc^2}{2\pi kT}\right)^{1/2} e^{-mc^2(v-v_0)^2/(2kTv_0^2)}, \tag{3.5.19}$$

and the FWHM of this component is taken as:

$$\Delta v_D = 2v_0\sqrt{\frac{2kT\ln(2)}{mc^2}}. \tag{3.5.20}$$

The Doppler line shape function can be written in terms of the FWHM as [47]:

$$g_D(v - v_0) = \frac{2}{\Delta v_D}\sqrt{\frac{\ln(2)}{\pi}} e^{4\ln(2)[(v-v_0)/\Delta v_D]^2}. \tag{3.5.21}$$

An advantage of using collinear laser spectroscopy is that the Doppler contribution to the width of the spectral peaks may be reduced by three orders of magnitude [1]. The act of accelerating the ion bunch in the form of a beam down a beamline results in the distribution of ion velocities along the axis of propagation becoming compressed; as the ions are accelerated to a well-defined energy, the original spread of energies is conserved at the cost of the velocity spread being reduced [41]:

$$\delta v = \frac{1}{\sqrt{2mE}}\delta E. \tag{3.5.22}$$

This principle is illustrated in figure 3.6.

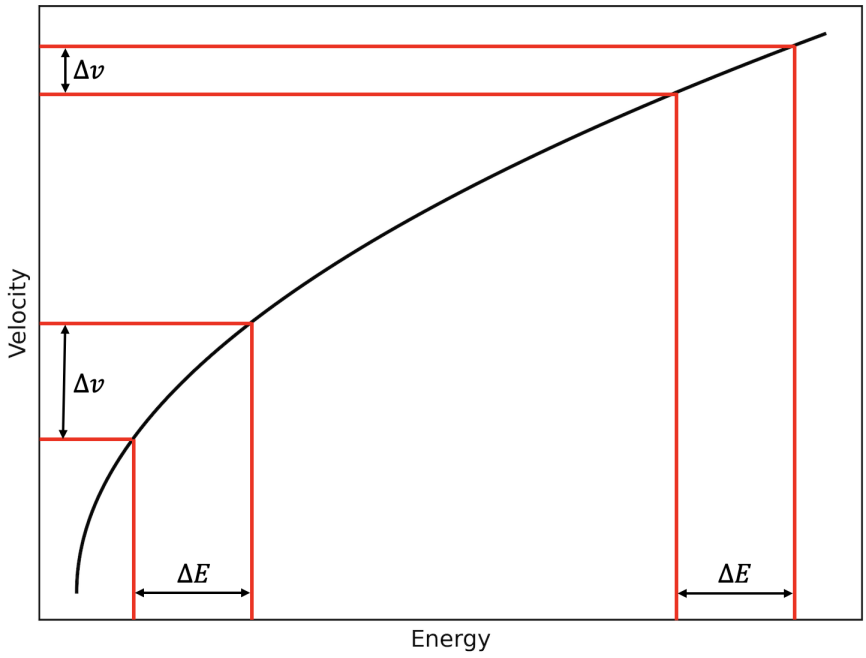

Figure 3.6: A diagram to illustrate how velocity compression is achieved by accelerating ions to higher energies.

3.5.3 Power Broadening

During a laser spectroscopy experiment it is important that an optimal amount of laser power is used - too little and a smaller fraction of the atoms/ions will be excited and fluoresce, which reduces the efficiency of the experiment, too much power and the width of the spectral peaks increases, which reduces the precision to which hyperfine parameters and centroid frequencies can be determined. The broadening of spectral peaks due to this phenomenon is referred to as power broadening.

Power broadening occurs in steady-state systems, for example, the atomic/ionic systems being studied in laser spectroscopy experiments, where an equilibrium between the excitation of electrons into a higher energy state by a continuous-wave laser and the relaxation of electrons via photon emission has been achieved. In this setup, the intensity of the signal detected by the photo-multiplier tube, S, is directly proportional to the population of the excited state, P_2, and the spectral line profile is defined by the measure of de-tuning, Δ:

$$S \propto P_2 = \frac{1}{2} \frac{(I/I_{sat})}{1 + (\Delta/\beta)^2 + (I/I_{sat})}, \tag{3.5.23}$$

where

$$\Delta = v_B - v, \tag{3.5.24}$$

I is the intensity of the laser radiation, I_{sat} is the characteristic saturation intensity for the given transition, β is the width parameter of the weak-excitation limit, v_B is the natural frequency of the transition, and v is the frequency of the laser.

From equation 3.5.23, it can be seen that an increase in the intensity of the laser radiation results in an increase in the width of the spectral profile; this results from the fact that in the presence of a more intense radiation field, the electrons spend a greater proportion of the time in the excited state. The line width is proportional to the range of values Δ can adopt, and this range increases with increasing laser power, thus broadening the spectral peaks [49].

3.5.4 Line Shape Summations

Each of the broadening phenomena contribute to the observed peak profile observed in laser spectroscopy experiments. It should be noted that Doppler broadening in an inhomogeneous phenomenon, which observes Gaussian statistics. In order to be able to model both the Lorentzian and Gaussian natures of the aforementioned broadening phenomena, a Voigt profile may be used to model the spectral peaks.

The Voigt profile is a convolution of both the Lorentzian and Gaussian contributions, and is mathematically defined as [50]:

$$V(x, \sigma, \alpha) = \int_{-\infty}^{\infty} G(x', \sigma) \cdot L(x - x', \alpha) dx'. \tag{3.5.25}$$

The Gaussian and Lorentzian profiles are defined, respectively, as:

$$G(x, \sigma) = \frac{1}{\sigma\sqrt{2\pi}} e^{-x^2/2\sigma^2}, \tag{3.5.26}$$

$$L(x, \alpha) = \frac{\alpha/\pi}{(x^2 + \alpha^2)}, \tag{3.5.27}$$

where

$$\sigma = \frac{\Delta v_G}{2\sqrt{2\ln 2}}, \tag{3.5.28}$$

$$\alpha = \frac{\Delta v_L}{2}, \tag{3.5.29}$$

and Δv_G and Δv_L are the full-width half maxima of the Gaussian and Lorentzian line shapes, respectively.

Chapter 4

Experimental Methodology: The IGISOL-IV Facility

IGISOL is an acronym for **I**on **G**uide **I**sotope **S**eparator **O**n**L**ine, and IGISOL-IV is the fourth generation of the ISOL facility at the University of Jyväskylä. The university has a very well-established accelerator laboratory home to many different experimental setups. The IGISOL-IV facility is located in one of two experimental halls and feeds into five different experimental setups:

- the spectroscopy line (used in various decay spectroscopy experiments and can be equipped with a variety of detectors),
- RAPTOR (**R**esonant ionisation spectroscopy **A**nd **P**urification **T**raps for **O**ptimised spect**R**oscopy,
- JYFLTRAP (a cylindrical double Penning trap mass spectrometer),
- MORA (**M**atter's **O**rigin from the **R**adio**A**ctivity of trapped and polarized isotopes),
- and the laser spectroscopy beamline utilized for this work.

The following discussion will focus on the production of radioactive ions, delivery of said ions to the laser spectroscopy beamline, and the composition of key components used in the experimental setup. Figure 4.1 provides a schematic overview of the IGISOL-IV facility (excluding MORA and RAPTOR).

4.1 Radioactive Ion Production and Extraction

One of the key defining features of the IGISOL facility is its ability to produce isotopes of interest in a chemically insensitive way - this is done within the target chamber. In operation,

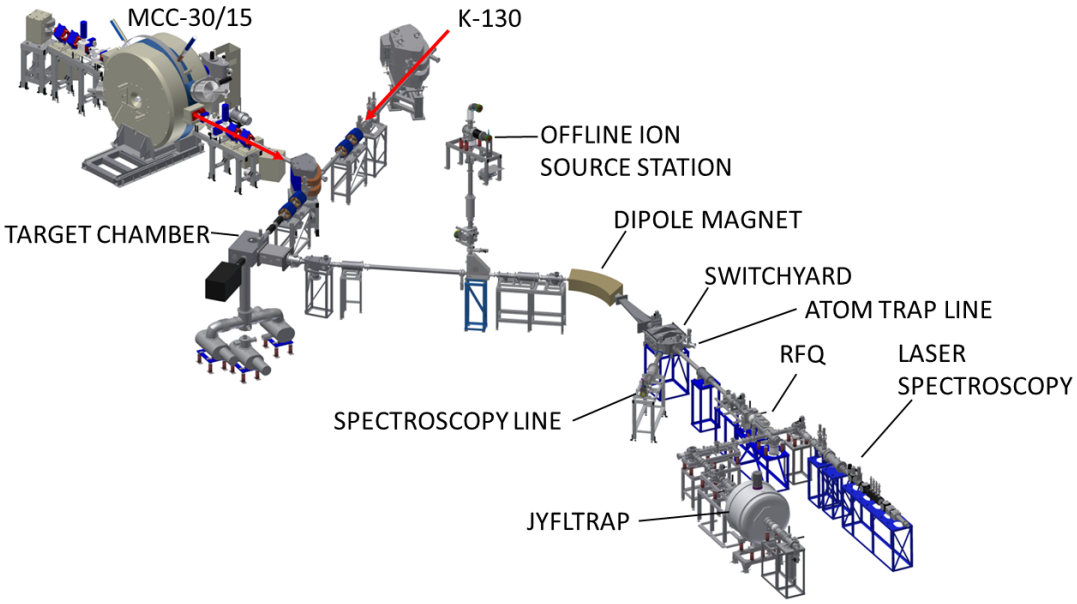

Figure 4.1: A pictorial representation of the IGISOL-IV facility at the University of Jyväskylä. Schematic taken from [51].

a beam of protons is accelerated up to 30 MeV by one of the two cyclotrons employed at the facility, the MCC-30/15 or the K-130, and directed downstream into the target chamber via a series of magnetic quadrupoles and steerers. Figure 4.2 shows a photograph of a magnetic quadrupole used at the facility.

The target chamber comprises a metallic vessel continuously supplied with a stream of helium gas, known as the ion guide. Installed within this chamber is a thin-foil target into which the proton beam is directed. The proton beam has sufficient energy that when impinging onto the target foil the protons are able to overcome the Coulomb repulsion of the atoms in the target material and induce nuclear reactions.

The advantage of using a thin-foil target as opposed to a thick target, and the underlying reason that IGISOL produces isotopes in a chemically insensitive way, is that the reaction products are able to recoil directly out of the target and into the target chamber. When using a thick target, the reaction products do not have sufficient energy to recoil out of the material, and instead, the target material must be baked to achieve extraction; this results in longer extraction times, which prevents measurements from being made on isotopes with short half-lives. Additionally, as the pathway out of a thick target is longer there is more opportunity for reaction products to collide with atoms in the lattice of the target material, reducing their kinetic energies and increasing the likelihood of the reaction products getting trapped within the material. This trapping effect may be enhanced further depending on the chemical properties of both the re-

action product and target material.

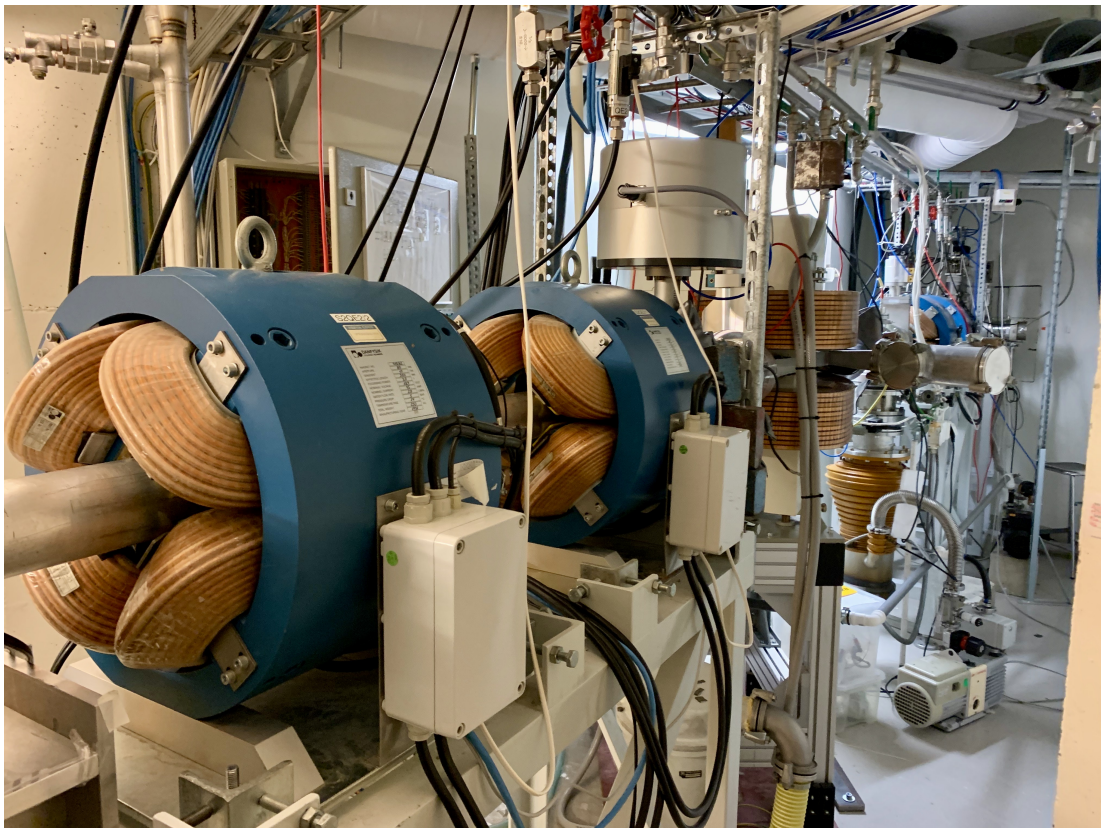

Figure 4.2: A photograph of a magnetic quadrupole used to steer protons/ions from the K-130 cyclotron to the target chamber of the IGISOL.

Three targets were used in this investigation; a natural chromium target, a ^{50}Cr enriched target, and a ^{54}Cr enriched target. As noted previously, the isotopic abundances of natural chromium are: 4.345(13)% ^{50}Cr, 83.789(18)% ^{52}Cr, 9.501(17)% ^{53}Cr, and 2.365(7)% ^{54}Cr [4]. The lighter radioactive isotopes investigated in this work (^{48}Cr, ^{49}Cr, and ^{51}Cr) were produced by impinging protons onto the natural chromium target and ^{50}Cr enriched target. Attempts to measure the hyperfine structure of ^{55}Cr were also made as part of this work, and this isotope was produced by impinging deuterons onto the ^{54}Cr enriched target.

The reaction products that recoil out of the target have a range of kinetic energies and charge states. This is unsuitable for ion manipulation as the kinematic properties of each ion differs. This would result in a multitude of ion trajectories. Collisions between the reaction products and the helium buffer gas act to thermalise the reaction products whilst simultaneously putting many of them in a singly charged state. The improved uniformity of these properties makes ion manipulation more consistent amongst the reaction products. The buffer gas-reaction product

amalgam is then extracted from the target chamber via a 1 mm aperture in the form of a supersonic gas jet, and into a radio-frequency sextupole ion beam guide henceforth referred to as the SPIG.

The SPIG is formed from two combined segments, each of which houses six cylindrical rods arranged in a hexagonal structure. The cylindrical rods have oscillating, radio-frequency voltages applied to them. One segment of the SPIG is enclosed in order to maintain high pressure and collimate the gas jet, whereas the other is open and allows for the buffer gas and other neutral artefacts to be pumped away through the gaps between the rods using a series of Roots blowers. Direct current potentials may be applied to each segment of the SPIG to create an increasingly negative voltage gradient that efficiently guides positive ions downstream. Electrodes are located at either end of the SPIG, the upstream electrode is referred to as the 'repeller' and the downstream electrode is referred to as the 'end electrode'. These electrodes are used to optimise transport through the SPIG by preventing ions from escaping [52]. The SPIG forces the ions along a central axis, reducing their transverse emittance and thus forcing the ions into a beam profile. This ion beam is then focused using a conical Einzel lens and subsequently directed down the beamline where it is accelerated to 30 keV by a potential applied to the IGISOL platform. The processes of isotope production and beam formation are illustrated in figure 4.3.

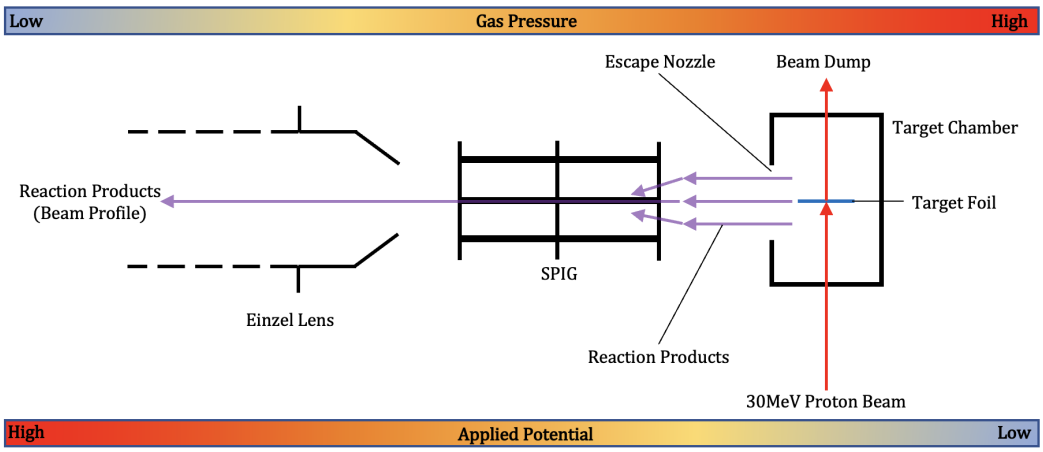

Figure 4.3: A pictorial representation of how a beam of reaction products is formed using the SPIG and the conical Einzel lens following isotope production in the target chamber.

4.2 The Offline Sources

In addition to the online cyclotron sources, there are also a number of offline sources that may be used to produce ions of interest. These ions are typically stable or long-lived and do not

need to be produced by inducing nuclear reactions. The offline sources are particularly useful when setting up for an experiment; for example by producing a sufficient number of ions for diagnostic beam tuning, and when investigating the efficiencies and sensitivity to nuclear properties of different fine structure transitions. Time using the online sources must be applied for in advance and is very costly, thus having readily available offline sources maximises the time during an experiment spent collecting data of interest. Furthermore, the stable isotopes produced by the offline sources may be used as reference ions during online experiments. By frequently checking the centroid positions of the reference spectra, it is possible to determine if any systematic drifts of the tuning voltage or laser frequency are occurring.

One of the most commonly used offline sources is the spark ion source. In this setup a needle made of the isotope of interest, and contained within a chamber filled with helium gas, is connected to the cathode of a high-voltage power supply. The high potential leads to sparking events which ionise the helium atoms. The helium ions are accelerated by the potential towards the needle cathode, causing ions of interest to be sputtered from the needle. These ions are then extracted and accelerated down the beamline in the same manner as for the online sources.

Although such offline sources can be placed within the IGISOL for preparatory tests, an alternative offline source is the ion source station located on the second floor of the facility, an illustration of which is provided in figure 4.4. The ion source station can house 3 different ion sources, two on the horizontal plane and one on the vertical, and currently houses a range of discharge sources. In operation, the ions produced by either source are guided by a skimmer electrode, which gives them a beam profile, before being injected into a quadrupole bender and subsequently focused by an Einzel lens. Steering electrodes are used to align the beam and transport it to a 90 degree deflector located on the first floor, which itself then deflects the beam onto the horizontal plane where the ions may be transported into the beamline [53].

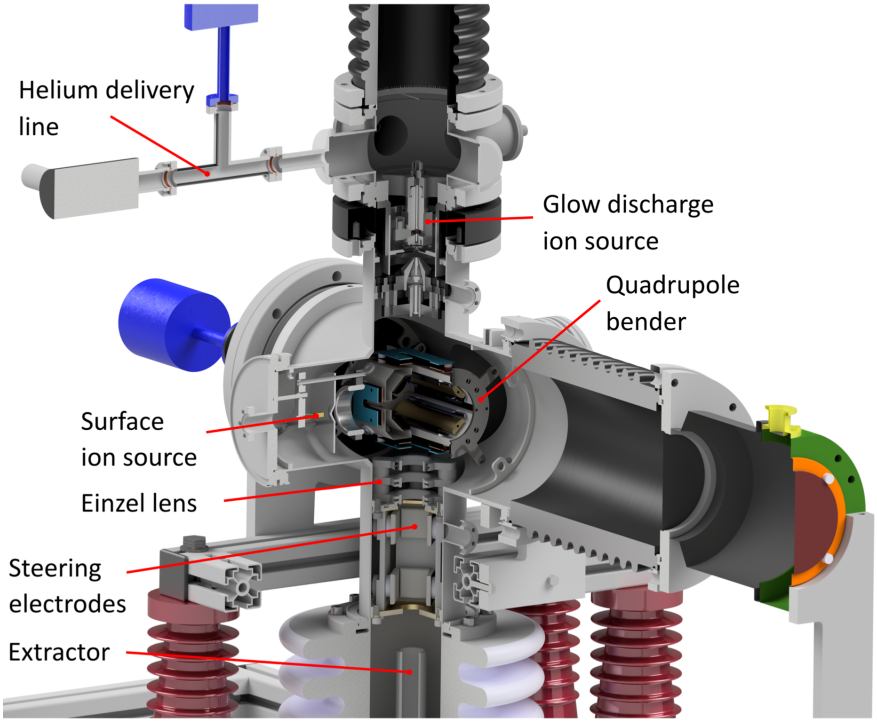

Figure 4.4: A render of the internals of the offline ion source station. Taken from Vilen *et al.* [53].

4.3 Isotope Separation

The ion beam extracted from the target chamber and directed down the beamline is a cocktail beam, meaning that it is not isotopically pure. As such, it is necessary to separate the ions of interest from the remainder of the beam prior to them being directed to the experimental stations. This is achieved using a bender: a 55 degree dipole separator magnet.

Ions in a magnetic field experience a force perpendicular to the direction of the magnetic field and their velocity, meaning that the ions follow a curved path. The centripetal force experienced by an ion of mass m with charge q, propagating through a magnetic field of strength B, at a velocity v is given by:

$$F = qvB = \frac{mv^2}{r}, \tag{4.3.1}$$

$$\therefore r = \frac{mv}{qB}, \tag{4.3.2}$$

where r is the radius of the path the ion follows. The kinetic energy of the ion is equal to the product of the charge of the ion and the acceleration voltage, V, supplied to the ion:

$$qV = \frac{mv^2}{2}, \tag{4.3.3}$$

$$\therefore v = \sqrt{\frac{2qV}{m}}. \tag{4.3.4}$$

Hence substituting equation 4.3.4 into equation 4.3.2 gives:

$$r = \sqrt{\frac{2V}{B^2} \cdot \frac{m}{q}}. \tag{4.3.5}$$

From equation 4.3.5, it becomes apparent that for an ion with a given mass-to-charge ratio, the radius of the arc that the ion follows can be dictated by the strength of the magnetic field. This phenomenon can be exploited using the bender to selectively deflect ions of interest downstream, whilst deflecting ions with other mass-to-charge ratios into a beam dump. This principle is illustrated in figure 4.5.

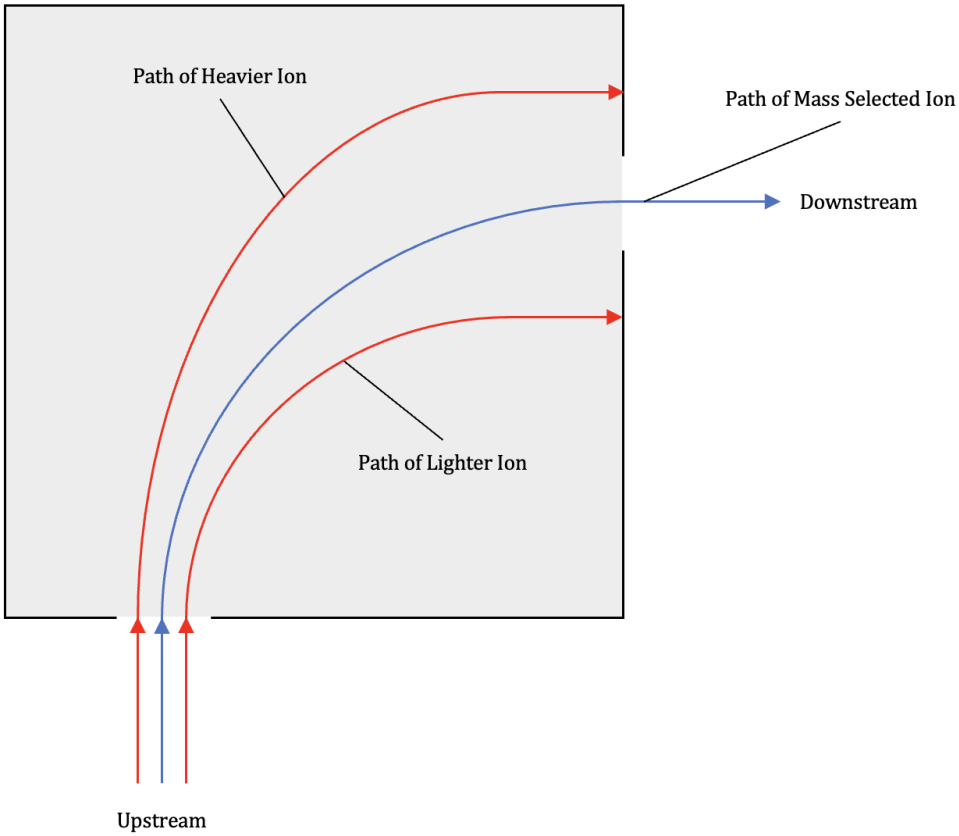

Figure 4.5: A diagram to show how mass selection is achieved using a bender magnet. At IGISOL the bender deflects ions of interest by 55 degrees rather than 90 degrees as illustrated in this figure.

4.4 The Cooler-Buncher

Directly downstream from the bender is a radio-frequency cooler-buncher. The cooler-buncher comprises a gas-filled radio-frequency quadrupole positioned atop a high-voltage platform but biased a couple of hundred volts lower than the +30 kV IGISOL platform potential. This arrangement means that the positively charged ions are repelled and accelerated down the beamline by the positive IGISOL platform potential, before again being repelled but decelerated by the slightly less positive high-voltage platform. This mechanism ensures that the ions have sufficient kinetic energy to drift into the cooler-buncher, but not so much that cooling and bunching would not be possible. The quadrupole itself is made of four stainless steel rods which have a radio-frequency voltage applied to them. Each rod is divided into sixteen segments. At the inlet of the quadrupole is a pair of cylindrical electrostatic lenses used to focus the ions beam as they enter. Located at the outlet of the cooler-buncher is an end-plate electrode, and an intersecting, smaller, secondary quadrupole, which maintains the transverse emittance of the ions before they are released to a high-vacuum further down the beamline.

The cooler-buncher is filled with a low-pressure helium buffer gas. Interactions with this gas thermalise the ions as they are directed downstream to a 'trapping region' by an axial field applied along the length of the cooler-buncher. Within the trapping region, a stronger axial field gradient is applied to the ions by the last two segments of each rod and the secondary quadrupole. A +20 V potential can be applied to the end-plate electrode which produces a potential well used to trap ions into bunches. Lowering the end-plate potential to 0 V releases the bunched ions. Typically, ions will be accumulated for around 100 ms before the bunched ions are released; the end-plate voltage will be set to 0 V for 100 μs, producing bunches with a temporal width of 10-20 μs [54]. Figure 4.6 demonstrates how the trapping potential is used to accumulate ions into bunches.

There are two key advantages of using cooled ion bunches in laser spectroscopy experiments. Firstly, as the bunches have a limited temporal width, a time gate may be applied to the recorded data. This time gate corresponds to the time period during which the ion bunch was passing directly in front of the photo-multiplier tube used to detect photons. This method, therefore, allows for suppression of background statistics in the measured spectra, which may be attributed to scattered laser photons, and has been shown to reduce the background statistics by up to four orders of magnitude [55]. Time-gating will be discussed in more detail in a subsequent chapter.

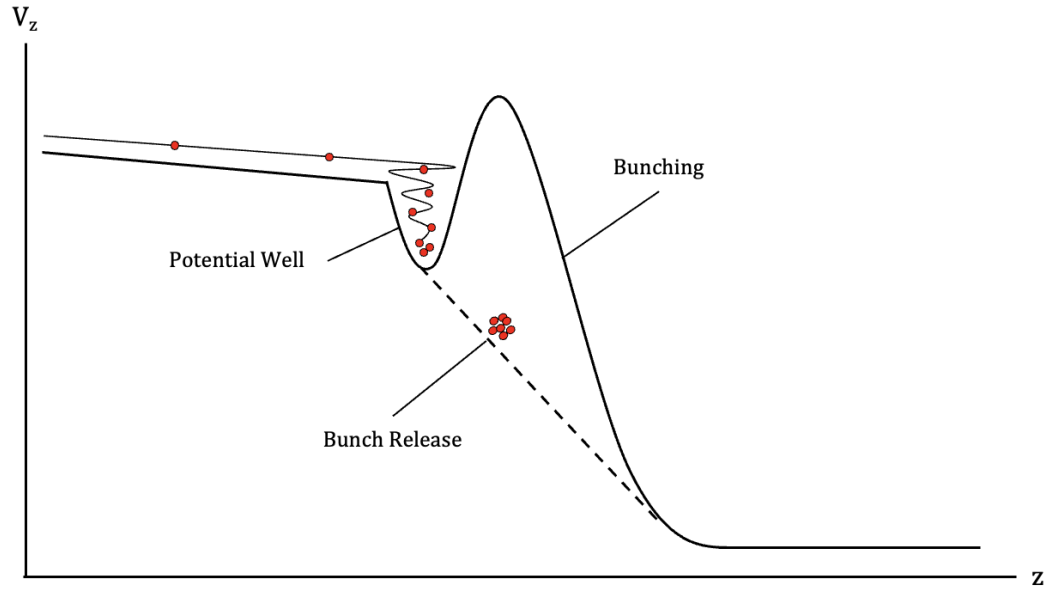

Figure 4.6: A pictorial representation of how a trapping potential is used to accumulate ions into bunches in the cooler-buncher.

The second advantage of using the cooler-buncher is a natural consequence of reducing the kinetic energy of the ions; the Doppler broadening of spectral peaks is reduced:

$$E = \frac{1}{2}mv^2, \tag{4.4.1}$$

$$\therefore \frac{dE}{dv} = mv, \tag{4.4.2}$$

$$\therefore \Delta E = mv\Delta v. \tag{4.4.3}$$

A reduction in the spread of the ions' kinetic energies achieved by cooling directly corresponds to a reduction in the velocity spread of the ions, which accordingly reduces the Doppler broadening of the resonance peaks and improves emittance for beam transport.

4.5 The Laser Spectroscopy Line

Once extracted from the cooler, the ion bunch can be directed to the laser spectroscopy line. A schematic overview of the laser spectroscopy beamline is provided in figure 4.7. A laser beam of fixed frequency is directed upstream from the laser cabin along the beamline. The laser beam

and ion bunches overlap one another but propagate in opposite directions. This is an anti-collinear geometry, hence the technique is referred to as 'anti-collinear laser spectroscopy'. The 'anti' prefix is often neglected, despite the fact that 'collinear laser spectroscopy' also exists, where the laser beam and ion beam co-propagate in the same direction. The main components of the laser spectroscopy line are the acceleration electrodes, the charge-exchange-cell (CEC), the light interaction region, and the laser cabin.

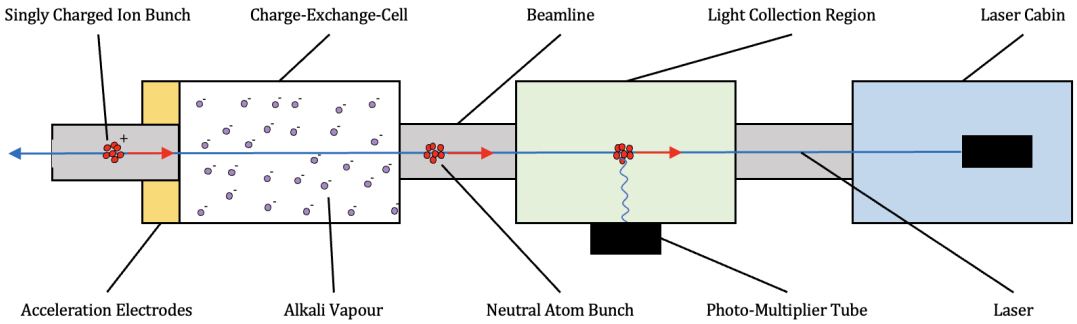

Figure 4.7: A schematic representation of the elements that form the laser spectroscopy line. The acceleration electrodes and laser cabin are positioned at the upstream and downstream ends of the beamline, respectively.

On the laser line ion bunches are decelerated or accelerated by a tuning potential applied to electrodes upstream from the charge-exchange-cell and to the cell itself. This tuning potential is variable and is altered through a pre-specified range of voltages during a resonance scan. This is because resonances are detected (and hyperfine spectra mapped) by Doppler tuning the frequency of the laser in the reference frame of the atom by applying this tuning voltage. The total voltage applied to the ion is equal to the cooler voltage minus the tuning voltage. Consequently, the ions may be accelerated or decelerated by the tuning voltage according to its polarity, thus providing access to a range of laser frequencies in the reference frame of the atom despite the the frequency of the laser in the lab frame remaining the same. Accordingly, if one were to scan through a range of tuning voltages, one voltage increment per bunch of ions, each bunch would experience a different frequency of laser light. Resonances (the absorption and subsequent emission of a photon by an atom/ion) will be achieved when the observed frequency of the laser corresponds to the energy of a hyperfine transition. Therefore, one can map the hyperfine structure of an atom/ion by measuring the number of photons detected by the photo-multiplier tube as a function of the tuning voltage applied to the ion bunch. To ensure that a sufficient number of counts are detected to form a spectrum, sweeps through the tuning voltage range are repeated many times for any given measurement.

4.5.1 The Charge-Exchange-Cell

The charge-exchange-cell is mounted upon an electrically insulated platform, which allows a tuning potential within $\pm 4\,\mathrm{kV}$ to be applied to the cell for Doppler tuning the ions before neutralisation. The cavity of the charge-exchange-cell is filled with a low-pressure alkali vapour (typically sodium or potassium), which acts to neutralise the ions as they move downstream to the light interaction region.

The charge-exchange process is utilised when atomic transitions need to be studied rather than ionic transitions; the energies required to probe their ionic electron structure may be inaccessible/inconvenient using the photon energies producible using the laser, or the ionic transitions available may not be sensitive to the nuclear properties. The spectral peaks obtained when measuring ions are symmetric, whereas those obtained when measuring neutralised atoms often exhibit an asymmetry. Symmetric profiles are preferable because the process of fitting models to the spectra is simplified, however for the reasons discussed above it is not always preferable to study ionic systems. This is the case for chromium and in this experiment the chamber of the charge-exchange-cell was filled with low-pressure potassium vapour to facilitate neutralisation. As such, it is important to understand the mechanisms that cause the asymmetry so that it may be accounted for it when fitting models to the spectra.

There are two mechanisms by which the incoming ions may be neutralised: ground-state charge exchange and excited-state charge exchange. Examples of these mechanisms are as follows:

Ground-state charge exchange mechanism:

$$\mathrm{Cr}^{+} + \mathrm{K} \rightarrow \mathrm{Cr}_{(\mathrm{Ground\ State})} + \mathrm{K}^{+} - \delta\mathrm{E}. \tag{4.5.1}$$

Excited-state charge exchange mechanism:

$$\mathrm{Cr}^{+} + \mathrm{K} \rightarrow \mathrm{Cr}_{(\mathrm{Excited\ State})} + \mathrm{K}^{+} - (\delta\mathrm{E} + \Delta\mathrm{E}). \tag{4.5.2}$$

If direct population of the ground state is achieved via the ground-state mechanism, a small amount of kinetic energy corresponding to the difference between the ionisation potentials of chromium and potassium, δE, is taken from the beam. Regardless of which charge-exchange pathway is taken this loss will occur, therefore this energy loss does not manifest itself as a source of asymmetry in the spectra. Alternatively, via the excited-state mechanism, the ground

state is populated indirectly as an excited neutral atom is produced. As the excited state electron relaxes to the ground state, it emits a photon with an energy corresponding to the energy separation of the two states, ΔE, and an equivalent amount of energy is taken from the kinetic energy of the beam in addition to δE [56].

Accordingly, through this excited-state pathway, a subset of the atoms in the beam have less kinetic energy and require additional acceleration before they achieve resonance; a higher tuning voltage is therefore required. This excited-state exchange phenomenon manifests itself in a spectrum as an asymmetry of the resonance peaks, which is caused by unresolved 'satellite peaks' in the spectra. The frequency offset between the resonance peak and a satellite peak corresponds to the difference in energies between the electronic ground state and the excited state occupied during neutralisation. These satellite peaks become particularly pronounced at high vapour pressures and temperatures, which result in more significant peak asymmetries. If these satellite peaks are left unaccounted for they may result in an incorrect determination of the hyperfine parameters and centroid positions of the spectra in the fitting process.

The probability, P, that upon neutralisation an electron will occupy an excited state is modelled using Poisson statistics:

$$P = \frac{\lambda^k e^{-\lambda}}{k!}, \tag{4.5.3}$$

where λ is the expected rate of occurrence, e is Euler's number, and k is the number of occurrences.

It is possible that satellite peaks may be present in the spectra of this work as a result of these excited-state charge exchange mechanisms. In order to address this, analysis has been performed to determine how these satellite peaks should be accounted for when modelling the hyperfine spectra.

4.5.2 The Light Interaction Region

Once neutralised, the atoms drift downstream and into the light interaction region. The light interaction region is formed of a vacuum chamber and a photo-multiplier tube. The inside of the chamber is painted black to minimise the number of photon scattering events detected by the photo-multiplier tube. Resonance photons emitted by fluorescing atoms are focused into the photo-multiplier tube by a series of lenses.

In order to maximise the resonance detection rate, it is necessary to maximise the number of atoms interacting with the laser. This is achieved by optimising the ion/atom delivery rate down the beamline, and ensuring that the beam and laser beam are aligned and overlapping one another. Alignment is achieved using a series of three apertures positioned in parallel to one another. Two adjustable apertures are located within the laser cabin directly downstream from the entrance to the light interaction region. A third aperture, with a 1 mm fixed diameter, is positioned within the light-interaction region. The third aperture can be manually lowered into (and raised out of) the light interaction region. Alignment of the laser beam is achieved by tuning the angles of steering mirrors within the laser cabin so that the path of the laser beam intersects all three apertures.

A series of detectors are positioned throughout the beamline and are used to maximise the ion beam transport efficiency. The voltages of steering electrodes positioned along the beamline are manually adjusted and the number of ions/atoms detected is monitored using either Faraday cups, a silicon detector, or a MagneToF detector. The transport efficiency is maximised by tuning the steering electrodes sequentially, starting from the upstream end of the IGISOL and ending at the laser spectroscopy line. Finally, to maximise the overlap between the atom/ion beam and the laser, the alignment of the beam is tuned through the 1 mm aperture located in the light interaction region using the MagneToF detector. The 1 mm aperture is raised out of the path of the atoms/ions/laser prior to measurements being taken.

4.6 Laser Light Production

As mentioned previously, a tuning voltage is applied to the ions of interest prior to neutralisation in the charge-exchange-cell to Doppler tune them into resonance with the laser. The laser light can only be Doppler tuned through a relatively small range of frequencies, so it is key that the frequency of the light produced by the laser is as close to the desired range of frequencies as possible. The laser used in this series of experiments was a continuous-wave titanium-sapphire laser (Matisse 2 TiSa), henceforth referred to as the TiSa. The TiSa was pumped using a neodymium-doped yttrium aluminium ($Nd:Y_3Al_5O_{12}$) laser; henceforth referred to as the 'Nd:YAG'. The laser light produced by either laser is directed along the desired path using a series of specialised optics, which are optimised to reflect light within a specific range of frequencies.

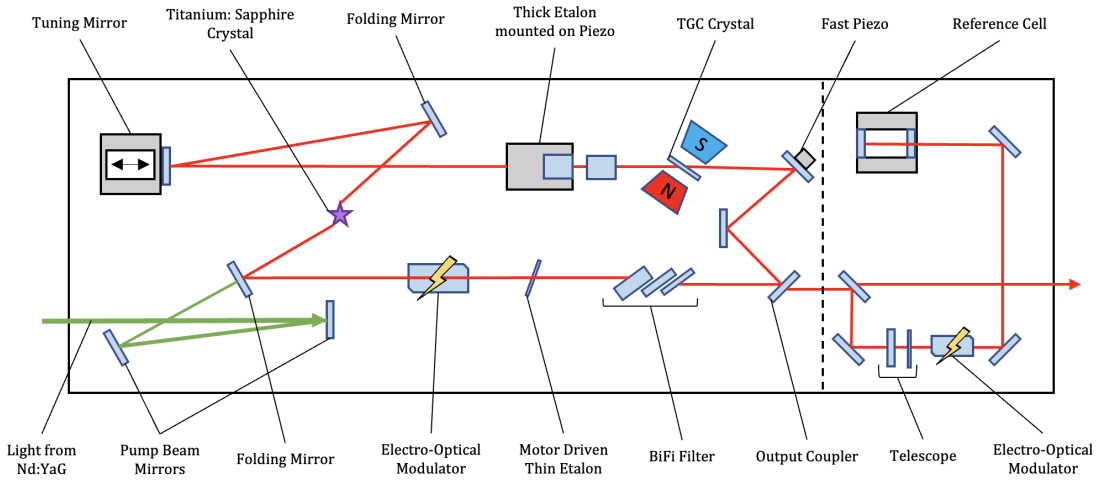

Figure 4.8: A pictorial representation of the elements of Matisse 2 TiSa laser system. The diagram illustrates how the laser light interacts with each element and cycles within the cavity [57].

With reference to figure 4.8, it can be seen that pump laser light from the Nd:YAG enters the Matisse TiSa 2 laser box (from the left) and is reflected off of a series of pump beam mirrors, which deflect the pump laser into the TiSa crystal through the backside of a folding mirror. Once the pump laser has been focused into the TiSa crystal it will begin fluorescing. The pump laser ensures that the number of electrons occupying a meta-stable energy state is larger than the number of electrons occupying the ground state of the lasing medium. This is known as population inversion and is a condition that must be maintained for sustained stimulated emission to take place. The fluorescent light produced is cycled within the laser cavity resulting in the amplification of the power of the laser light. An output coupler is integrated into this cycling pathway and allows a fraction of the light to exit the laser head whilst reflecting the rest back into the laser cavity. Following amplification via the crystal, the folding mirrors are used to align the rays of laser light parallel to one another. A thin etalon, a birefringent (BiFi) filter and a thick etalon all act as band-pass filters to ensure that the correct cavity mode is achieved so that the TiSa outputs a laser beam with the desired wavelength. A tuning mirror (TM) is attached to a piezo and is movable in order to change the length of the cavity, which fine-tunes the wavelength of the selected lasing mode.

During operation it is possible for the wavelength of the laser to drift. This may be caused by thermal expansions, mechanical interference, changes in humidity/air pressure etc., all of which may change the optical properties or relative positions of the individual components of the laser, and hence the frequency of light the laser produces. To mitigate frequency drifts some of the laser light is reflected into a reference cell, which comprises a highly stable, scannable

optical resonator that behaves as an external frequency reference. The intensity of transmitted light from the reference cell observes an Airy-function and the frequency of the laser is set to correspond to a point on one of the fringes of a transmission resonance peak. If the frequency of the laser drifts, the transmission intensity will change and control signals will be directed to the tuning mirror piezo and another piezo actuator (the fast piezo) upon which a second laser resonator mirror is mounted. The piezo then respond accordingly to counteract the change in transmission intensity and corresponding frequency drift. This is known as "side-of-fringe" frequency stabilisation [57].

The emission spectrum producible by the TiSa laser spans a range between 662 nm to 1050 nm [58]. As mentioned above, the birefringent filter, henceforth referred to as the 'BiFi', the thick etalon, and the thin etalon are the components used for frequency selection [57]. Frequency selection using these elements is illustrated in figure 4.9.

The BiFi is a broad-range tuning element and dictates the approximate wavelength output by the Matisse by narrowing down the band of frequencies in which lasing modes may exist to several hundred GHz. Formed from three plates with differing thicknesses, the BiFi uses the phenomena of birefringence and the polarization selective property of the laser resonator for selection. In operation, as the laser light passes through the BiFi its polarisation becomes rotated, the amount of rotation is dependent on the wavelength of light. Accordingly, the BiFi may be tuned so that all wavelengths of light bar the desired wavelength become elliptically polarised. The elements of the BiFi are mounted at the Brewster's angle, and as such light that is not linearly polarised in the correct plane suffers reflection losses during transmission through the filter.

To further reduce the number of laser modes output by the TiSa, the thin and thick etalons are used. The thick etalon is formed from two reflective surfaces which sit parallel to one another and are separated by an air space. The distance between the surfaces is adjustable. The thin etalon has a similar composition but differs in construction as it is a single composite optic, and therefore the distance between the reflective surfaces is fixed by a solid connective medium. In operation, incident light with wavelengths of $n\lambda = 2d$, where d is the separation between the partially-reflective surfaces, are transmitted through each etalon, and all other wavelengths of light destructively interfere.

It is often the case that the wavelength of the transition being studied lies beyond the emission

spectrum of the lasing material. This is the case in this experiment as the 358 nm and 425 nm transitions do not fall within the 662 nm to 1050 nm range producible using the TiSa. For this reason, it is necessary to 'frequency double' the laser light to ensure that the energy of the laser photons corresponds to the resonances being studied. To do this a frequency-doubling crystal contained within a cavity is introduced into the experimental setup. The doubling crystal, which is a non-linear medium, is capable of doubling the frequency of the light incident upon it. This is achieved by a phenomenon known as "second harmonic generation" [59].

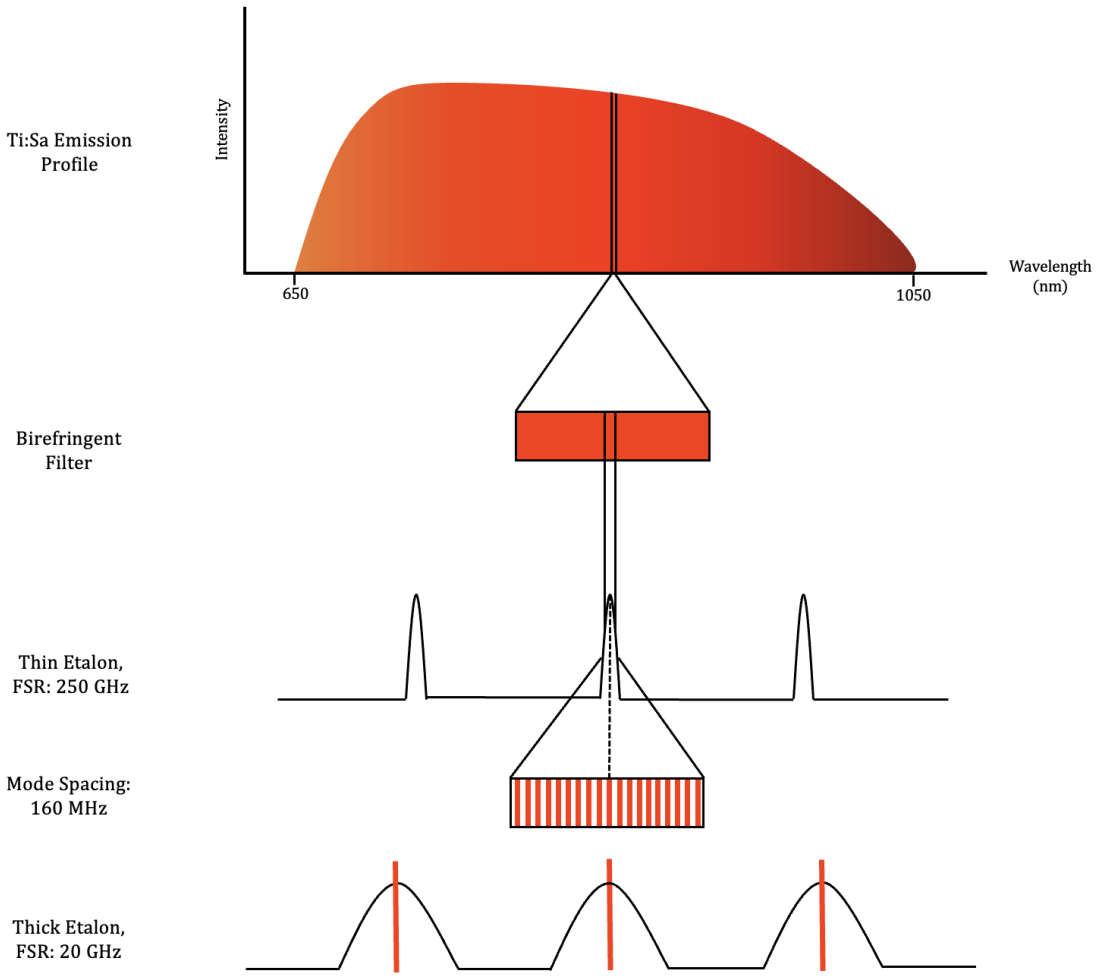

Figure 4.9: An illustration of how frequency selection is achieved from the broad spectrum produced by the TiSa, using the birefringent filter, thick etalon, and thin etalon. This is a re-illustration of a figure provided in the Matisse TiSa 2 user guide [57].

Second harmonic generation can be understood in terms of polarisation in a non-linear dielectric material. When a source of laser light is incident upon a dielectric material, the electric field of the laser photon interacts with charges in the material, displacing them and thus inducing secondary electric fields. This is known as polarisation, P. The magnitude of P can be expressed

in terms of a power series of the initial electric field strength E:

$$P = \epsilon_0 \chi^{(1)} \mathbf{E} + \epsilon_0 \chi^{(2)} \mathbf{EE} + \epsilon_0 \chi^{(3)} \mathbf{EEE} + ... \tag{4.6.1}$$

where ϵ_0 is the permittivity of a vacuum, χ^n is the electric susceptibility of a dielectric material, and $\mathbf{E}$ is the wave equation of an electric field. Substituting the following wave equation into the polarisation power series demonstrates how frequency doubling occurs in such a material:

$$\mathbf{E} = \boldsymbol{E_0} \cos(kz - wt), \tag{4.6.2}$$

$$\therefore \boldsymbol{EE} = \boldsymbol{E}^2 = \boldsymbol{E_0}^2 \cos^2(kz - wt) = \frac{1}{2} \boldsymbol{E_0}^2 [1 + \cos(2kz - 2wt)], \tag{4.6.3}$$

$$\therefore P = [\epsilon_0 \chi^{(1)} \boldsymbol{E_0} \cos(kz - wt)] + [\frac{1}{2} \epsilon_0 \chi^{(2)}] + [\frac{1}{2} \epsilon_0 \chi^{(2)} \boldsymbol{E_0} \cos(2kz - 2wt)]. \tag{4.6.4}$$

The third term of the polarization expansion shows that a second order harmonic with frequency $2w$ is generated (i.e production of a photon with double the frequency of the incident light). In physical terms, this process can be understood as a photon of frequency w entering the non-linear dielectric and polarising the material by inducing oscillating dipoles, some of which oscillate with a frequency $2w$, and thus emit photons with frequencies that match the dipole oscillation frequency.

Chapter 5

Experimental Campaigns

For this investigation, three separate experimental campaigns were undertaken:

- An offline campaign performed in June 2020,
- An online campaign performed in January/February 2021 (henceforth referred to as the January 2021 campaign),
- A second offline campaign performed in July 2021.

5.1 June 2020 Offline Experimental Campaign

The purpose of this preliminary experimental series was to test the efficiencies of various atomic transitions in chromium in preparation for an online campaign. In order to be able to use the cyclotron facilities at the IGISOL facility, one must apply for a limited amount of time in advance, therefore it is necessary to investigate which transitions are the most suitable to be studied well in advance as setting up and optimising the laser to study a particular transition can be a time-consuming process. Measurements of 8 different transitions were made during this campaign, the details of which are presented in table 5.1. When deciding which transitions may be suitable candidates for study many different factors are considered, for example, transitions with high Einstein-A coefficients and highly populated lower states are desirable as these factors influence the spectroscopic efficiency. Furthermore, the number, and therefore relative intensities of the resonance peaks in a spectrum is dictated by the J values of each state and the nuclear spin, I. Fitting models to the spectra becomes increasingly difficult if resonance peaks are low-intensity or poorly resolved, so these factors must also be taken into account when considering the objectives of the experiment.

Table 5.2 shows which stable isotopes were measured on each line, and figure 5.1 shows samples of the spectra measured for ^{53}Cr on each line. ^{53}Cr is the only stable isotope of chromium which produces a hyperfine spectrum due to it having a non-zero spin ($I = 3/2$), the remaining stable isotopes (^{50}Cr, ^{52}Cr and ^{54}Cr) produce a single fine structure peak as they are spin-zero and therefore do not have hyperfine structures.

Transition (nm)	Lower State	Lower State Energy (cm^{-1})	Upper State	Upper State Energy (cm^{-1})	Efficiency Rank
429	$3d^5(^6S)4s\ ^7S_3$	0	$3d^5(^6S)4p\ ^7P_2$	23305.0026	6
427	$3d^5(^6S)4s\ ^7S_3$	0	$3d^5(^6S)4p\ ^7P_3$	23386.3419	4
425	$3d^5(^6S)4s\ ^7S_3$	0	$3d^5(^6S)4p\ ^7P_4$	23498.8156	2
361	$3d^5(^6S)4s\ ^7S_3$	0	$3d^4(^5D)4s4p(^3P)\ ^7P_2$	27728.811	3
359	$3d^5(^6S)4s\ ^7S_3$	0	$3d^4(^5D)4s4p(^3P)\ ^7P_3$	27820.1975	5
358	$3d^5(^6S)4s\ ^7S_3$	0	$3d^4(^5D)4s4p(^3P)\ ^7P_4$	27935.2412	1
301	$3d^4 4s^2\ ^5D_4$	8307.5753	$3d^4(^5D)4s4p(^1P)\ ^5D_3$	41575.099	8
300	$3d^4 4s^2\ ^5D_3$	8095.1842	$3d^4(^5D)4s4p(^1P)\ ^5D_2$	41408.9840	7

Table 5.1: A table of the atomic transitions in chromium investigated in the June 2020 offline campaign. Information from the National Institute of Standards and Technology spectral line database [39].

Isotope (A)	429 nm	427 nm	425 nm	361 nm	359 nm	358 nm	301 nm	300 nm
^{50}Cr	✓	✓	✓	✓	✓	✓	✗	✗
^{52}Cr	✓	✓	✓	✓	✓	✓	✓	✓
^{53}Cr	✓	✓	✓	✓	✓	✓	✗	✗
^{54}Cr	✓	✓	✓	✓	✓	✓	✗	✗

Table 5.2: A table showing the isotopes that were measured for each atomic transition during the June 2020 offline campaign.

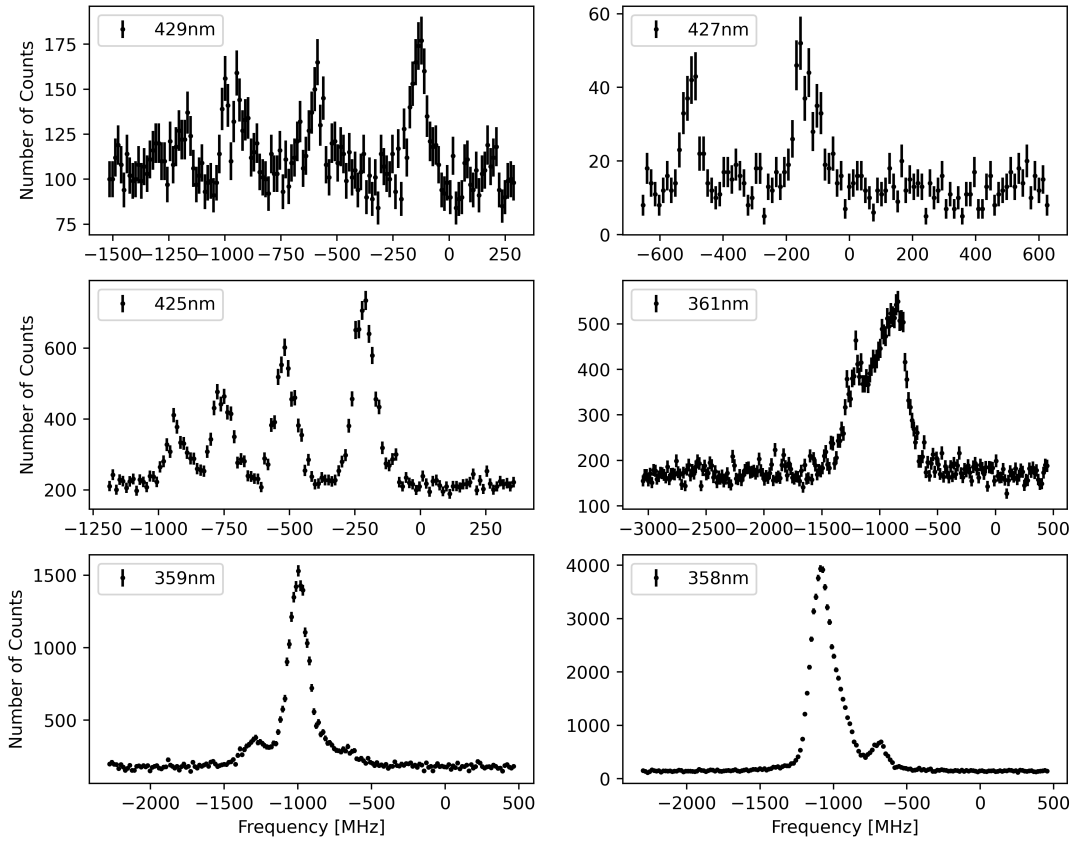

Figure 5.1: Plots to show examples of the spectra produced when measuring ^{53}Cr using each atomic transition.

The efficiencies of each spectral line were determined by calculating the ratio between the resonance count rate and the rate of atoms passing through the beamline. The number of atoms present at the end of the beamline was determined using a MagneToF detector; this is a highly sensitive time-of-flight ion detector capable of measuring beam currents in the sub-pA range. The resonance rate and rate of atoms passing through the beamline were calculated using the following equations:

$$\text{Resonance rate} = \frac{\text{Max channel counts} - \text{Background}}{\text{Dwell time} \cdot \text{No. of scans} \cdot \text{No. of bunches released per step}}, \tag{5.1.1}$$

$$\text{Atom count rate} = (\text{Count rate} - \text{ Background rate}) \cdot \text{K}_{\text{sf}}. \tag{5.1.2}$$

The MagneToF device is highly sensitive, and for this reason, it cannot be exposed to the full number of atoms used in a typical resonance scan without potentially being damaged. During a resonance scan, the MagneToF is raised out of the beamline so that the full fraction of atoms

may be utilized, whereas when it is lowered into the beamline it is necessary to reduce the number of atoms reaching the laser-spectroscopy line. This is achieved by de-tuning optics along the beamline leading to the switchyard. The number of ions directed from the switchyard to the cooler-buncher is measured using a Faraday cup. The number of ions is measured using this Faraday cup when the optics are optimally tuned and when they have been de-tuned. A scaling factor, K_{sf}, may be calculated by dividing the optimised ion current by the de-tuned ion current. It is assumed that the corresponding number of ions present in the laser-spectroscopy line during a resonance scan is equal to the number of ions detected by the MagneToF multiplied by the same scaling factor. If a resonance scan is performed using a different isotope to the one for which the beam currents had been measured using the switchyard Faraday cup, the scaling factor is modified further to account for the differences in isotopic abundance within the target material, e.g. if the alternative isotope is five times more abundant, it is assumed five times as many atoms are directed to the laser-spectroscopy line.

The efficiency of each transition is ranked in table 5.2. The 358 nm line is shown to be the most efficient in this series of experiments followed by the 425 nm line (the 358 nm line was determined to be approximately 2.8 times as efficient as the 425 nm line). The high efficiency of the 358 nm line makes it ideal for collecting large quantities of statistics in a limited period of time. The 425 nm line's high efficiency coupled with the fact that it produces a hyperfine spectrum highly appropriate for fitting models to also makes it a good candidate for use in the online campaign. Furthermore, the literature indicates that this transition has a suitable field shift factor for calculating the charge radii of the isotopes being studied [60]. The 358 nm and 425 nm lines share the same J_l state, therefore complementary measurements may be taken on the 358 nm line to rapidly obtain additional statistics to be used when modelling.

5.2 January 2021 Online Experimental Campaign

The purpose of this campaign was to make measurements of the hyperfine structures of the non-stable isotopes of chromium. The isotopes produced and measured include: ^{48}Cr, ^{49}Cr, ^{50}Cr, ^{51}Cr, ^{52}Cr, ^{53}Cr, and ^{54}Cr. Initially, measurements of the hyperfine spectra of $^{48-53}$Cr were made on the 358 nm line, and during the campaign, the transition being probed was changed to the 425 nm line. The reason for this is discussed in the previous section: the 425 nm line has a suitably high efficiency, produces a hyperfine spectrum that allowed for the extraction of hyperfine parameters, and as it was later determined has a field shift factor more suitable

for extracting the changes in mean-square charge radii from the measured isotope shifts than the 358 nm line. Measurements of $^{48-54}$Cr were made on the 425 nm line. Examples of the hyperfine spectra measured on each line are given in figures 5.2 and 5.3.

During the experiment, multiple measurements are taken for each isotope, and reference scans are made of the stable isotopes throughout the campaign, between the measurements of the isotopes of interest. When measuring on the 358 nm line ^{50}Cr and ^{52}Cr were used as the reference isotopes, whereas when measuring on the 425 nm line ^{50}Cr and ^{54}Cr were used as the reference isotopes. The reason for taking reference measurements is that during the experiment, systematic drifts may result in the spectra shifting slightly in frequency over the course of the experimental run. If reference scans were simply made at the start or the end of an experimental run, these drifts could impact the isotope shifts extracted. Regular reference measurements of the stable isotopes provide anchors from which the isotope shifts of the isotopes of interest can be calculated, therefore mitigating the potential for systematic drifts to impact the results.

Towards the end of this campaign, attempts were made to measure the hyperfine spectrum of ^{55}Cr. The target material was swapped to the ^{54}Cr enriched target to produce the isotope via a (d,p) stripping reaction, that is to say, the target is impinged by deuterons rather than protons allowing the neutron of a deuteron to be captured by a ^{54}Cr nucleus in the target, thus producing ^{55}Cr. Reference measurements were made using ^{54}Cr. Unfortunately, it was not possible to measure the hyperfine spectrum of ^{55}Cr. The measured spectra do not exhibit resonance peaks due to high relative background counts, this being in spite of efforts made during the experimental run to improve the quality of the measurements, such as optimizing the alignment of the laser to suppress background laser scatter, re-tuning the optics along the beamline, and taking steps to reduce the number of impurities present in the beam.

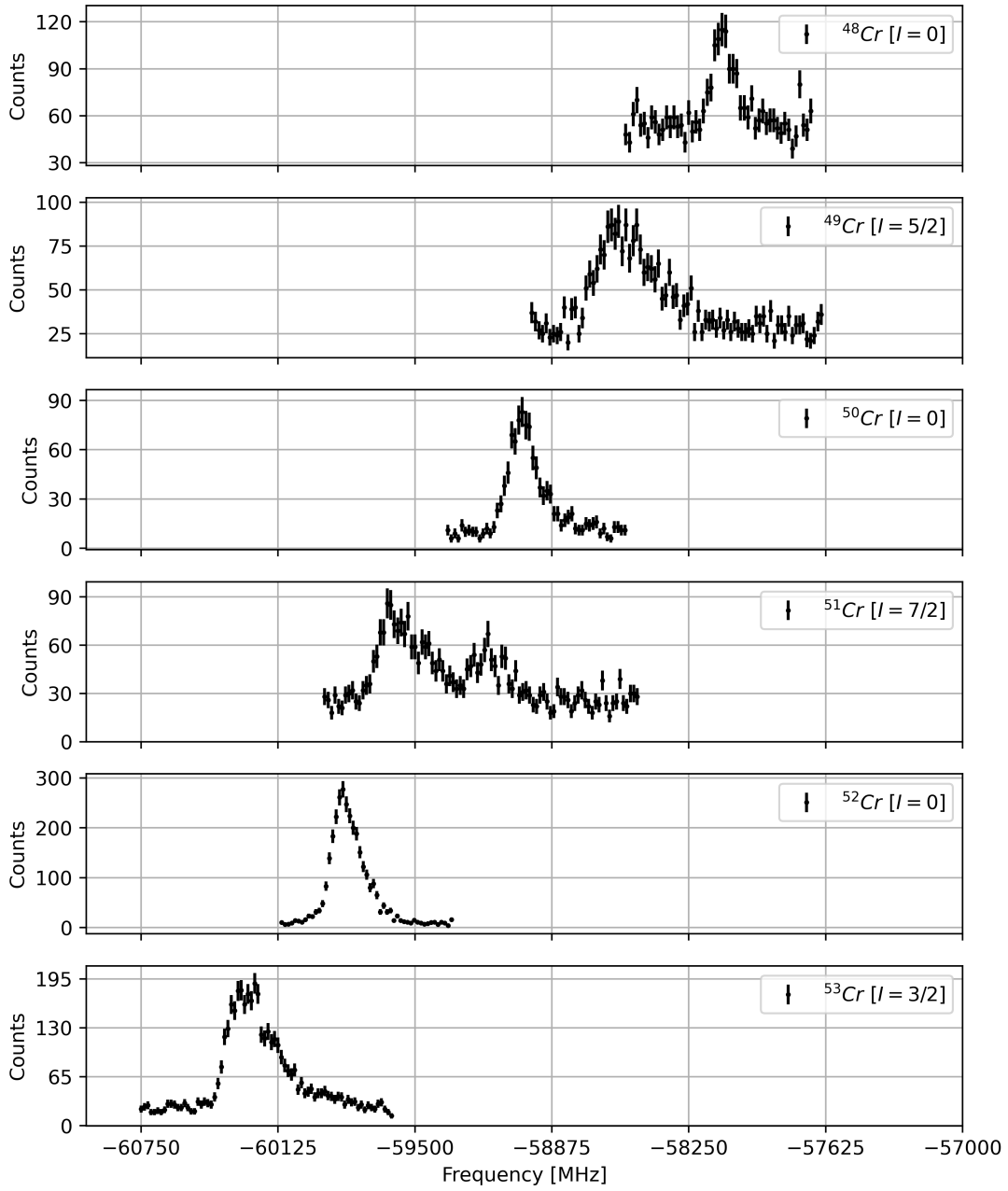

Figure 5.2: Plots to show examples of the hyperfine spectra obtained from each isotope of chromium when measured using the 358 nm transition.

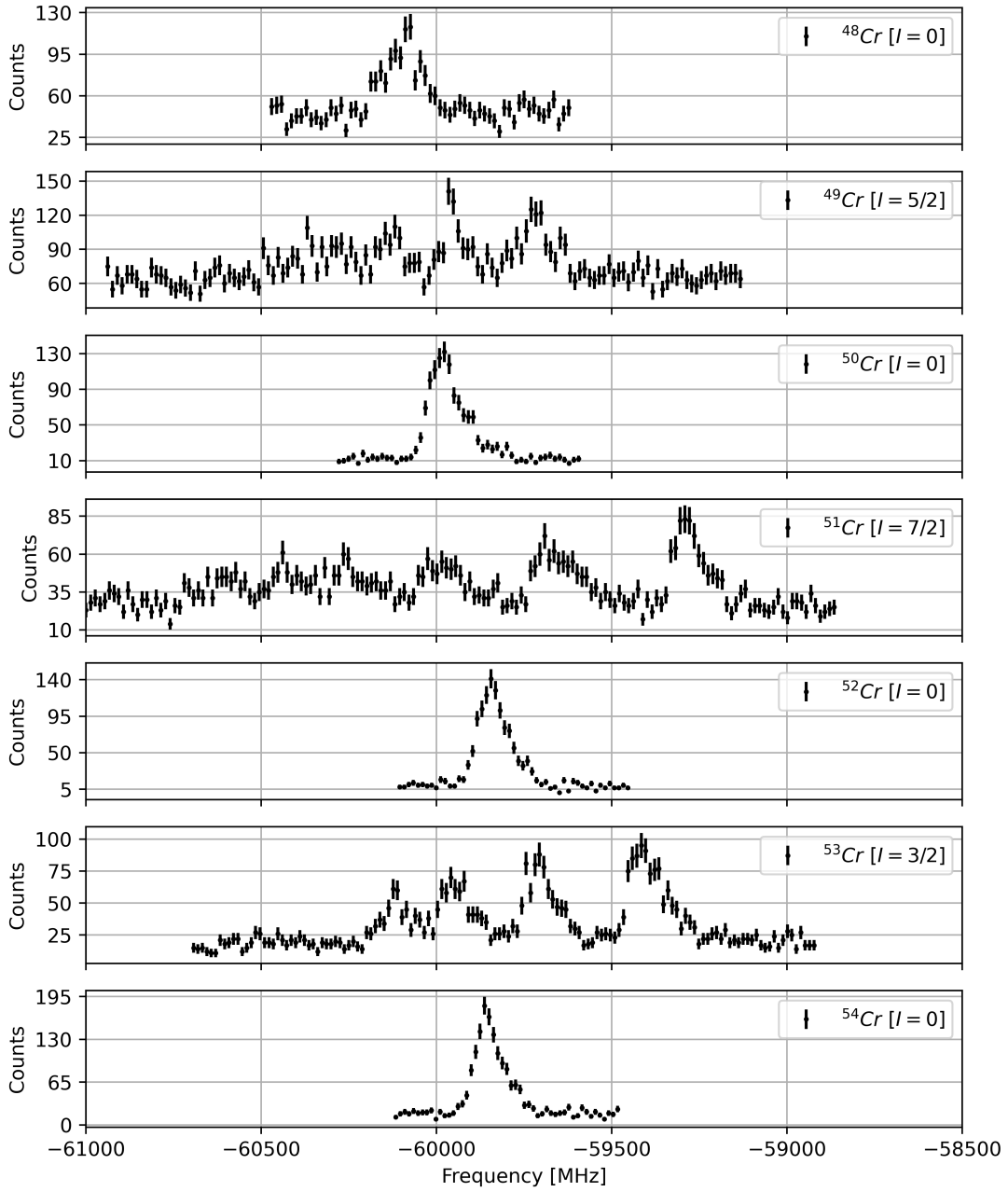

Figure 5.3: Plots to show examples of the hyperfine spectra obtained from each isotope of chromium when measured using the 425 nm transition.

The spectra obtained from this experimental campaign have features which make analysis difficult, for example, the peaks exhibit large asymmetries attributed to high-intensity satellite peaks (as can be seen in figures 5.2 and 5.3) and are generally poorly resolved. This made fitting models to the data very difficult. The hyperfine parameters and isotope shifts determined from preliminary analyses were heavily dependent on the properties of the model being used and were repeatedly inconsistent with the known literature values. For this reason, it was decided that additional offline measurements would be made of the stable isotopes of chromium. If

high-quality spectra were obtained in these remeasurements, it would be possible to use the results determined from the analysis of these spectra to constrain the models being fitted to the spectra obtained in the January 2021 campaign. It was hoped that this would simplify the modelling process and yield results that are consistent with the known literature values.

5.3 July 2021 Offline Experimental Campaign

The purpose of this campaign was to take additional measurements of the stable isotopes of chromium following the online campaign in January 2021. Measurements were made solely on the 425 nm line as by this point it had been established that the field shift factor for the 358 nm transition was not suitable for the extraction of charge radii from the isotope shifts (as will be outlined in the results section).

During the time that elapsed between the January 2021 and July 2021 campaigns, some minor improvements were made to the data acquisition system (DAQ) on the laser spectroscopy setup, which improved the quality of the hyperfine spectra that were recorded as can be seen in figure 5.4. The improvement in the quality of the measured spectra can be attributed to three things: the first is that the cooler-buncher voltage divider had been upgraded. The purpose of this component is to reduce the magnitude of the read-voltage of the cooler-buncher to one which can be handled by the inputs of the DAQ without overloading the circuitry. The second contribution is that a capacitor connected to the high-voltage platform and ground had been installed, this had the effect of smoothing out the platform voltage. The third factor was that the pressures and temperatures in the charge-exchange-cell appear to have been lower in the July 2021 campaign, as will be established in the subsequent satellite peak analysis. As a result of these contributions, the offline data allows for a much more precise determination of the A and B hyperfine parameters as well as the centroids of each spectrum.

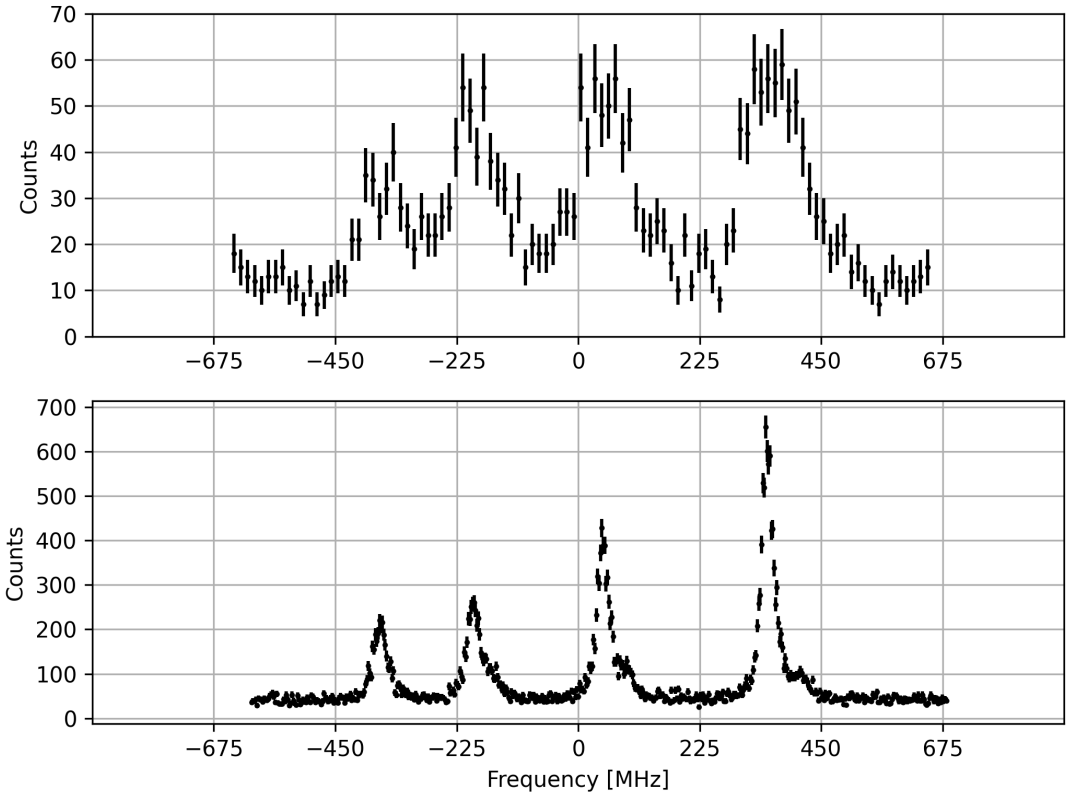

Figure 5.4: Plots to show the hyperfine spectra of ^{53}Cr measured on the 425 nm line in the January 2021 (top) and the July 2021 (bottom) experimental campaigns.

Chapter 6

Analysis Methods

6.1 Least-Squares Fitting

A model may be fitted to the data in order to extract properties from the spectra such as the level of background noise in the spectrum, the relative intensities of each peak in the spectrum, the full width at half maxima of each peak, the A and B hyperfine parameters, and the centroid of the spectrum.

There are multiple methods that may be employed when modelling a hyperfine spectrum, all similar but with minor amendments which may result in more accurate fitting results, for example, it may be appropriate to modify the complexity of the model used to fit the data; some atomic transitions produce hyperfine spectra with many unresolved and overlapping peaks, which if modelled to too high a complexity, due to there being too many competing fitting parameters, may result in the modelled parameters having exceedingly high associated errors. This in turn makes it difficult to draw strong conclusions from the data. In such instances, the models fitted the spectra may be simplified by using less mathematically complex line shapes e.g. Lorentzian rather than Voigt.

The fitting routines used in this analysis all operate on the premise of χ^2 minimisation, which is to say that the fitting parameters output by the fitting routine provide a model fit that best represents the trends of the data taking into account the magnitude of the associated error on each data point. The value of χ^2 is given by:

$$\chi^2 = \sum_{i=1}^{n} \left(\frac{x_i - \mu_i}{\sigma_i} \right)^2 , \tag{6.1.1}$$

where x_i is an observed experimental value, μ_i is an expected value derived from the model, and σ_i is the uncertainty associated with the observed experimental value, which is given by $\sqrt{x_i}$ as this experiment is a counting experiment and therefore observes Poisson statistics.

The χ^2 is divided by the number of degrees of freedom, which is calculated by subtracting the number of fitting parameters from the number of data points used in the fitting, to give the reduced χ^2. The reduced χ^2 is considered optimal when it has a value of 1, and it is the reduced χ^2 which is used to assess how likely the fit describes the data.

The χ^2 minimisation routine utilises a least squares fitting imported from the Python module "SciPy". The least squares fitting can be used for non-linear, multi-variable functions, such as the model used to describe a hyperfine spectrum. In this case, the least-squares fitting can be used to best determine the values of the model parameters for the peak FWHM, background statistics in the spectrum, hyperfine peak intensities, hyperfine A and B parameters, and the centroid of the spectrum through an iterative process used to minimise the distance between the model fit and experimental data points.

For example, the function used to model a particular hyperfine spectrum may be defined as:

$$y(x) = f(x, c_1, c_2, c_3, ..., c_n), \tag{6.1.2}$$

where y is the number of counts detected, x is the observed laser frequency, and the c terms represent the additional variables in the model such as the hyperfine parameters. This function would give y points:

$$y_1 = f(x_1, c_1, c_2, c_3, \ldots, c_n), \tag{6.1.3}$$

$$y_2 = f(x_2, c_1, c_2, c_3, \ldots, c_n), \tag{6.1.4}$$

$$y_3 = f(x_3, c_1, c_2, c_3, \ldots, c_n), \tag{6.1.5}$$

$$\vdots \tag{6.1.6}$$

$$y_n = f(x_n, c_1, c_2, c_3, \ldots, c_n). \tag{6.1.7}$$

Due to the limitations of the model function and other limitations which hinder the quality of the measured spectra, each experimental data point will differ somewhat from the value output by the model function for that particular x value. For a given data point this difference, the

residual, may be defined as:

$$R_i = y_i - f(x_i, c_{10}, c_{20}, c_{30}, ..., c_{n0}), \tag{6.1.8}$$

where c_{10}, c_{20}, etc. represent the values of the variables initially used. The residual value can then be minimised by using a Taylor series to determine how to optimise the values of the function variables [61]:

$$y_i = f(x_i, c_1, c_2, \ldots, c_n) = f(x_i, c_{10}, c_{20}, ..., c_{n0}) + \frac{\partial f}{\partial c_1} \cdot \Delta c_1 + \frac{\partial f}{\partial c_2} \cdot \Delta c_2 + \cdots + \frac{\partial f}{\partial c_n} \cdot \Delta c_n, \tag{6.1.9}$$

where Δc_n is a correction to the initial value used for a given variable:

$$c_n = c_{n0} + \Delta c_n. \tag{6.1.10}$$

Using equation 6.1.8, the function $f(x_i, c_{10}, c_{20}, ..., c_{n0})$ in equation 6.1.9 may be replaced with $y_i - R_i$, which gives the following when rearranged:

$$\frac{\partial f}{\partial c_1} \cdot \Delta c_1 + \frac{\partial f}{\partial c_2} \cdot \Delta c_2 + \cdots + \frac{\partial f}{\partial c_n} \cdot \Delta c_n = R_i. \tag{6.1.11}$$

The derivatives in equation 6.1.11 may be evaluated for each value of x, giving a system of linear equations:

$$\frac{\partial f(x_1)}{\partial c_1} \cdot \Delta c_1 + \frac{\partial f(x_1)}{\partial c_2} \cdot \Delta c_2 + \cdots + \frac{\partial f(x_1)}{\partial c_n} \cdot \Delta c_n = R_1, \tag{6.1.12}$$

$$\frac{\partial f(x_2)}{\partial c_1} \cdot \Delta c_1 + \frac{\partial f(x_2)}{\partial c_2} \cdot \Delta c_2 + \cdots + \frac{\partial f(x_2)}{\partial c_n} \cdot \Delta c_n = R_2, \tag{6.1.13}$$

$$\vdots \tag{6.1.14}$$

$$\frac{\partial f(x_3)}{\partial c_1} \cdot \Delta c_1 + \frac{\partial f(x_3)}{\partial c_2} \cdot \Delta c_2 + \cdots + \frac{\partial f(x_3)}{\partial c_n} \cdot \Delta c_n = R_m. \tag{6.1.15}$$

These linear equations may be solved in a matrix:

$$\begin{pmatrix} \frac{\partial f(x_1)}{\partial c_1} & \frac{\partial f(x_1)}{\partial c_2} & \frac{\partial f(x_1)}{\partial c_n} \\ \frac{\partial f(x_2)}{\partial c_1} & \frac{\partial f(x_2)}{\partial c_2} & \frac{\partial f(x_2)}{\partial c_n} \\ \vdots & \vdots & \vdots \\ \frac{\partial f(x_m)}{\partial c_1} & \frac{\partial f(x_m)}{\partial c_2} & \frac{\partial f(x_m)}{\partial c_n} \end{pmatrix} \begin{pmatrix} \Delta c_1 \\ \Delta c_2 \\ \vdots \\ \Delta c_m \end{pmatrix} = \begin{pmatrix} R_1 \\ R_2 \\ \vdots \\ R_m \end{pmatrix}$$

The expression above may be written in terms of the three matrices: the matrix of differentials, also known as the Jacobian matrix, J, the matrix of Δc values, ΔC, and the matrix of residuals, R:

$$J \cdot \Delta C = R. \tag{6.1.16}$$

In order to solve the equations to find the solutions of ΔC, J may be transformed so that it is square [62]:

$$(J^T J)\Delta C = J^T R, \tag{6.1.17}$$

$$\therefore \Delta C = (J^T J)^{-1} J^T R, \tag{6.1.18}$$

Once ΔC has been solved, the c values can be used to recalculate the residual values. This process is repeated for a significant number of iterations until the results begin to converge upon a solution (i.e. when the reduced χ^2 approaches a minimal value).

6.2 Data Processing

Prior to the models being fitted to the measured spectra, the raw data recorded must be organised and processed so that a suitable spectrum is produced. When processing the data it is possible to apply corrections to the data where necessary. This is discussed in more detail below.

6.2.1 Time-of-Flight Time Gating

When a bunch is released from the cooler it has a temporal width of approximately 10 μs, however, the period following the release of each bunch during which the data acquisition system records data for a given bunch is 200 μs. Although the rate of counts detected by the PMT will be the greatest during the window of time during which the bunch is passing directly in front of it, background counts, which may be attributed to scattered laser light, will also contribute to the recorded statistics across the whole 200 μs period. The effect these background statistics have in obscuring resonant photon counts in a spectrum can be significant, particularly when the resonant photon detection rate is comparable to the scattered photon detection rate, as may be the case if a particularly weak atomic transition or low yield isotope is being investigated.

The time-of-flight profile for a scan of ^{49}Cr is provided in figure 6.1. An optimised time gate can

be applied to this data set so that only the counts detected between 48 μs and 58 μs from cooler release (the peak) are included in the spectrum. The number of counts in this peak account for only 6.958% of the total number of counts in this data file. A comparison of the spectra produced when using the optimised time-gated data vs the non-optimised time-gated data (the 200 μs measurement period acts as a hardware imposed time-gate) is provided in figure 6.2. It can be seen that features indistinguishable in the non-time-gated spectrum become pronounced once optimised time-gating has been applied and the mass of background statistics eliminated. The number of background counts present in a spectrum may be reduced by up to four orders of magnitude using this method compared to using a continuous beam or no time gate being applied.

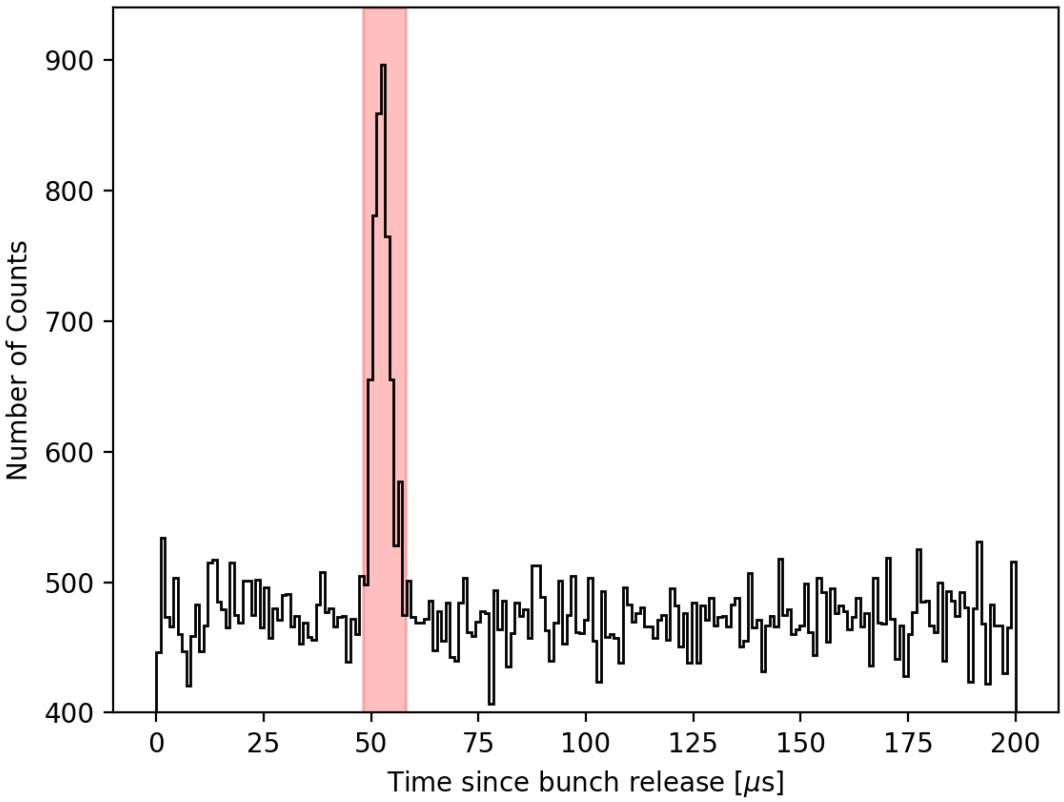

Figure 6.1: An example of a time-of-flight spectrum: the number of photons detected by the photo-multiplier tube as a function of the time elapsed since bunch release from the cooler. The time gate to be applied is highlighted in red.

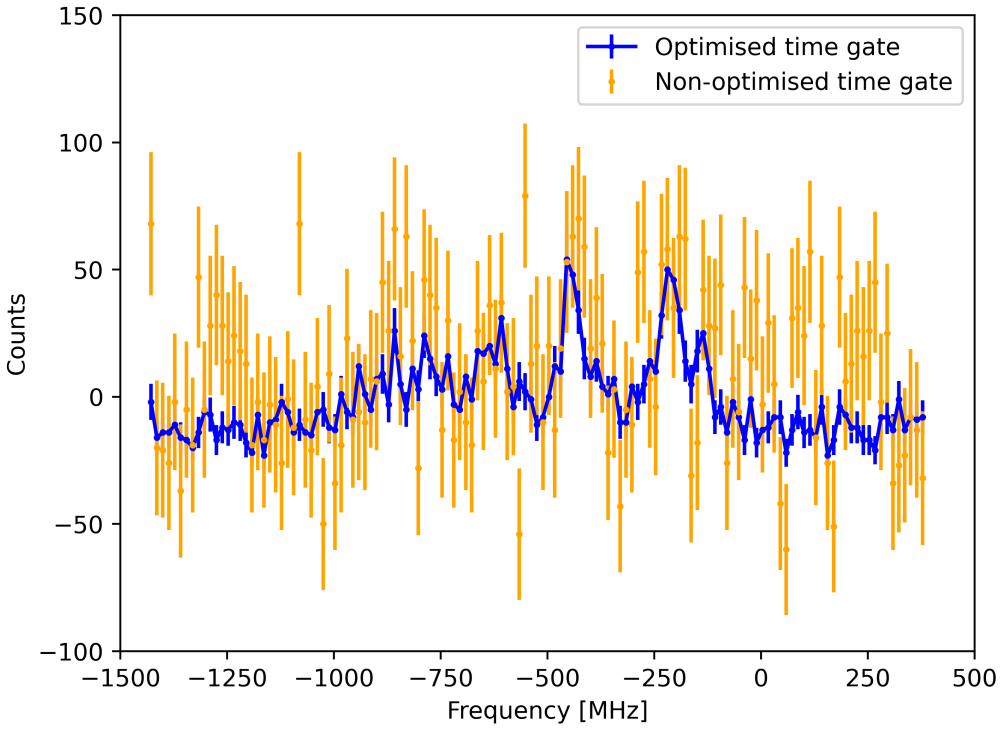

Figure 6.2: A plot for comparison of the spectra produced by the same run file when applying an optimised time gate vs the non-optimised time gate. For ease of comparison, each spectrum shown has had the background counts removed so that the features shown in each spectrum are offset to a similar value on the y-axis.

6.2.2 Voltage-to-Frequency Conversion

It is necessary to perform a voltage-to-frequency conversion. As discussed previously, the atoms are brought to resonance by Doppler tuning them using a tuning voltage, V_{tuning}, before they are neutralised in the CEC. As such, data may initially be presented as the number of counts detected by the PMT as a function of tuning voltage, however, to perform meaningful analysis this needs to be converted into the number of counts as a function of frequency. This is achieved using a Python script known as the "time gating and frequency conversion program", or "conversion program". The frequency of the laser in the reference frame of the atoms is related to the applied potential by the following:

$$v = v_l \left(1 + \alpha + \sqrt{2\alpha + \alpha^2}\right), \tag{6.2.1}$$

where,

$$\alpha = \frac{eV_{total}}{mc^2}, \tag{6.2.2}$$

v is the observed frequency, v_l is the frequency of the laser, $V_{total} = (V_{cooler} - V_{tuning})$, e is the charge of an electron, m is the mass of the atom, and c is the speed of light in a vacuum. The measured values of V_{tuning}, V_{cooler}, and v_l may have a correction applied in order to account for systematic effects in the data acquisition; this is discussed in more depth below.

6.2.3 Tuning Voltage Correction

The tuning voltage actually applied to the ions differs slightly from the tuning voltage programmed to be applied. To account for this discrepancy, for each experimental run a full sweep through the range of tuning voltages to be applied is made, and for each voltage increment the corresponding read-back of the tuning voltage through a voltage divider is saved within a file known as the "calibration file". A reading of the wavenumber of the laser for a given run is also recorded in this file to be used in the conversion calculation. A reading of the cooler voltage is also recorded in this file. The conversion program produces a plot of the measured tuning voltages as a function of the programmed tuning voltages and fits a line of best fit to the data. The values of tuning voltage used in the remainder of the conversion calculation are those provided by the line of best fit. An example of a tuning voltage calibration plot is shown in figure 6.3.

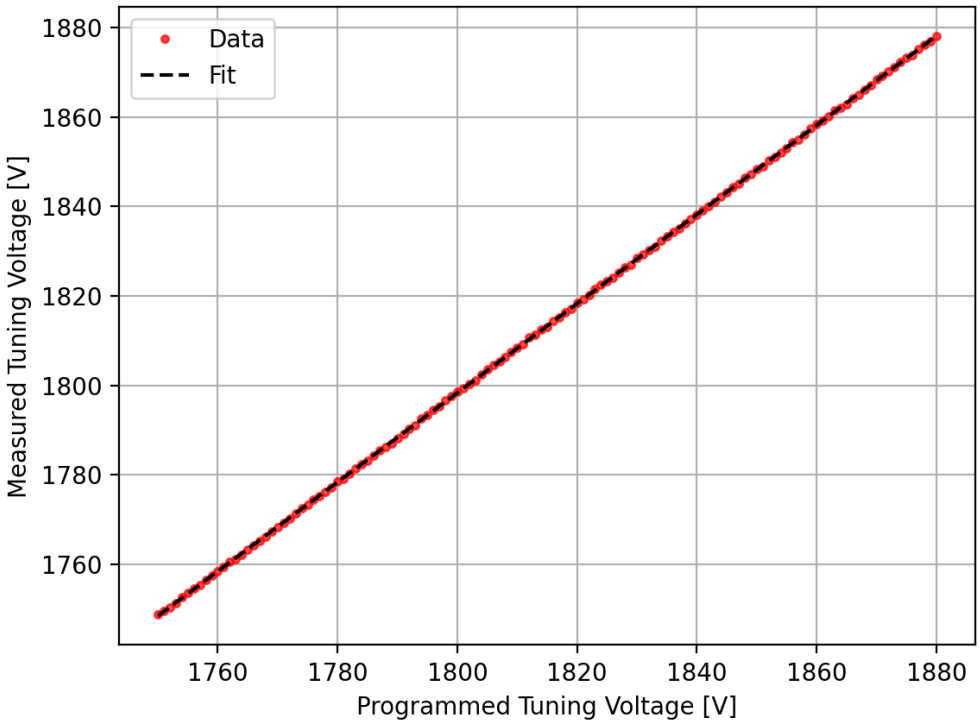

Figure 6.3: An example of a calibration plot from which the corrected tuning voltages may be determined for the voltage-to-frequency conversion calculation.

6.2.4 Cooler Voltage Correction

When extracting isotope shifts and hyperfine parameters from a spectrum, it is also important to ensure that the cooler voltage used in the frequency conversion calculation is appropriate. The voltage reading of the cooler-buncher varies throughout the duration of a scan and for this reason, a reading of the cooler voltage is recorded every time a photon is detected during a run; this is then saved within a file known as the "run file". The average of these recorded values is taken to be the cooler voltage to be used in the voltage-to-frequency conversion calculation. For each detection event, the following information is also recorded in the run file: the absolute time of the event, the programmed tuning voltage, the bunch number, and the time elapsed between the bunch being released from the cooler to the detection being made.

As an additional insurance, applying a small corrective offset to the cooler voltage may be necessary before frequency converting the data files. The magnitude of this offset can be determined by a simple calibration in which the hyperfine spectra of isotopes with very well-known hyperfine parameters are measured. For example, the hyperfine parameters of ^{171,173}Yb are known to a high degree of precision in the literature [63], therefore by measuring these spectra, extracting the hyperfine parameters determined for a range of corrective offsets, and then comparing them to the literature values, one can extrapolate what corrective offset should be applied to the cooler voltage to achieve the best agreement between the experimental and literature hyperfine parameters.

Measurements of the hyperfine spectra of ^{171,173}Yb ions were taken at the end of both the January 2021 and July 2021 experimental campaigns. The transition for which measurements were taken was $J_l = 4f^{14}6s^2S_{1/2} \rightarrow J_u = 4f^{14}6p^2P_{1/2}$, also known as the 369.419 nm line. The $4f^{14}6s^2S_{1/2}$ state is the ground state of ionic ytterbium, for which the A hyperfine parameters are well known. The value of the A hyperfine parameters were taken to be the same as the literature values used in the work of *de Groote* [63].

In this analysis, the Yb spectra were fitted simultaneously for each data set. The January 2021 data set contained 3 measurements of the ^{171}Yb spectrum and 4 measurements of the ^{173}Yb spectrum. The July 2021 data set contained 6 and 5 measurements of the ^{171}Yb and ^{173}Yb spectra, respectively. A consistent fitting procedure was adopted for both the January 2021 and July 2021 measurements; for each data set Lorentzian line shapes and Racah intensities were used to model the resonance peaks, all of the available run files were fitted simultaneously

with the A_l hyperfine parameters being modelled as a single fitting parameter for each isotope, and the $A_u : A_l$ ratio being modelled as a single fitting parameter for all of the run files of each isotope. Additional fitting parameters used when modelling satellite peaks did not need to be considered in the fitting procedure as ionic species of Yb were used, meaning they did not undergo charge exchange, which otherwise could have resulted in satellite peaks being present in the spectra.

Figure 6.4 shows the difference between the experimental and literature values of the A hyperfine parameters of the ground states of ^{171,173}Yb for the January 2021 and July 2021 data sets. The weighted mean of the x-axis intercepts of the two lines of best fit was taken to be the correct cooler voltage correction.

The weighted mean, $\bar{x}$, of n variables, x_i, with associated errors, σ_i, is calculated using the following equation:

$$\overline{x} = \frac{\sum_{i=1}^{n} (w_i \cdot x_i)}{\sum_{i=1}^{n} w_i}, \tag{6.2.3}$$

where w_i is a weighting factor calculated as:

$$w_i = \frac{1}{{\sigma_i}^2}, \tag{6.2.4}$$

where σ_i is the error associated with x_i. The standard error of the weighted mean is given by:

$$\sigma_{\overline{x}} = \sqrt{\frac{1}{\sum_{i=1}^{n} w_i}}. \tag{6.2.5}$$

The intercepts of the lines of best fit with $y = 0$ for the ^{171}Yb and ^{173}Yb data were inconsistent with one another in both the January 2021 and July 2021 data. For this reason, the standard error of the weighted average was inflated using the Birge ratio, σ_B, defined as [64]:

$$\sigma_B = \sqrt{\frac{1}{n-1} \sum \frac{(x_i - \bar{x})^2}{\sigma_i^2}}. \tag{6.2.6}$$

The cooler voltage corrections were taken to be (37 ± 5) V and (-21 ± 5) V for the January 2021 data and July 2021 data, respectively. The large difference in cooler voltage corrections is unsurprising as different voltage dividers were used in each campaign.

It is noteworthy and unexpected that in both analyses the cooler-voltage corrections determined using ^{171}Yb and ^{173}Yb were inconsistent with one another. This suggests that an additional

calibration must be performed. As the only other variable used in the voltage-to-frequency conversion is the wavenumber of the laser, a similar calibration was performed to determine the corrective offset that needed to be applied to the recorded value of the wavenumber in each calibration file.

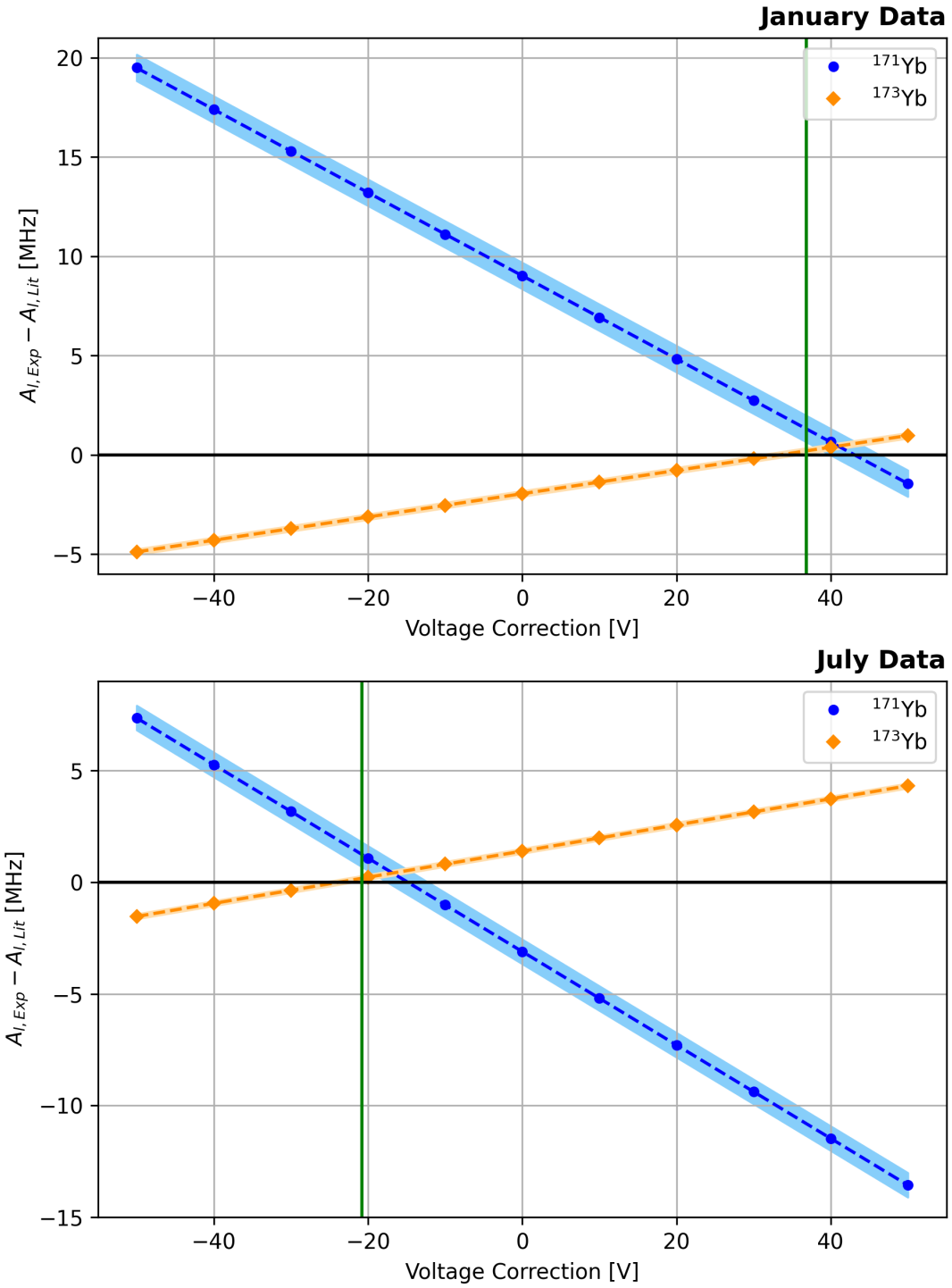

Figure 6.4: A plot of the discrepancy between experimental A hyperfine parameters measured in January 2021 (top), and July 2021 (bottom), with literature A hyperfine parameters, as a function of cooler voltage correction for ^{171,173}Yb. The coloured bands represent the combined statistical uncertainties for the data points. January 2021: the weighted average of the x-axis intercepts gives a cooler voltage correction of (37 ± 2) V, with a Birge inflated error of 5 V. July 2021: the weighted average of the x-axis intercepts gives a cooler voltage correction of (-21 ± 2) V, with a Birge inflated error of 5 V.

6.2.5 Laser Wavenumber Correction

In order to determine the corrective offset that needs to be applied to the wavenumber used in the conversion calculation, the cooler voltage corrections determined previously are applied in the conversion program, and similarly to the previous stage of the analysis, the differences between the literature and experimental hyperfine parameters are determined for ^{171}Yb and ^{173}Yb for a range of wavenumber corrections. However, unlike the previous stage of the analysis, the discrepancy between these 'experimental-literature difference' values for the two isotopes is taken and plotted as a function of the wavenumber correction. This data is then fitted linearly to determine the wavenumber correction to be applied in the conversion calculation. The $y = 0$ intercept of the plot described gives the wavenumber correction that results in the lines of best fit from figure 6.4 converging at the previously determined cooler voltage corrections. Figure 6.5 shows the plots used to determine the appropriate wavenumber corrections for the January 2021 and July 2021 data sets.

By repeating the analysis performed to determine the required cooler voltage correction, but having applied the appropriate wavenumber corrections for the January 2021 and July 2021 data, it can be seen in figure 6.6 that the lines of best fit for ^{171}Yb and ^{173}Yb now converge at the weighted average cooler voltage corrections determined previously, thus confirming that the wavenumber corrections calculated are appropriate. It is noted that this approach does result in a very small discrepancy between the point of intersection of the fitted lines and the $y = 0$ line, however the analysis required to eliminate this discrepancy would be much more challenging and time consuming and was deemed unjustifiable considering that the difference in results would be insignificant.

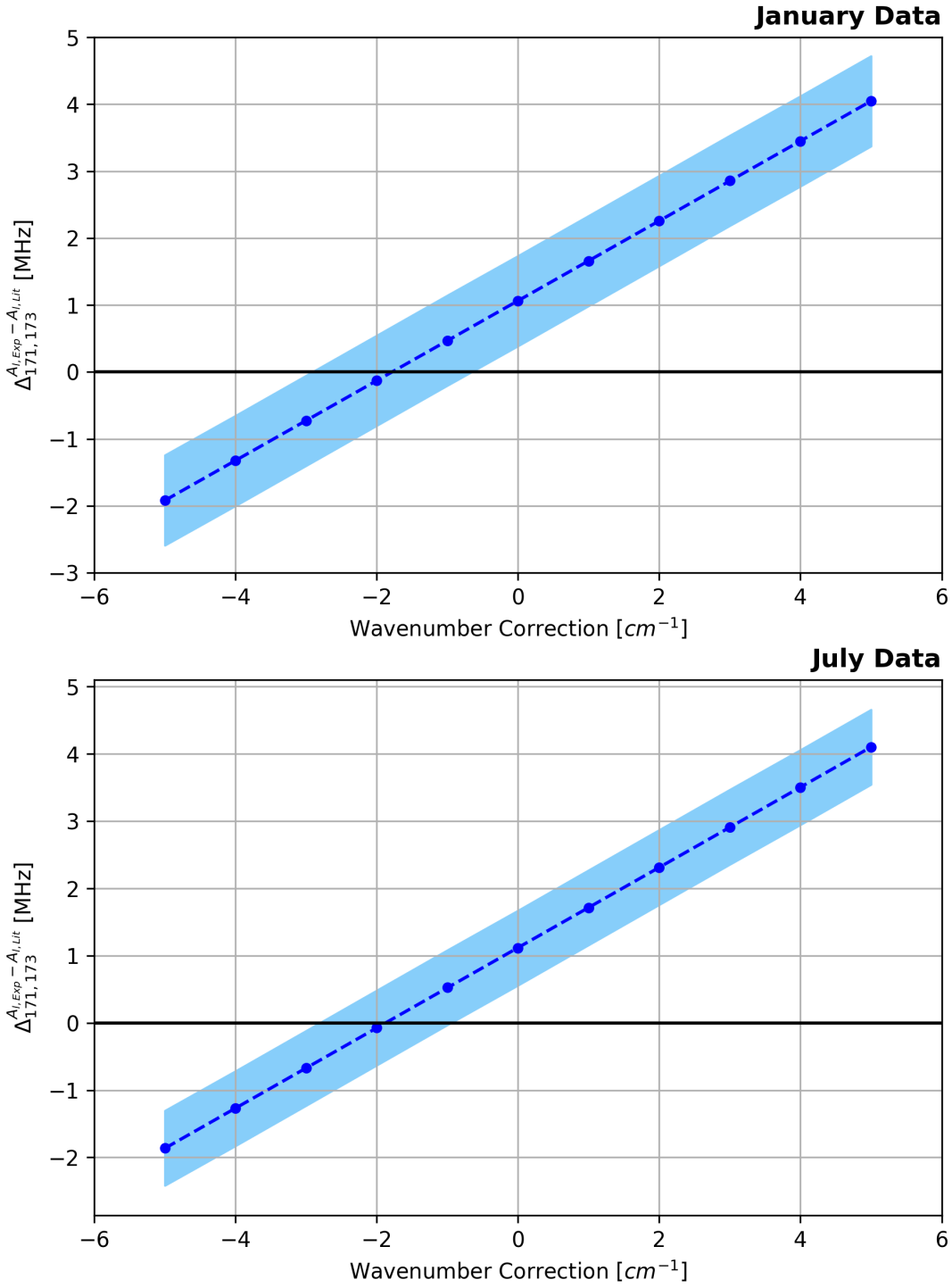

Figure 6.5: A plot to show the discrepancy between the 'experimental-literature difference' values for ^{171}Yb and ^{173}Yb as a function of wavenumber correction for the January 2021 (top) and July 2021 (bottom) data sets. The appropriate wavenumber correction as determined from the $y = 0$ intercept of the line of best fit is $(-2 \pm 1)\,\mathrm{cm}^{-1}$ for the January 2021 data, and $(-1.9 \pm 0.9)\,\mathrm{cm}^{-1}$ for the July data.

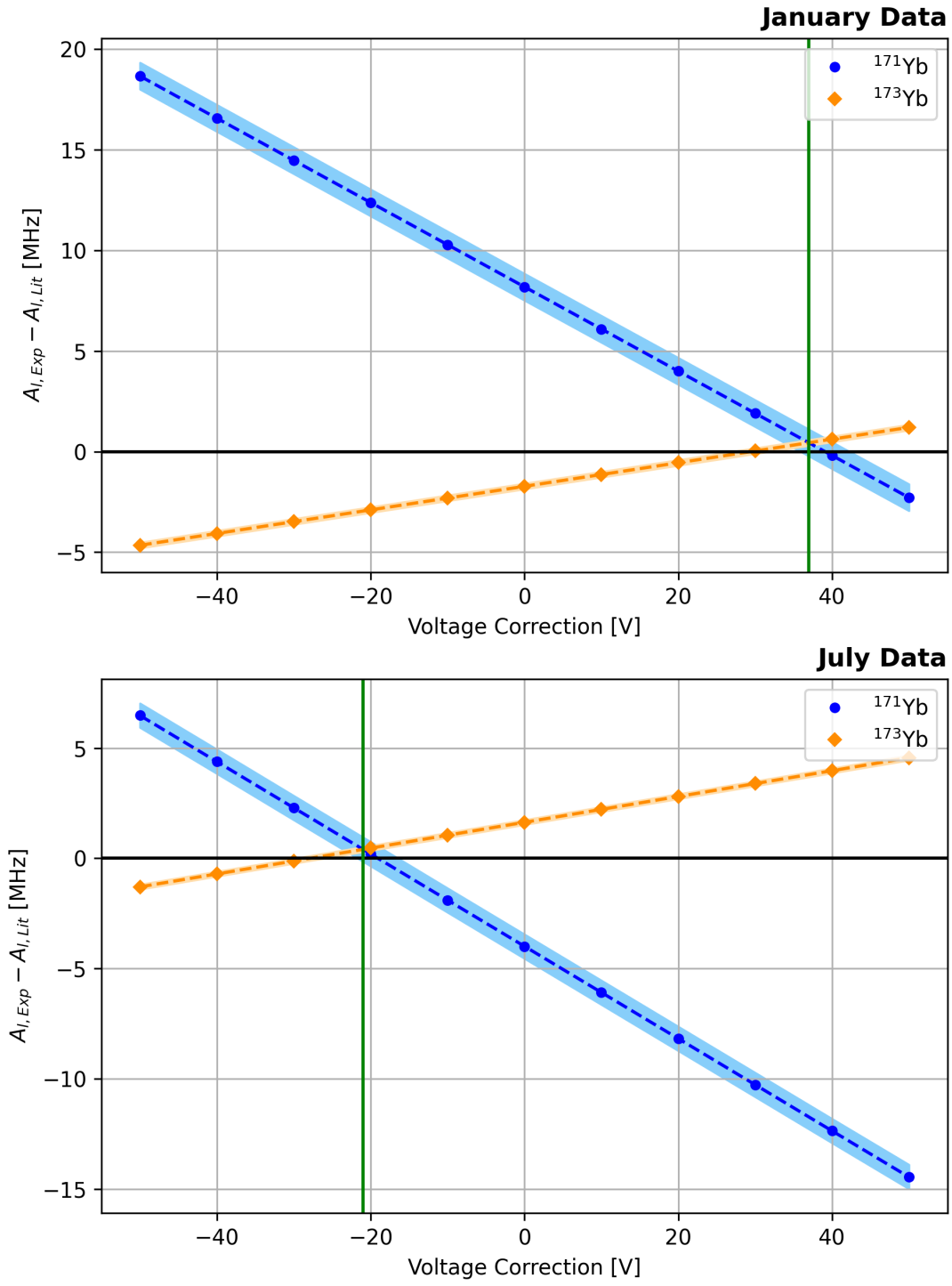

Figure 6.6: A plot of the discrepancy between experimental A hyperfine parameters measured in January 2021 (top), July 2021 (bottom), and literature A hyperfine parameters as a function cooler voltage correction for ^{171,173}Yb, when an appropriate correction has been applied to the wave numbers recorded in the calibration files. The coloured bands represent the combined statistical uncertainties for the data points, the green line indicates the cooler voltage correction to be applied in the frequency conversion calculation for the January 2021 data set.

6.3 Satellite Peak Analysis

As discussed previously, satellite peaks in the spectrum correspond to electrons being promoted to excited states in the atom. Therefore, the energy offset of a satellite peak relative to its parent resonance peak must be equal to the difference in energy between the excited state and the ground state. Whilst the energy offset between a satellite peak and its parent peak is isotope independent, the frequency offset differs for each isotope being investigated. This is because the voltage-to-frequency conversion factor, a value directly proportional to the energy-to-frequency conversion factor, is also isotope dependent.

In order to determine the properties of satellite peaks present in the spectra obtained in January 2021 and July 2021, various analysis methods were performed. When modelling a series of satellite peaks, the model should include a sufficient number of satellite peaks to be realistic, but not so many that the model becomes too computationally complex for efficient analysis. The number of satellite peaks modelled per resonance peak was set to 3.

In order to simplify the analysis to the greatest extent possible, only the spectra obtained from even-N, stable isotopes of chromium were used. This is due to the fact that these spectra have sufficient statistics for meaningful analysis, and as a consequence of the lack of a nuclear spin, these isotopes do not exhibit a hyperfine splitting - only a single peak corresponding to the fine structure transition. The hyperfine spectra produced by the odd-N isotopes contain unresolved hyperfine peaks when measured on both the 358 nm and 425 nm lines; this is difficult to model, even when not accounting for additional unresolved satellite peaks, therefore these spectra were not used for determining the properties of any potential satellite peaks.

Initially, the analysis was performed on the data obtained from the July 2021 experimental campaign. This was due to the fact that, as mentioned previously, hyperfine spectra obtained from this campaign were better resolved than those obtained in the January 2021 campaign. For each isotope, the analysis methods used were the following:

1. The spectra were fitted with a skewed Lorentzian function, assuming the presence of 1, 2, or 3 series of satellite peaks present in the spectra, with each series having a unique energy offset;
    (a) wherein the peak full-width-half-maxima (FWHM) and Poisson factors were fitting parameters unique to each run file;

(b) wherein the FWHM was a fitting parameter shared between all of the run files, and the Poisson factors were unique for each run file;

(c) wherein the FWHM and the Poisson factor were fitting parameters shared between all of the run files.

2. The spectra were fitted with a skewed Lorentzian, wherein the satellite peak offsets were fixed to frequencies that corresponded to known, strong ground state transitions. This method was repeated under two different conditions:

   (a) wherein the Poisson factor is a unique fitting parameter for each run file and for each transition;

   (b) wherein the Poisson factor is a shared fitting parameter across all run files for each transition.

As the data obtained in the July 2021 campaign was obtained using an offline source of ions, therefore guaranteeing a high ion delivery rate to the laser spectroscopy station, it was possible to take all of the measurements in this data set over a short period of time. The conditions within the charge-exchange-cell were unlikely to fluctuate significantly over the period that measurements were taken. For this reason, it is permissible to fit the data where the FWHM and Poisson fitting parameters are shared across each run file as was done in methods 1(b) and 1(c).

In order to conclusively identify which atomic transition(s) contributed to peak asymmetry in the data sets when using method 1, the following criterion needed to be met: the analysis must produce a satellite peak energy offset which is consistent across each isotope analysed, and with a known ground state transition. The results were deemed to be consistent if the three sigma consistency condition was met:

$$|x_1 - x_2| < 3\sqrt{\delta x_1^2 + \delta x_2^2}, \tag{6.3.1}$$

where x_i is one value and δx_i is its associated uncertainty. When multiple series of satellite peaks were modelled, the magnitudes of the energy offsets were used when comparing the offsets determined using each isotope e.g. the smallest offset determined using ^{50}Cr was compared to the smallest determined using ^{52}Cr and ^{54}Cr etc.

The second analysis method was based on the assumption that the relative intensities of the satellite peaks for each transition, measured by their Poisson factors, correlate to the likelihood

that the transition is the root of any peak asymmetries. For this analysis, nine different ground state transitions were considered as potential roots of the observed asymmetries owing to their high transition strengths (A-values greater than or equal to $10^7\,s^{-1}$). Table 6.1 outlines the properties of each of these transitions. The strength of a transition correlates to the lifetime of its excited state, for example, on average an electron will relax from an excited state and back to the ground state more quickly for a higher-strength transition than for a lower-strength transition. It is therefore more likely that the electron is in the ground state prior to interacting with the laser and achieving resonance for a higher-strength transition, thus making them more likely candidates as the root of any peak asymmetries.

The candidate transitions used in this analysis were grouped into series as indicated in table 6.1. This is because the difference in the frequency offsets corresponding to each transition within a series was less than 0.5 MHz for a given isotope. Accordingly, the frequency offset corresponding to the average energy of the transitions within each series was used in this analysis. These groupings of transitions will henceforth be referred to as the 194 nm series, 359 nm series, and 427 nm series.

Series Name	Wavelength (nm)	Photon Energy (eV)	Lower State (cm^{-1})	Upper State (cm^{-1})	Transition Strength ($10^7\ s^{-1}$)
194 nm	194.0451	6.389515	0	51534.400	1.718
	194.0561	6.389156	0	51531.500	1.719
	194.0640	6.388895	0	51529.400	1.719
359 nm	357.8686	3.463563	0	27935.242	14.83
	359.3485	3.449299	0	27820.198	14.95
	360.5329	3.437969	0	27728.812	16.14
427 nm	425.4336	2.913511	0	23498.817	3.148
	427.4797	2.899566	0	23386.343	3.062
	428.9717	2.889481	0	23305.005	3.155

Table 6.1: A table to show the properties of the candidate ground state transitions used in the satellite peak analysis. All values taken from Kurucz spectral line database [38].

6.3.1 July 2021 Satellite Peak Analysis Results

The satellite peak offsets determined from analysis methods 1(a), 1(b), and 1(c) are shown in figure 6.7. Only method 1(c), assuming the presence of 3 unique sets of satellite peaks, produced satellite peak offset energies that were consistent for each isotope according to equation 6.3.1. However, each of these offset energies were very small and did not correspond to any

of the ground state transitions found in atomic chromium. For this reason, these offsets were deemed unsuitable for use in the remainder of the analysis.

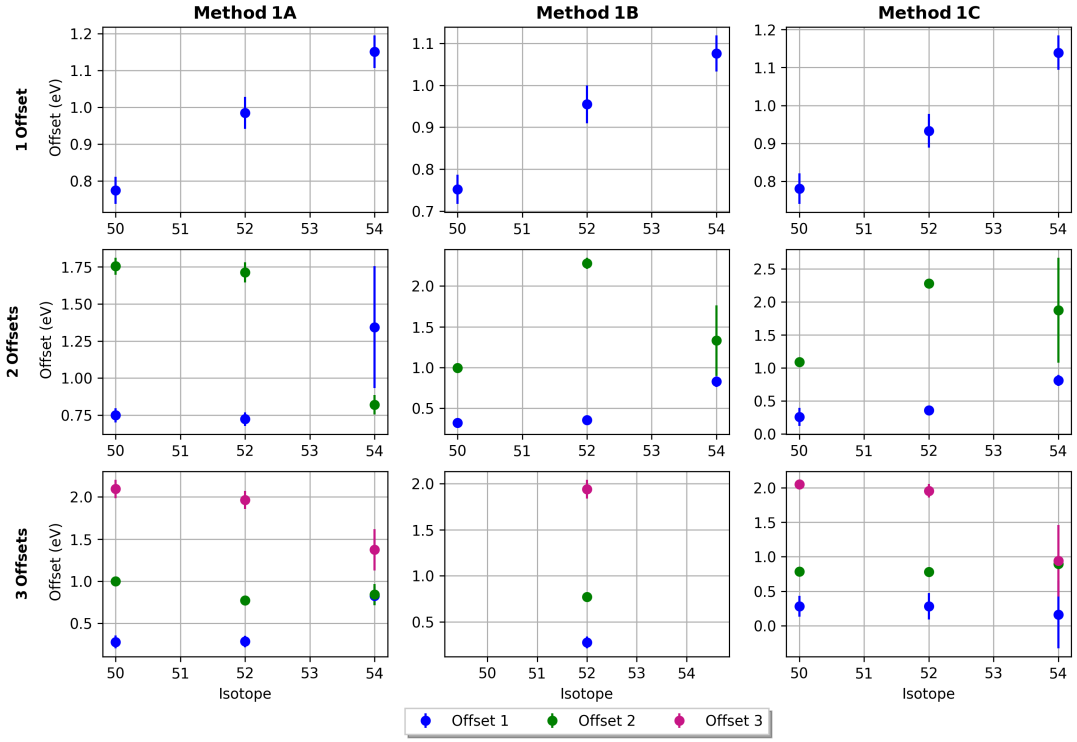

Figure 6.7: A plot to show the satellite peak offset energies determined from analysis methods 1(a), 1(b), and 1(c) using the data collected in July 2021. Note: It was only possible to extract offset energies for ^{52}Cr using method 1(b) assuming 3 unique satellite peak offsets; the fitting script was unable to optimise models for ^{50}Cr and ^{54}Cr.

Figure 6.8 shows the Poisson factors determined for each transition in analysis 2(a). The results show that the 427 nm series of transitions dominates in each instance, however, the large error bars overlap with those of the other transitions which have smaller Poisson factors. In either case, the 359 nm series of transitions has a Poisson factor that is largely consistent with 0, therefore this transition may be disregarded.

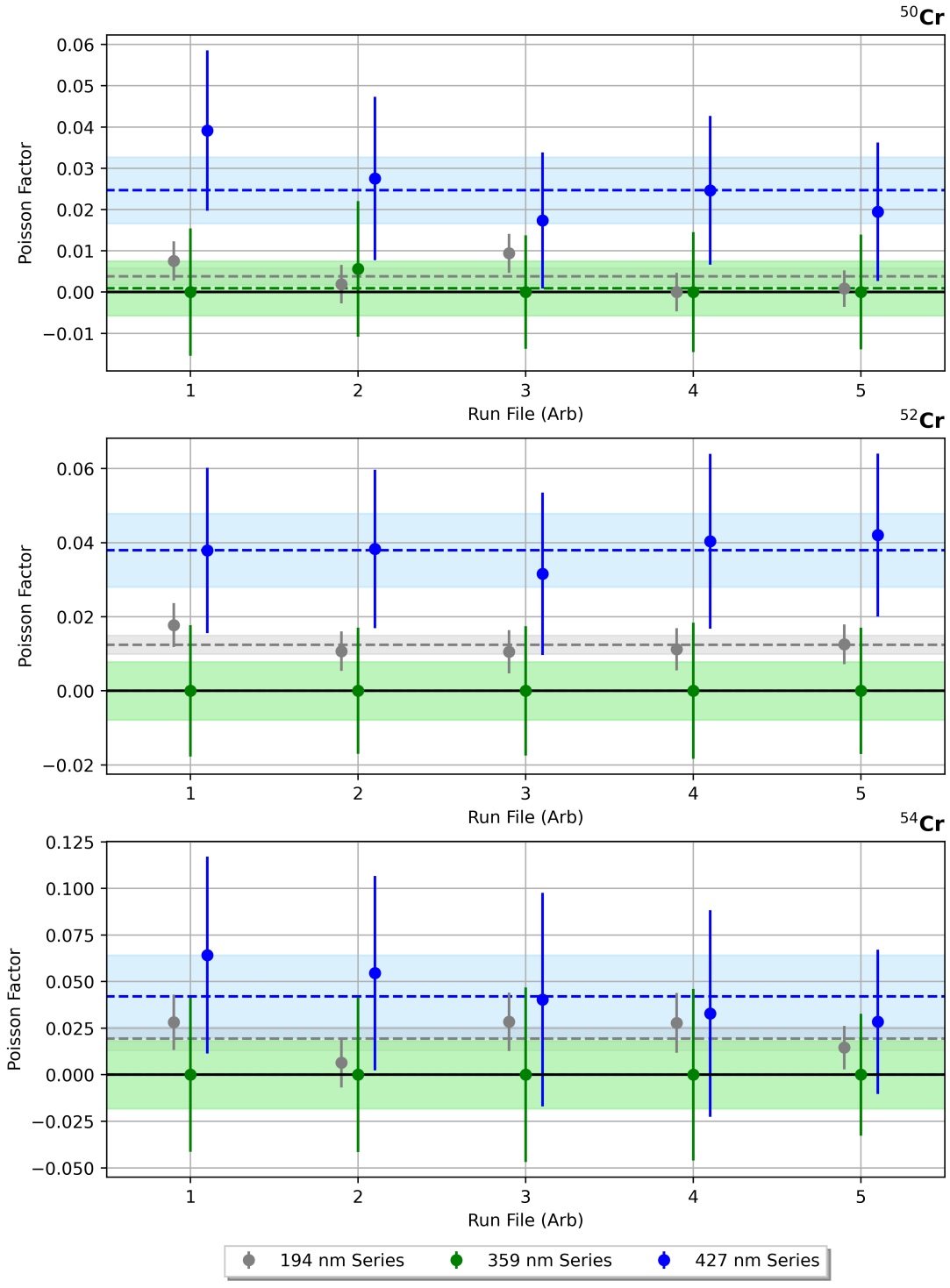

Figure 6.8: A plot to show the Poisson factors determined for each transition as a function of isotope using analysis method 2(a) and the July 2021 data set. The dashed lines and coloured bands represent the weighted averages and their associated errors, respectively. The run files for each isotope have been assigned an arbitrary value to aid presentation. The assigned value reflects the order in which the measurements were taken.

Figure 6.9 shows the Poisson factors determined for each transition in analysis 2(b). These

show a similar trend in that the 427 nm series of transitions dominate, followed by the 194 nm and then 359 nm series of transitions, which again give Poisson factors consistent with 0. From this set of results, it again appears that the 427 nm series of transitions is the most likely to contribute to the peak asymmetry in the spectra. It is noted that the Poisson factors determined for each transition series should be isotope independent, therefore the lack of consistency between the Poisson factors determined for the 194 nm series is noteworthy.

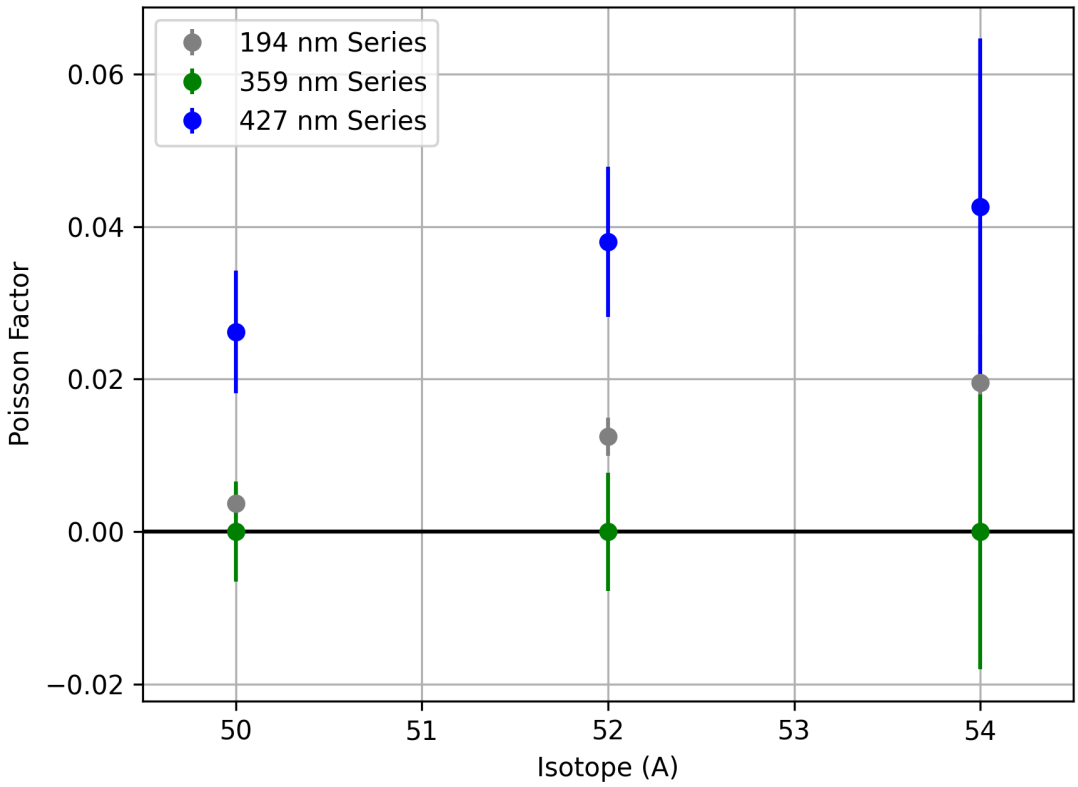

Figure 6.9: A plot to show the Poisson factors determined for each transition as a function of isotope using analysis method 2(b) and the July 2021 data set.

The results from the satellite peak analysis of the July 2021 data show that there is little asymmetry in the peaks of the spectra, this is evidenced by the fact that when the energy offsets are free to assign themselves to their optimal value, they consistently have energies much smaller than the smallest energy ground state transition, this occurs even when the energy offsets across isotopes are consistent with one another. Furthermore, the Poisson factors determined in analysis methods 2(a) and 2(b) are very small, which is indicative of little peak asymmetry. For this reason, a similar analysis was performed on the January 2021 data collected during the online experimental campaign; this data set exhibits significant asymmetry.

6.3.2 January 2021 Satellite Peak Analysis Results

The measurements made in the January 2021 campaign were taken over a series of days, over which the conditions in the charge-exchange-cell may have fluctuated. For this reason, it is not appropriate to perform analysis methods 1(b) or 1(c) on this data set.

The satellite peak offsets determined from analysis method 1(a) are shown in figure 6.10. It can be seen that regardless of whether 1, 2, or 3 unique satellite peaks are fitted there is(are) no consistent energy offset(s) output by the fitting routines across all isotopes. Therefore the conclusion drawn is that none of these offsets are appropriate to be used in further analysis.

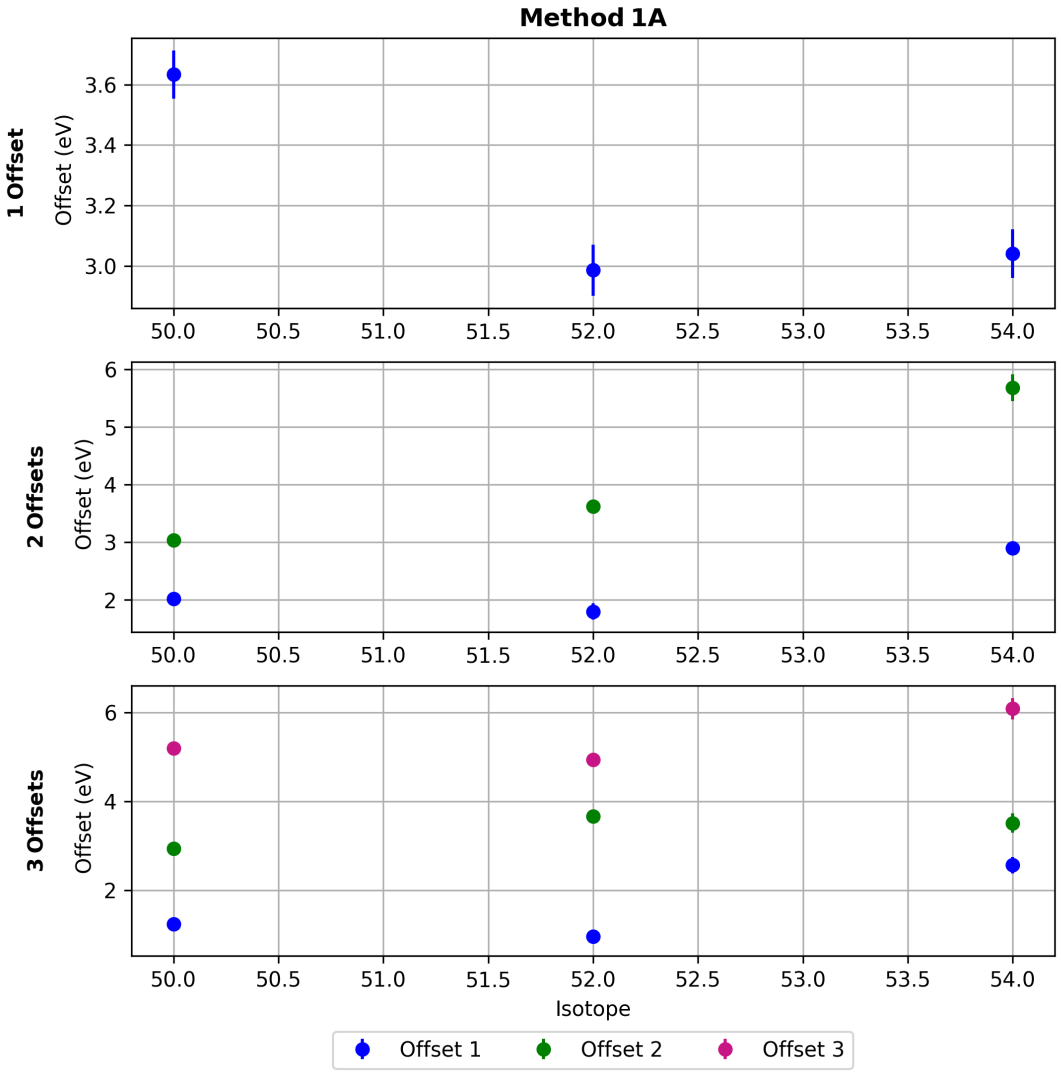

Figure 6.10: A plot to show the satellite peak offset energies determined from analysis method 1(a) using the data collected in January 2021.

Figure 6.11 shows the results of analysis method 2(a). It can be seen that the weighted average

of the Poisson factors is generally largest for the 359 nm series of transitions (the exception being for ^{52}Cr), but that this is generally closely followed by that of the 427 nm series of transitions. In all instances, the contribution of the 194 nm transitions is the smallest. There are however large uncertainties associated with each of the data points, which make interpreting the results more difficult. For this reason, the results of method 2(b) should be considered. As the measurements made in this campaign were taken over an extended period of time, during which the conditions within the CEC are likely to have fluctuated, it could be argued that it is not appropriate to fit the data using shared fitting parameters for the Poisson factor, however, due to the large error bars associated with the sporadic data points obtained from analysis method 2(a), it is argued that a more flexible approach to determining which series of transitions is the root of the peak asymmetry should be considered.

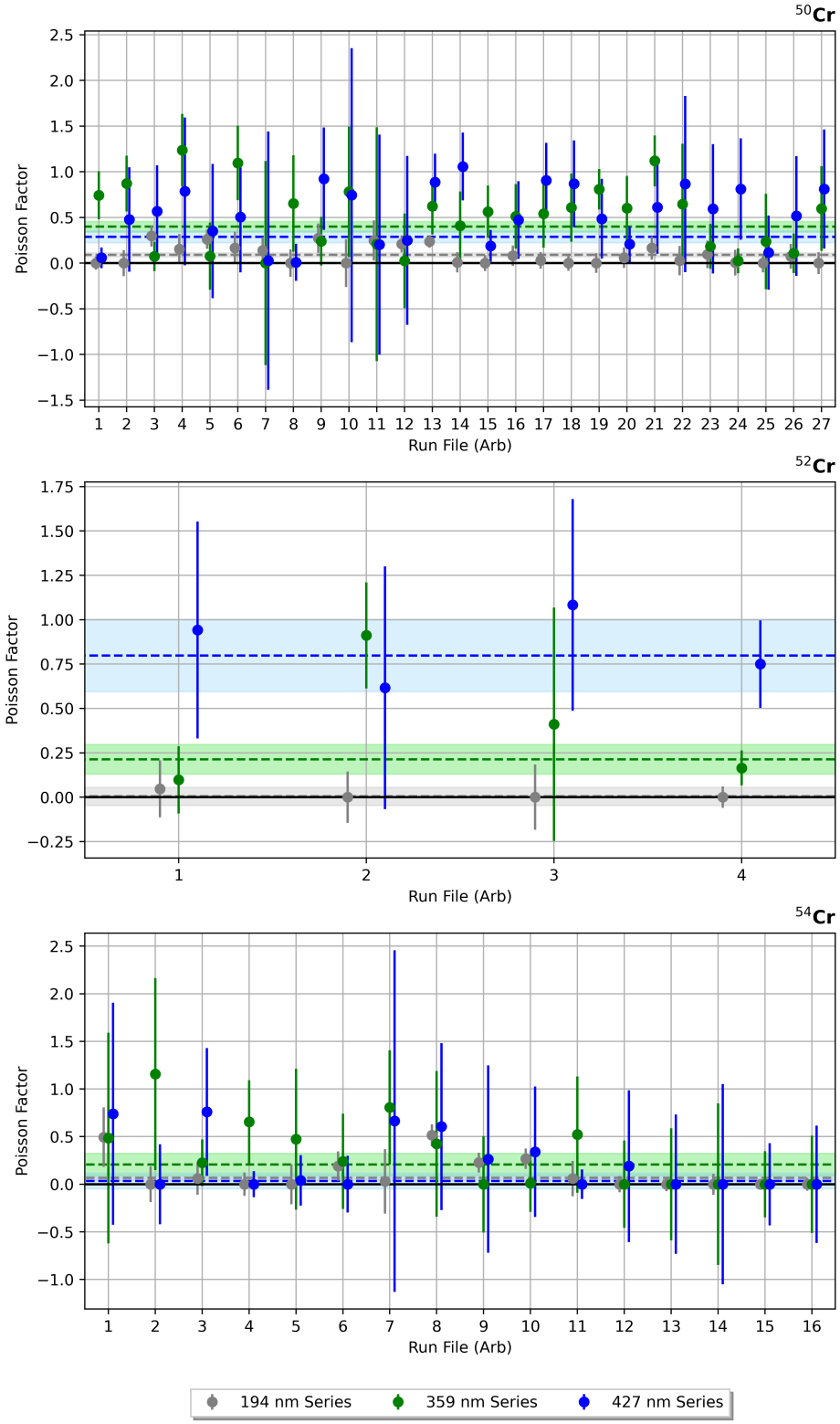

Figure 6.11: A plot to show the Poisson factors determined for each transition as a function of isotope using analysis method 2(a) and the January 2021 data set. The dashed lines and coloured bands represent the weighted averages and their associated errors, respectively. for each series The run files for each isotope have been assigned an arbitrary value to aid presentation. The assigned value reflects the order in which the measurements were taken.

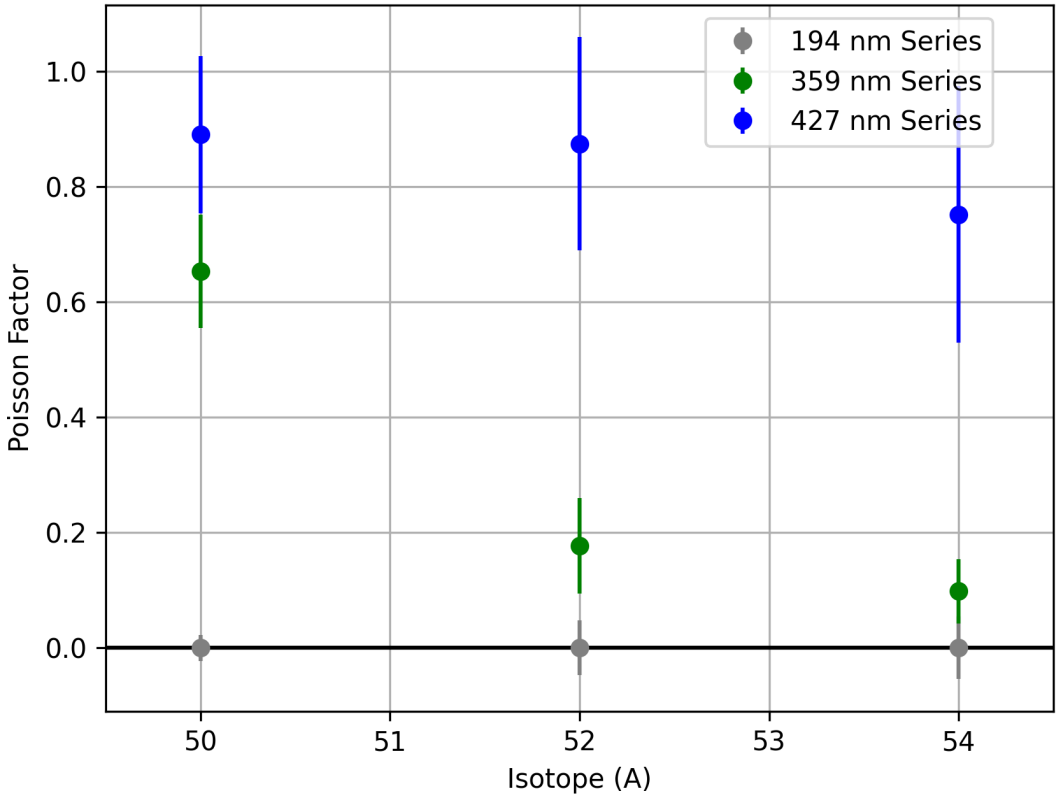

Figure 6.12: A plot to show the Poisson factors determined for each transition as a function of isotope using analysis method 2(b) and the January 2021 data set.

As can be seen from figure 6.12, it is apparent that the energy offset of the 427 nm series of transitions dominates, followed by the 359 nm series of transitions, and then the 194 nm series of transitions. This result is in agreement with the parallel analysis performed on the data obtained in July 2021. The high Poisson factor determined for the 359 nm series when analysing the ^{50}Cr spectra is anomalous as, as mentioned previously, this value should be independent of the isotope being investigated.

In summary, analysis methods have been performed to determine the energy offsets of any satellite peaks that may be present in the spectra. The analysis shows that the spectra obtained in July 2021 do not exhibit significant peak asymmetries. That being said, according to analysis methods 2(a) and 2(b), if any satellite peaks were to be modelled in these spectra, the energy offset corresponding to the 427 nm series of transitions should be used. The January 2021 data set does exhibit significant peak asymmetry, and it is not as apparent as to which energy offset these underlying satellite peaks should adopt for further analysis; analysis method 2(a) suggests that the energy offset corresponding to the 359 nm or 427 nm series of transitions could be used, whereas analysis 2(b) suggests that offset corresponding to the 427 nm series of

transitions should be used. Taking into consideration both the January 2021 and July 2021 data sets, this analysis would suggest that the energy offset corresponding to the 427 nm series of transitions should be used as the appropriate satellite peak energy offset in subsequent analysis.

6.4 Extracting Nuclear Moments and Charge Radii

Having performed the appropriate calibrations required for the frequency conversion, and determining the properties of any potential satellite peaks present in the spectrum, it was possible to perform a full analysis using the data for all isotopes.

6.4.1 Fitting Even-N Spectra

The even-N spectra each contain one resonance peak as their nuclear spins are equal to zero. The spectrum of each run file was fitted using a Lorentzian line shape and assuming the presence of two satellite peaks. The decision to fit assuming the presence of two satellite peaks was based on the fact that from the isotope shifts between ^{50}Cr and ^{52}Cr (measured on the 425 nm line during the January 2021 campaign), it was apparent that using more than two satellite peaks in the model does not significantly impact the isotope shifts extracted, as shown in figure 6.13. The approximately 30 MHz spread in the isotope shifts shown in figure 6.13 is a reflection of the challenges associated with fitting and extracting information from the spectra measured in the January 2021 campaign. Two satellite peaks were also modelled for the spectra obtained in the July 2021 campaign; the satellite peak analysis showed that the Poisson factors were very small for these spectra, therefore the amplitude of any further satellite peaks would be negligible.

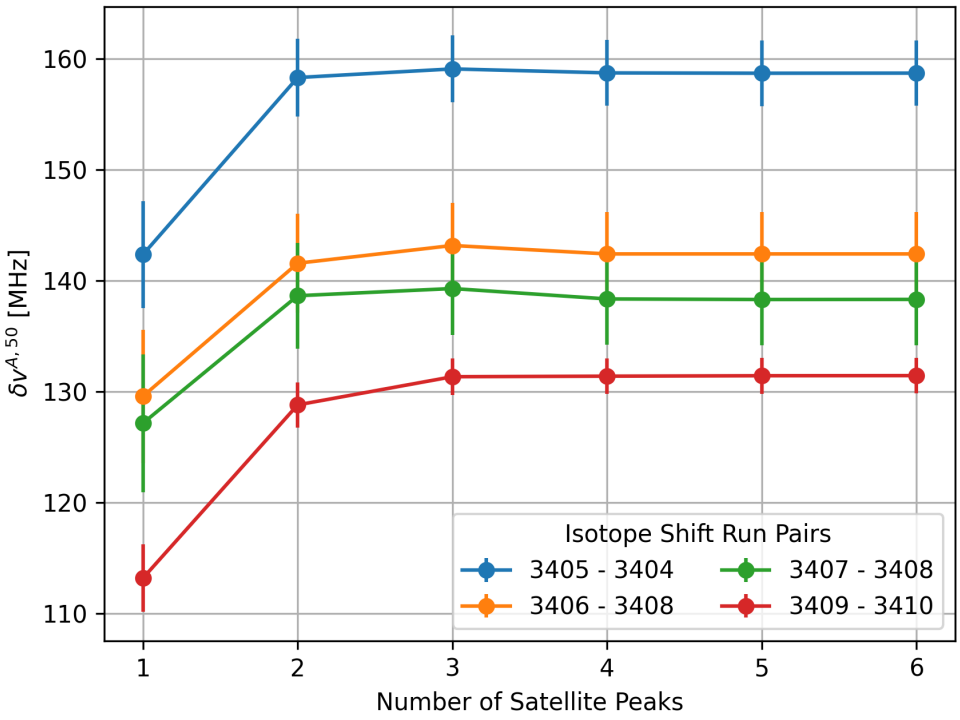

Figure 6.13: A plot to show the isotope shifts between ^{50}Cr and ^{52}Cr spectra as a function of the number of satellite peaks modelled in each spectrum. The legend shows which run files were used when calculating the isotope shifts. ^{50}Cr was used as the reference isotope in each case.

6.4.2 Fitting Odd-N Spectra

The odd-N spectra have a much more complex structure and are therefore more difficult to model, particularly due to the fact that in all of the spectra obtained, there are no individually resolved peaks. In this analysis, the spectra obtained from the January 2021 and July 2021 experimental campaigns were modelled separately, however, certain fitting parameters obtained from the July 2021 data were used when modelling the January 2021 data. This is because, as mentioned previously, the spectra measured in the July 2021 campaign are much more clearly resolved meaning that the hyperfine parameters extracted were much more precise. When modelling the spectra obtained in the January 2021 campaign, the fitting parameters corresponding to the hyperfine parameters common to both the January 2021 and July 2021 data were fixed to the values obtained from the July 2021 data.

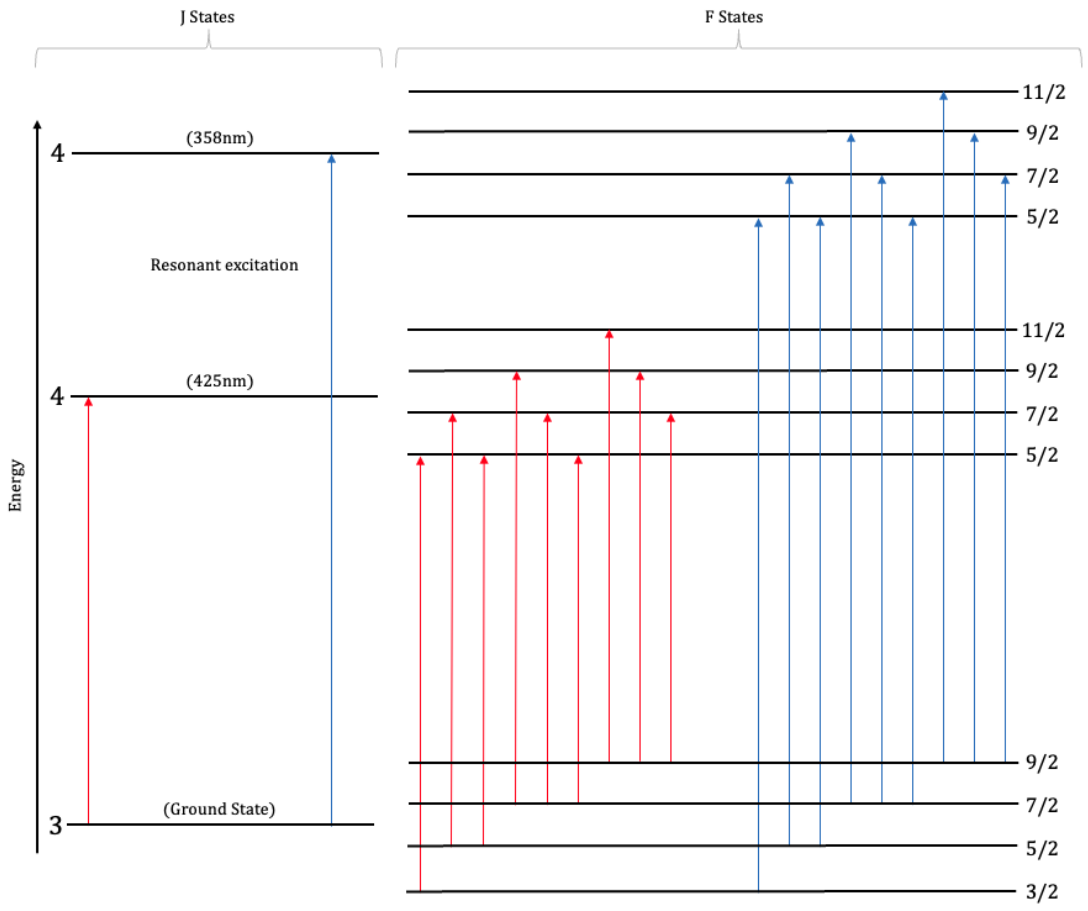

Figure 6.14: A schematic to illustrate the hyperfine level schemes produced on the 358 nm and 425 nm lines for an $I = 3/2$ nucleus.

The hyperfine spectra obtained for ^{53}Cr, which was the only odd-N isotope measured in the July 2021 campaign, were fitted using a model which had the following features:

- The ^{53}Cr spectra measured on 425 nm line were fitted using Lorentzian line shapes, Racah intensities, and assuming the presence of two satellite peaks per resonance peak.
- A single fitting parameter representing the ground state hyperfine parameter, A_l, was shared across all of the ^{53}Cr spectra measured during this campaign.
- A single fitting parameter representing the ratio between the upper and lower state A hyperfine parameters (henceforth referred to as the A-ratio), $A_u : A_l$, was shared across all of the ^{53}Cr spectra measured during this campaign.
- Single fitting parameters for each of the upper and lower state B hyperfine parameters, B_u and B_l, respectively, were shared across all of the ^{53}Cr spectra measured during this campaign.

As previously discussed, the 358 nm and 425 nm lines both originate from the ground state of atomic chromium, as illustrated in figure 6.14, therefore it is possible to fit the spectra produced on both lines simultaneously in such a way that the fitting parameters that represent transition independent parameters, such as the ground state A and B hyperfine parameters for each isotope, are shared across both transitions. This is not the case for the hyperfine parameters of the upper states. This practice increases the number of statistics being used when optimising these parameters, therefore yielding better results. A sophisticated model was used to fit the odd-N spectra for both transitions obtained from the January campaign simultaneously. This model had the following features:

- The spectra were fitted using Lorentzian line shapes, Racah intensities, and assuming the presence of two satellite peaks per resonance peak.
- For each isotope, a single fitting parameter representing the transition independent ground state hyperfine parameter, A_l, was shared across each spectrum, with the exception of ^{53}Cr. This A_l parameter was fixed to the value obtained from the July 2021 analysis.
- For measurements made on the 358 nm line, a single fitting parameter representing the 358 nm A-ratio was shared across each spectrum. For the measurements made on the 425 nm line, the fitting parameter representing the 425 nm A-ratio was fixed to the value obtained from the July 2021 analysis.
- For each isotope, a single fitting parameter representing the transition independent ground state B hyperfine parameter, B_l, was used, with the exception of ^{53}Cr. This B_l parameter was fixed to the value obtained from the July 2021 analysis.
- For each isotope and transition, a single fitting parameter representing the transition-dependent upper state B hyperfine parameter, B_u, was used, with the exception of ^{53}Cr on the 425 nm line. This B_u parameter was fixed to the value obtained from the July 2021 analysis.
- For each run file the Poisson factor, λ, was constrained to adopt a value within the range of 0.62 and 0.78, and was assigned a a starting estimate of 0.7.

The spectra measured for all odd-N isotopes comprise unresolved resonance peaks on both the 358 nm and 425 nm lines. For this reason, it was appropriate to simplify the models in order to avoid 'over-parameterisation', which is why Lorentzian line shapes and Racah intensities were adopted.

The Poisson parameters were limited in this analysis as a more preliminary analysis showed that when left free they would assign themselves to a large range of values, which did not follow any particular trend. Furthermore, when left free, the Poisson parameters may adopt values well in excess of the value at which the magnitude of the first satellite peak exceeds that of the resonance peak, which is unlikely and would result in the wrong assignment of the resonance peak, thus shifting the centroid frequency. The Poisson parameter is directly related to the conditions in the CEC. The Poisson factors determined in this analysis are large and therefore indicative of high temperatures and pressures in the CEC, which results in less optimal spectra. Additionally, as the conditions in the CEC change gradually, it would be expected that the Poisson factors determined from each consecutive run file would follow a trend, whereas, in reality, they appear to be much more sporadic. For this reason, it was appropriate to constrain the values that the Poisson parameter may adopt. As ^{50}Cr was measured regularly for both transitions, the weighted mean of the Poisson factors determined for this isotope was calculated, this would be the starting estimate of the Poisson parameter assigned for each run file. The range in which the parameter is constrained to is $\pm 1\sigma$, where σ is the standard error of the weighted mean inflated by the Birge ratio (λ could adopt a value between $0.62 - 0.78$).

6.4.3 Calculating Isotope Shifts

As mentioned previously, reference scans of stable isotopes are made throughout the duration of an online experimental run. The purpose of this is so that isotope shift calculations can be performed using these reference scans, without which large periods of time may elapse between scans of the isotopes of interest and the stable isotope(s), and therefore the isotope shifts determined may be susceptible to systematic drifts which alter the measured centroid of a particular spectrum over time.

During the January 2021 experimental campaign, both ^{50}Cr and ^{52}Cr were used as reference isotopes when making measurements using the 358 nm transition, and ^{50}Cr was used as the reference when making measurements on the 425 nm line. The reference isotope chosen for the July 2021 experimental campaign is ^{52}Cr. The isotope shifts and changes in mean-square charge radii reported in this thesis are all reported with reference to ^{52}Cr to simplify the comparisons between this isotope chain and others in the region. It is the convention to report the changes in mean-square charge radii relative to the closed shell isotope, which in this region are the $N = 28$ isotopes.

Isotope shifts were calculated between run files that were either directly adjacent or near adjacent in the order of measurement. For each isotope, the weighted average of the isotope shifts was calculated, as were the standard error of the weighted average and the Birge-modified standard error. The error assigned to the weighted average was the larger of the two calculated errors. Where necessary, the isotope shifts were converted to be relative to ^{52}Cr using the experimentally determined $\delta v^{50,52}$ values for each transition.

Chapter 7

Results and Discussion

Once the optimised parameters were extracted from the models fitted to the spectra, it was possible to calculate the nuclear moments and mean-square charge radii of the isotopes being studied. These values are presented in the following section.

7.1 King Plots

In order to extract the charge radii from the experimentally determined isotope shifts, mass and field shift factors must be determined. This was achieved using a King plot with non-optical data (see equation 3.4.2), where the changes in mean-square charge radii were taken as those from Aufmuth *et al.* [10], the isotope shifts were taken as those determined from the January 2021 analysis.

The King plots shown in figures 7.1 and 7.2 were used to extract the mass and field shift factors for the 425 nm and 358 nm transitions, respectively. The mass shift factor determined for the 425 nm line is (119 ± 12) GHz u, with a corresponding field shift factor of (-505 ± 80) MHz fm^{-2}. It can be seen from figure 7.1 that the line of best fit intersects all three of the data points when taking into account their associated errors, although the data point for ^{53}Cr lies further from the line of best fit. This is a consequence of the data point having large associated errors, therefore giving it less weighting in the linear regression.

The mass shift factor determined for the 358 nm line is (1100 ± 12) GHz u, with a corresponding field shift factor of (-13 ± 103) MHz fm^{-2}. The very small 358 nm field shift factor, coupled with its large associated error, means it is not suitable for calculating changes in mean-square charge radii; therefore all changes in mean-square charge radii reported below are those calcu-

lated using the isotope shifts determined for the 425 nm line.

It is noted that the magnitude of the field shift factors determined for each transition are in agreement theoretical expectation. The 425 nm transition is an s electron becoming a p electron, which corresponds to a large change in electron density (the $\Delta|\psi(0)|^2$ term in equation 3.3.12) due to the minimal spatial overlap between the s orbital, which itself has a large overlap with the nuclear volume, and the p orbital. For this reason, s to p transitions are particularly sensitive to the mean-square charge radius as they produce large field shifts. Conversely, the 358 nm transition is a d electron becoming a p electron, and as expected this resulted in a smaller field shift factor than that of the 425 nm transition. Furthermore, the mass shift factor determined for the 358 nm transition is greater than that of the 425 nm transition, again in aligned with expectation as transitions involving d electrons produce large specific mass shifts [46].

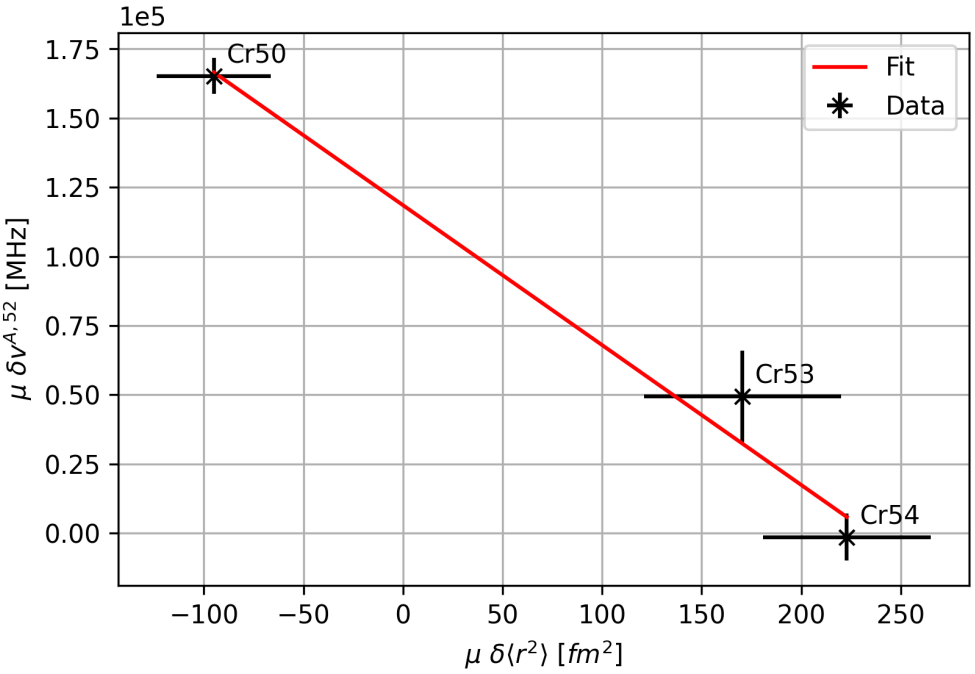

Figure 7.1: The King Plot for the 425 nm transition. The mass and field shift factors determined from this plot were (119 ± 12) GHz u and (-505 ± 80) MHz fm^{-2}, respectively.

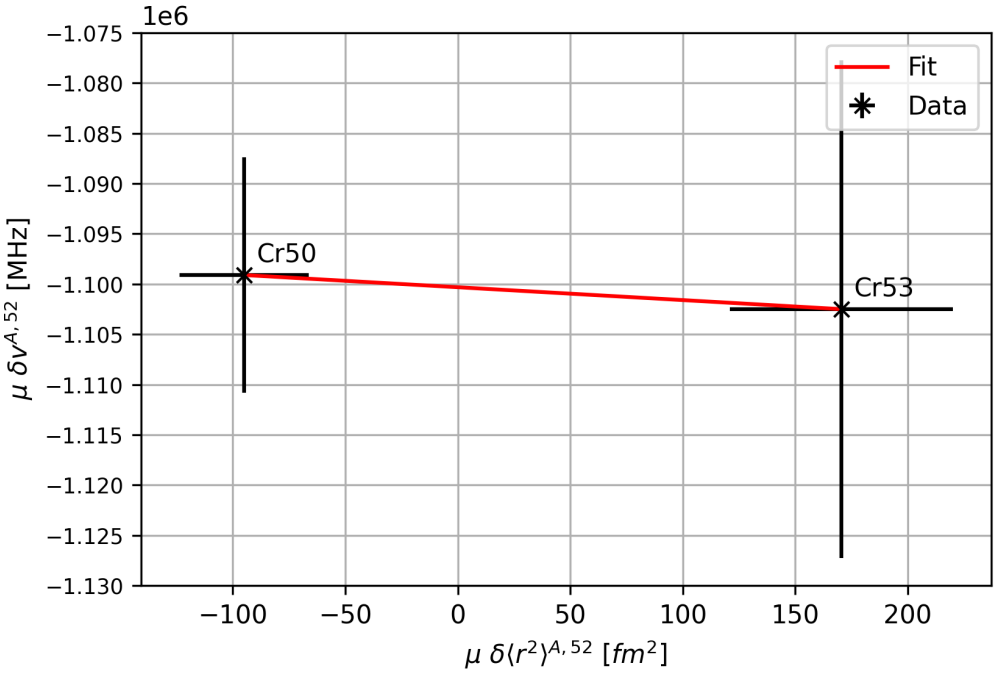

Figure 7.2: The King Plot for the 358 nm transition. The mass and field shift factors determined from this plot were (1100 ± 12) GHz u and (-13 ± 103) MHz fm^{-2}, respectively.

7.2 Magnetic Dipole and Electric Quadrupole Moments

The hyperfine parameters extracted from the fitting were used to calculate the nuclear magnetic dipole and electric quadrupole moments using equations 3.1.33 and 3.1.34, respectively. The A_l and B_l hyperfine parameters determined for ^{53}Cr from this work were in agreement with their literature values; for this reason, they were used as the reference parameters in the calculations, matched to the literature values of the magnetic dipole and electric quadrupole moments of ^{53}Cr: $\mu = -0.47454(3)\,\mu_N$ [65] and $Q_s = -0.15(5)$ b [66]. The experimentally derived $A_u : A_l$ ratios for the 358 nm and 425 nm lines are 0.964(3) and 0.134(2), respectively.

Isotope (A)	I^π $\hbar$	A_l Exp (MHz)	A_l Lit (MHz)	μ Exp (μ_N)	μ Lit (μ_N)
49	$5/2^-$	$-50.0(7)$	—	$-0.480(7)$	0.476(3)
51	$7/2^-$	$-69.6(3)$	—	$-0.935(5)$	$(-)0.934(5)$
53	$3/2^-$	$-82.4(3)$	$-82.5985(15)$[1]	—[2]	$-0.47454(3)$[3]

Table 7.1: A table of the available literature and experimental A hyperfine parameters determined in this analysis. Errors are reported in parentheses. [1] Taken from the work of Childs *et al.* [67]. [2] Literature magnetic dipole moment used as the reference. [3] Taken from the Nuclear Moments and Charge Radii Database [65].

Transition (nm)	Isotope (A)	I^π $\hbar$	B_l Exp (MHz)	B_l Lit (MHz)	B_u Exp (MHz)	Q_{s,B_l} Exp (b)	Q_{s,B_u} Exp (b)	Q_s Lit (b)
358	49	$5/2^-$	$-17(47)$	—	$-67(55)$	$+25(427)$	$+0.9(9)$	—
	51	$7/2^-$	$-2(23)$	—	$-5(31)$	$+3(62)$	$+0.07(40)$	—
	53	$3/2^-$	$+0.1(1.7)$	$-0.003(8)$	$+12(6)$	—[3]	—[3]	$-0.15(5)$[4]
425	49	$5/2^-$	—[1]	—	$-13(55)$	—[1]	$-0.3(1.0)$	—
	51	$7/2^-$	—[1]	—	$+11(26)$	—[1]	$+0.2(5)$	—
	53	$3/2^-$	—[1]	$-0.003(8)$[2]	$-8(1)$	—[3]	—[3]	$-0.15(5)$[4]

Table 7.2: A table of the available literature and experimental B hyperfine parameters determined in this analysis. Errors are reported in parentheses. [1] These values are the same as those for the 358 nm transitions as both transitions originate from the same J state. [2] Taken from the work of Childs *et al.* [67]. [3] Literature value of electric quadrupole moment used as the reference. [4] Taken from the work of Ertmer *et al.* [66]. There are no known B_u values known for both the 358 nm and 425 nm transition in the literature.

With reference to table 7.1, it can be seen that the A hyperfine parameter for the lower J state of ^{53}Cr is in excellent agreement with the literature value. Furthermore, when calculating the magnetic dipole moments using the experimentally determined A hyperfine parameters of ^{49,51,53}Cr, and the literature value of the magnetic moment of ^{53}Cr, the experimentally determined magnetic moments of ^{49,51}Cr are also in excellent agreement with literature. The sign of the nuclear magnetic moment of ^{51}Cr is also confirmed to be negative, whereas previously the negative sign had only been tentatively assigned.

With reference to table 7.2, it can be seen that the B hyperfine parameter for the lower J state of ^{53}Cr is consistent with literature. However, this is unsurprising due to the exceedingly high

error associated with the experimental value. The theme of large associated errors is continued for the B_l hyperfine parameters determined for ^{49,51}Cr, and for B_u parameters determined for each isotope on both lines, perhaps with the exception of the B_u parameter determined for ^{53}Cr when measured on the 425 nm line. The electric quadrupole moments, calculated using each of the B hyperfine parameters (using the experimentally determined B hyperfine parameters and literature electric quadrupole moment of ^{53}Cr as a reference), inherit these large associated errors. Therefore, each quadrupole moment determined for ^{49,51}Cr, regardless of which B parameter was used in the calculation, is consistent with 0 b, and in all but one case may be assigned either a negative or positive value. It is therefore not possible to comment on the type, or magnitude, of nuclear deformation of the ^{49,51}Cr nuclei.

It was anticipated that both of the transitions used in this study would exhibit little sensitivity to the quadrupole moments, in part due to the fact that the ground state B hyperfine parameter from the literature is very small, and in part due to the fact that the spectra obtained using either transition have collapsed structures with unresolved peaks. It is the relative positions of these unresolved peaks to one another from which the B hyperfine parameters are determined. Couple this with the fact that each of these unresolved resonance peaks will have its own series of unresolved satellite peaks, and it becomes clear why it is not possible to extract precise B hyperfine parameters - to do so is too computationally complex and based on too many assumptions.

7.3 Isotope Shifts and Mean-Square Charge Radii

The isotope shifts and corresponding changes in mean-square charge radii determined from this work are presented below. Table 8 and figure 7.3 show the remarkable agreement between the isotope shifts and changes in mean-square charge radii determined from the January 2021 data set and the literature values from Aufmuth *et al.* [10]. All changes in mean-square charge radii determined are consistent within errors with the literature values, as are all of the isotopes shifts, with the only exception being $\delta\nu^{50,52}_{358\,nm}$, which becomes consistent with literature with a $1.\dot{6}\sigma$ uncertainty. This gives confidence that the newly reported isotope shifts and charge radii determined from this experimental campaign are accurate.

Isotope (A)	I^{π} ($\hbar$)	$\delta\nu^{A,52}_{358\,nm}$ Exp (MHz)	$\delta\nu^{A,52}_{358\,nm}$ Lit (MHz)	$\delta\nu^{A,52}_{425\,nm}$ Exp (MHz)	$\delta\nu^{A,52}_{425\,nm}$ Lit (MHz)	$\delta\langle r^2\rangle^{A,52}$ Exp (fm^2)	$\delta\langle r^2\rangle^{A,52}$ Lit (fm^2)
48	0	+1747(14)	—	−253(7)	—	+0.125(14)[44]	—
49	$5/2^-$	+1285(27)	—	−186(6)	—	+0.092(12)[32]	—
50	0	+845(9)	+815(15)[1]	−127(5)	−130.3(2.0)[2]	+0.071(10)[22]	0.073(22)[4]
51	$7/2^-$	+409(7)	—	−42(5)	—	−0.005(10)[9]	—
53	$3/2^-$	−401(9)	−384(12)[1]	+18(6)	+23(3)[2]	+0.050(12)[12]	0.062(18)[4]
54	0	—	−770(12)[1]	−1(6)	0(6)[3]	+0.169(12)[32]	0.159(30)[4]

Table 7.3: A table of the available literature and experimental isotope shifts and changes in mean-square charge radii determined from the January 2021 campaign. Statistical errors are reported in round brackets and systematic errors are reported in square brackets. Changes in mean-square charge radii were calculated using the isotope shifts determined on the 425 nm line. [1]Taken from the work of Fricke [68], [2]taken from the work of Furmann [60], [3]taken from the work of Heilig and Wendlandt [69], [4]taken from the work of Aufmuth [10].

Isotope (A)	I^{π} ($\hbar$)	$\delta\nu^{A,52}_{425\,nm}$ Exp (MHz)	$\delta\nu^{A,52}_{425\,nm}$ Lit (MHz)	$\delta\langle r^2\rangle^{A,52}$ Exp (fm^2)	$\delta\langle r^2\rangle^{A,52}$ Lit (fm^2)
50	0	−148(1)	−130.3(2.0)[1]	+0.113(2)[26]	0.073(22)[3]
53	$3/2^-$	+18(1)	+23(3)[1]	+0.050(2)[12]	0.062(18)[3]
54	0	+9(1)	0(6)[2]	+0.149(2)[29]	0.159(30)[3]

Table 7.4: A table of the available literature and experimental isotope shifts, and changes in mean-square charge radii determined from the July 2021 campaign. Statistical errors are reported in round brackets and systematic errors are reported in square brackets. [1]Taken from the work of Furmann *et al.* [60], [2]taken from the work of Heilig and Wendlandt [69], [3]taken from the work of Aufmuth *et al.* [10].

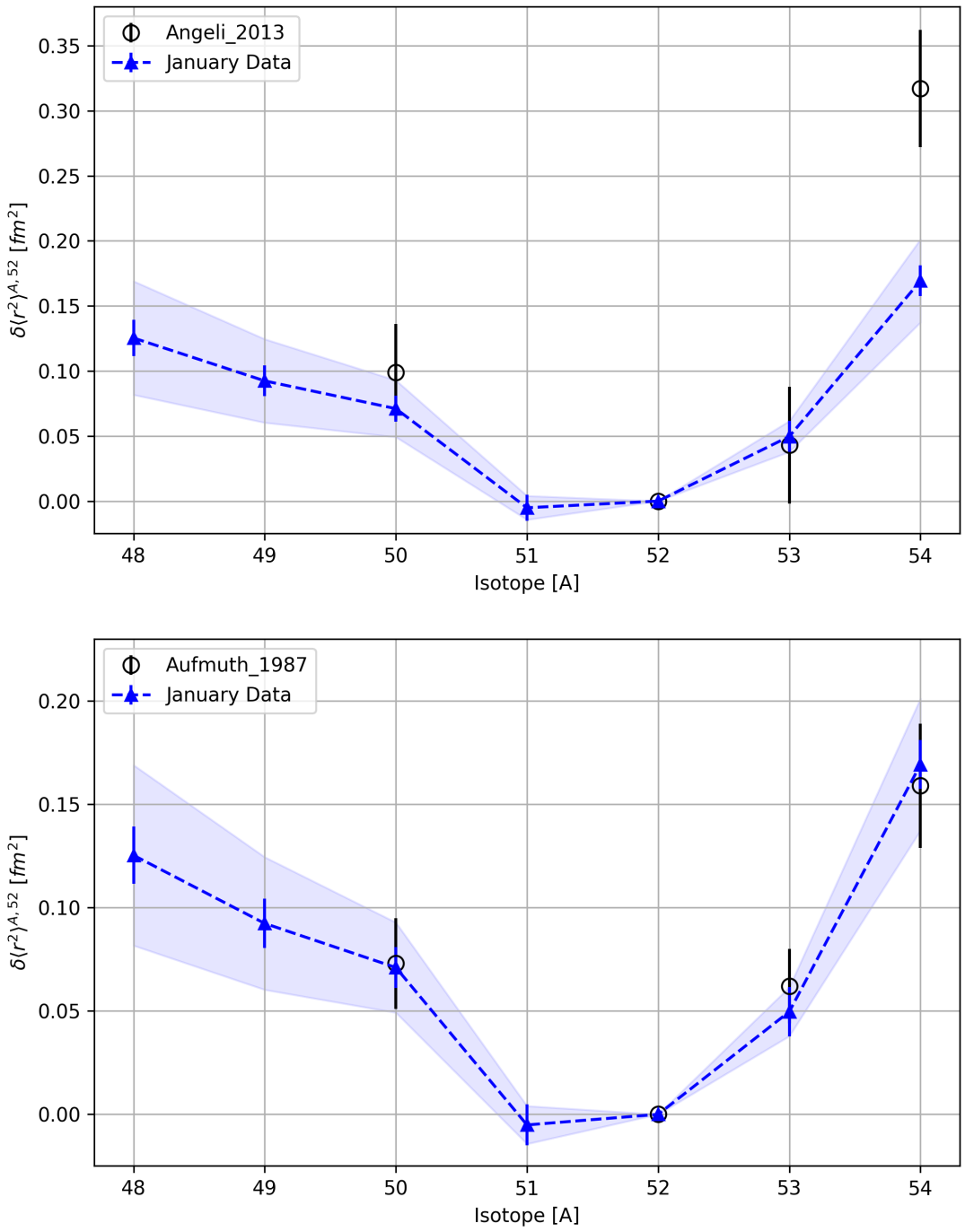

Figure 7.3: Plots to show the literature and experimental changes in mean-square charge radii relative to ^{52}Cr determined from the January 2021 campaign as a function of isotope. The error bars on the experimental data points represent the statistical uncertainties, whereas the error bands represent the systematic uncertainties inherited from the mass and field shift factors. One standard deviation is presented in both cases. Literature values taken from the work of Angeli and Marinova [11] (top) and Aufmuth *et al.* [10] (bottom). For both plots, the changes in mean-square charge radii were calculated using atomic parameters determined from a King plot that utilised the changes in mean-square charge radii reported in the work of Aufmuth *et al.*

With reference to table 8, it should be noted that the literature values of isotope shift reported for the 358 nm transition are not those reported by Fricke [68], as these appear to be reported with the incorrect sign. This correction has been made in the table. In an example given within this paper, it is noted that the isotope shift is calculated by subtracting the centroid frequency of the spectrum of ^{52}Cr from that of the isotope of interest, therefore the isotope shift is defined to be the same as in this work. However, from the experimental data, it becomes apparent that the isotope shifts reported in Fricke must have been miscalculated, likely by subtracting the centroid frequency of the spectrum of the isotope of interest from that of ^{52}Cr, which would result in the isotope shift having the opposite sign. This likely stems from the fact that the convention for defining the isotope shift is not standardised across the literature, nor is the notation used, as was discussed in the section 3.3. As discussed above, there is strong agreement between the experimentally determined isotope shifts and literature values for the 358 nm line, but this is only the case when the sign of the literature values is reversed, which strongly supports the conclusion that a miscalculation has been made or the values have been misreported in the Fricke paper.

It is noteworthy that there is a disparity between the isotope shifts determined from the July 2021 data set and those of both the January 2021 data set and the literature. One possible explanation for this is that the July 2021 data was collected using an offline ion source, which is able to deliver a significant rate of ions to the laser-spectroscopy beamline. It is possible that too many ions were delivered to the cooler-buncher during each run, which would increase the density of charge and therefore the electrostatic interactions between the ions. This may then have impacted the kinematics of the system resulting in a detrimental shifting of the centroids for each isotope, which manifested itself in the isotope shifts determined. One can determine if these space-charge effects are in play by inspecting the time-of-flight peak for each run file. If the cooler-buncher has been overfilled the time-of-flight peak will have a characteristic tail (e.g. see figure 7.4), this is because the higher charge density causes ions in the bunch to repel one another thus extending the spatial profile of the bunch. As the time-of-flight profile shows the number of photons detected as a function of time elapsed since a bunch left the cooler, if the bunch is spatially diffuse, photons will be detected over a longer time as the bunch will take longer to pass in front of the photo-multiplier tube. Inspection of the time-of-flight profiles from the July 2021 data do not exhibit this tailing, therefore over-filling of the cooler-buncher is most likely not responsible for the discrepancies in results.

An additional consideration to be made is that the data collected in July 2021 was measured

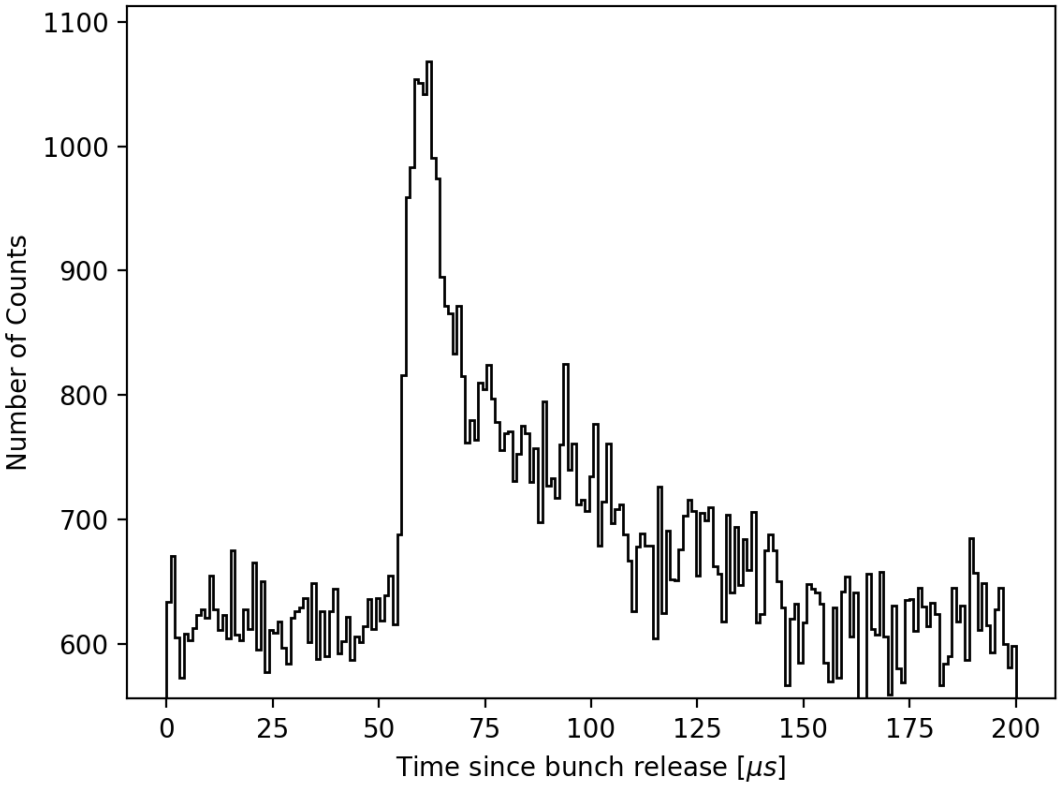

Figure 7.4: A plot to show an example of a typical time-of-flight profile measured when the cooler-buncher has been overfilled with ions.

over approximately a five-hour period. At face value this could be considered to be advantageous as measuring data over such a short time period would minimise the impact that slow systematic drifts have on the data. However, it is often the case that elements in the experimental setup need time to equilibrate with the lab conditions. For example, the laser cavity is very sensitive to changes in temperature, air pressure, and humidity. It may be the case that after optimising the lasers, in response to the local conditions, the frequency of the resonance laser drifted without detection. A reference cell is used to stabilise and lock the frequency of the laser, however, it is possible that the response of the reference cell may also be impeded by changing conditions. Online experiments usually take place over several days or weeks, and considerable time before the experiment is spent ensuring that the experimental setup has been optimised. As such, there is sufficient time for all elements of the setup to stabilise before any online measurements are taken. Alternatively, there may be a systematic error that impacts the centroid location of each spectrum, for example, an issue with the laser wavenumber, cooler voltage, or tuning voltage read-back. It may be the case that the equipment used to measure these values also needed additional time to equilibrate with the local conditions, this is to say that it is possible that the laser wavenumber, cooler voltage and tuning voltages used were appropriate, but that the measurements of them were not.

In order to determine if either the cooler voltage or measurements of the cooler voltages may have impacted the centroid frequencies of the spectra obtained in the July 2021 campaign, the average of the measured cooler voltages for each run was plotted as a function of run number, as shown in figure 7.5. From the figure, it is observed that, with the exception of the initial two runs, the measured cooler voltage appears to be relatively consistent throughout the experimental campaign. If either the actual cooler voltage was drifting (and the measurement of the cooler voltage was accurate), or the measurements of cooler voltage were subject to inaccuracies due to any changing properties of measurement equipment, an upwards or downwards trend would be seen in the figure 7.5. From the available data, neither of these effects appear to manifest themselves. It should be noted that if the actual cooler voltage was drifting, its impact would be negligible as this would still be accounted for when performing the voltage-to-frequency conversion, assuming that the measurements of the cooler voltage were accurate. Although it appears that the cooler voltages, or measurements of them, are not responsible for any centroid shifting effects, it is not possible to rule out the possibility that the actual cooler voltage and the properties of the measurement device were both changing in response to local conditions and the combined effects are masking one another in the recorded data.

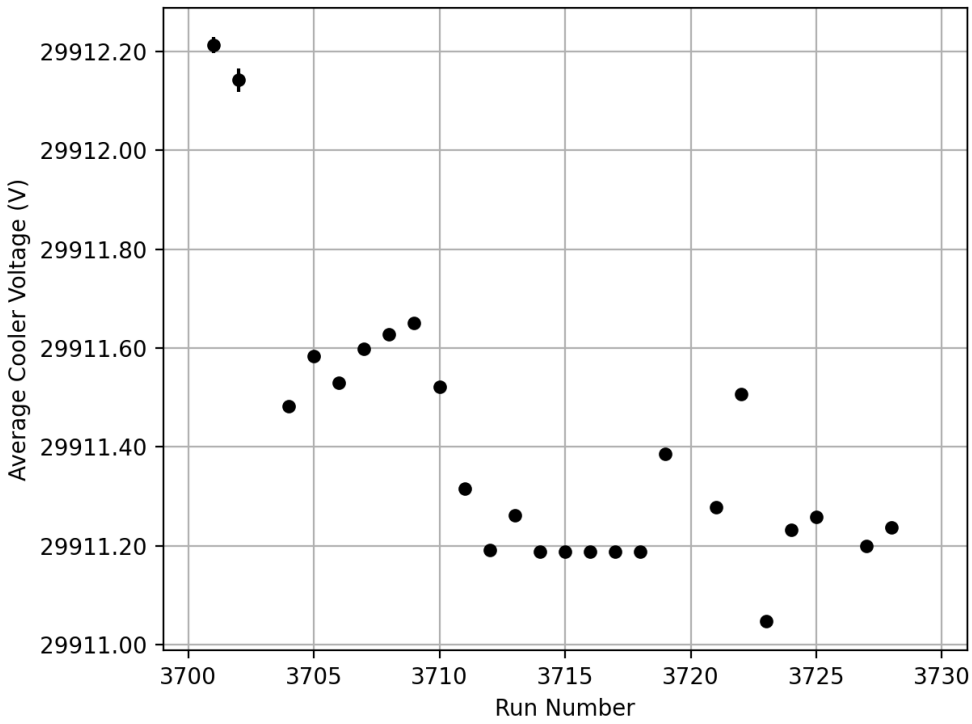

Figure 7.5: A plot to show the average of the cooler voltages measured during each run of the July 2021 experimental campaign as a function of the run number.

Despite the disparity between the isotope shifts, the charge radii extracted using the July 2021 data set are still consistent with both the charge radii determined from the January 2021 data set and the literature values when including the systematic errors. These measurements are therefore still of value, however, moving forward the discussion will revolve around the January 2021 data set as it provides better agreement with the literature, and includes the newly reported charge radii measurements.

Angeli and Marinova [11] is a commonly cited source of literature, however, as can be seen in figure 7.3, there is a large disparity between the change in mean-square charge radius reported for ^{54}Cr when compared to both the experimentally determined values (from both the January 2021 and July 2021 campaigns) and the value reported in Aufmuth *et al.* [10]. For this reason, it is assumed that the value reported by Angeli and Marinova [11] is incorrect, and the values reported by Aufmuth *et al.* are assumed to be a more appropriate set of values for comparisons to be made with. It is for this reason that the values of the changes in the mean-square charge radii used in the King plots were those reported by Aufmuth *et al.*.

Having obtained the chromium charge radii, with reference to figure 7.3, it is observed that above the $N = 28$ shell closure the mean-square charge radii increase as neutrons are added to the system. This is in line with expectations as it was known from the available literature that the charge radii of ^{53,54}Cr are greater than that of ^{52}Cr, and also due to the fact that the same trend is observed for all other isotope chains in the region. Below the $N = 28$ shell closure the mean-square charge radii also increase as neutrons are removed from the system, with the exception of ^{51}Cr which is reported to have a charge radius slightly smaller than that of ^{52}Cr. It is anticipated that ^{52}Cr should have the smallest charge radius owing to its magic number of neutrons, however, when taking into account its associated errors, ^{51}Cr may also adopt a charge radius larger than that of ^{52}Cr. The similarity of the charge radii of ^{51}Cr and ^{52}Cr is not unexpected as, with reference to figure 7.6, it is observed that for both the calcium and titanium isotope chains the $N = 27$ isotopes are of a similar size to the $N = 28$ isotopes. For both chains the $N = 27$ isotopes are slightly larger than their magic neighbours, however when considering errors may also be equal in size to, or in the case of calcium, smaller than, their $N = 28$ isotopes respectively.

Another feature present in figure 7.3 is the odd-even staggering along the isotope chain, this being another characteristic feature that is shared with both calcium and titanium. For each isotope chain, as one approaches the mid-shell the charge radii increase sequentially and in a

non-linear fashion as can be seen in figure 7.6. It is possible to compare the magnitude of the OES along the chromium isotope chain to that of the calcium and titanium chains quantitatively using the three-point OES parameter, $\Delta_r^{(3)}$, defined as:

$$\Delta_r^{(3)} = \frac{1}{2}\left(r_{A+1} - 2r_A + r_{A-1}\right), \tag{7.3.1}$$

where r_A is the charge radius of an isotope with A nucleons.

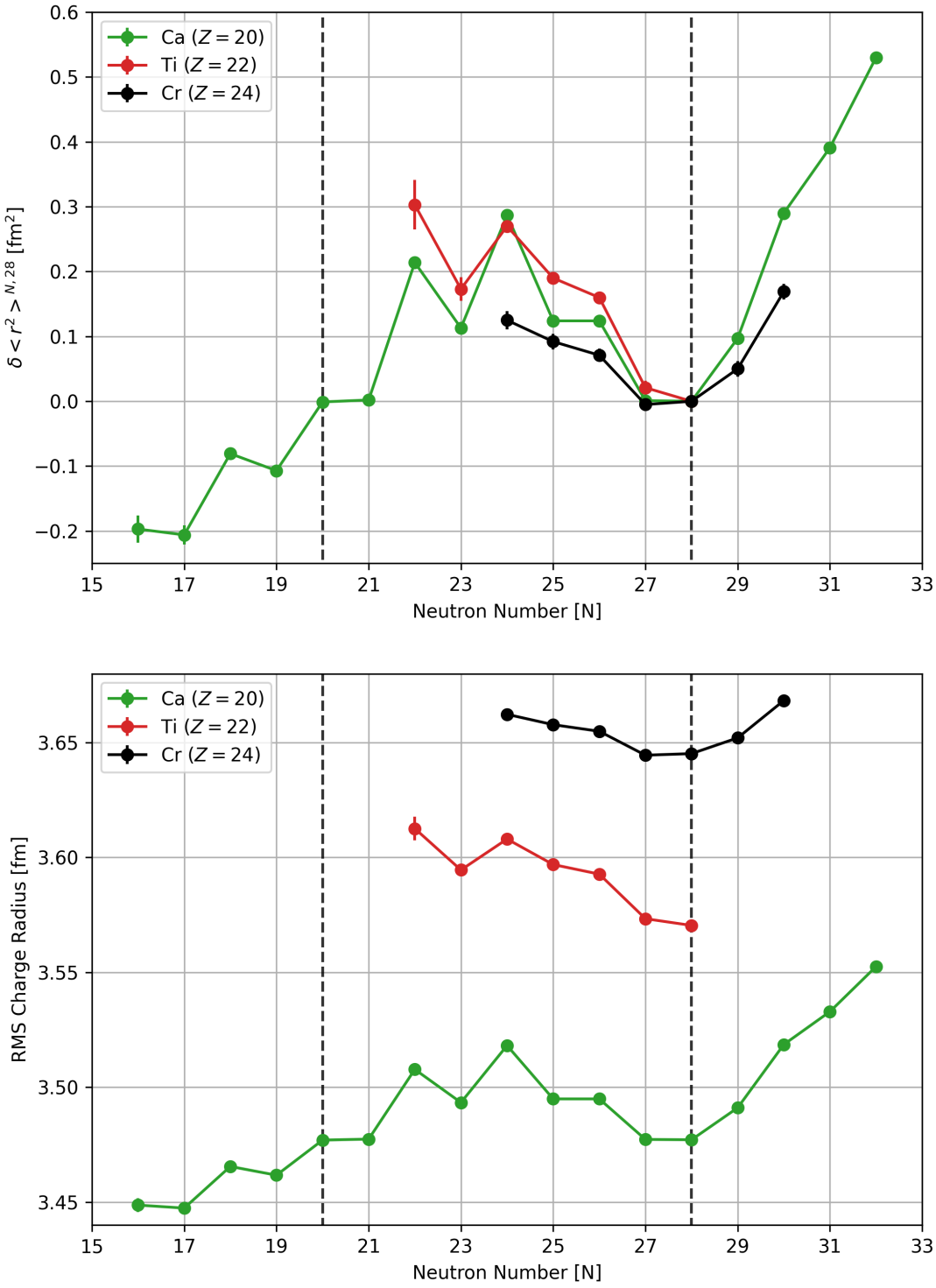

Figure 7.6: Plots to show the the changes in means square charge radii of calcium, titanium and chromium relative to their $N = 28$ isotopes (top), and the absolute charge radii of calcium, titanium and chromium (bottom). The dashed lines represent the N = 20 and N = 28 shell neutron closures. Error bars represent statistical uncertainties. The absolute charge radii of the reference nuclides are taken as those reported in Angeli and Marinova [11] and their associated errors are taken to be zero in each case. Literature values obtained Garcia Ruiz *et al.* (Ca) [5], Miller *et al.* (Ca) [6], and Angeli and Marinova [11].

Figure 7.7 shows the odd-even staggering along the calcium, titanium, and chromium isotope chains, from which it is apparent that as pairs of protons are added to the nuclear system, and one moves towards the proton mid-shell, the magnitude of the odd-even staggering decreases sequentially.

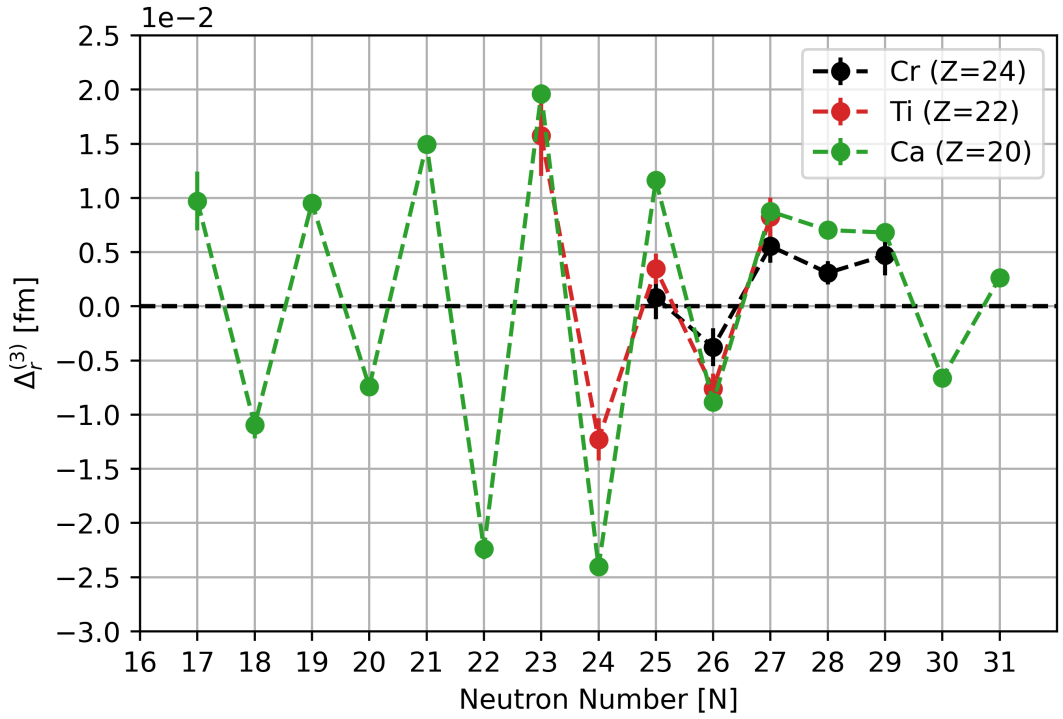

Figure 7.7: A plot of the odd-even staggering along the calcium, titanium, and chromium isotope chains as calculated using equation 7.3.1. The error bars represent statistical uncertainties. The error associated with the absolute charge radii of reference nuclides was taken as zero in each case.

In addition to comparing the charge radii of chromium to those of other isotope chains, they can also be compared to theoretical predictions. Figure 7.8 shows the charge radii of even-even chromium isotopes determined by Kortelainen *et al.* [70] using three different theoretical approaches: an ab-intio coupled cluster (CC) theory employing a two- and three-nucleon ΔNNLO$_{GO}$ interaction, and two approaches based on nuclear density functional theory (one based upon the Skyrme parametrisation (SV-min) energy density functional and one based on the Fayans functional parametrisation Fy(Δr, HFB) energy density functional). Figure 7.8 also shows the changes in mean-square charge radii of even-even isotopes determined by Hemalatha [71] using two different approaches: the relativistic Hartree-Bogoliubov model using the density-dependent meson-exchange functional (DD-ME2), henceforth referred to as DIRHB(DD-ME2), and the non-relativistic Hartree-Fock-Bogoliubov model using the Gogny D1S interaction, henceforth referred to as the HFB(Gogny D1S).

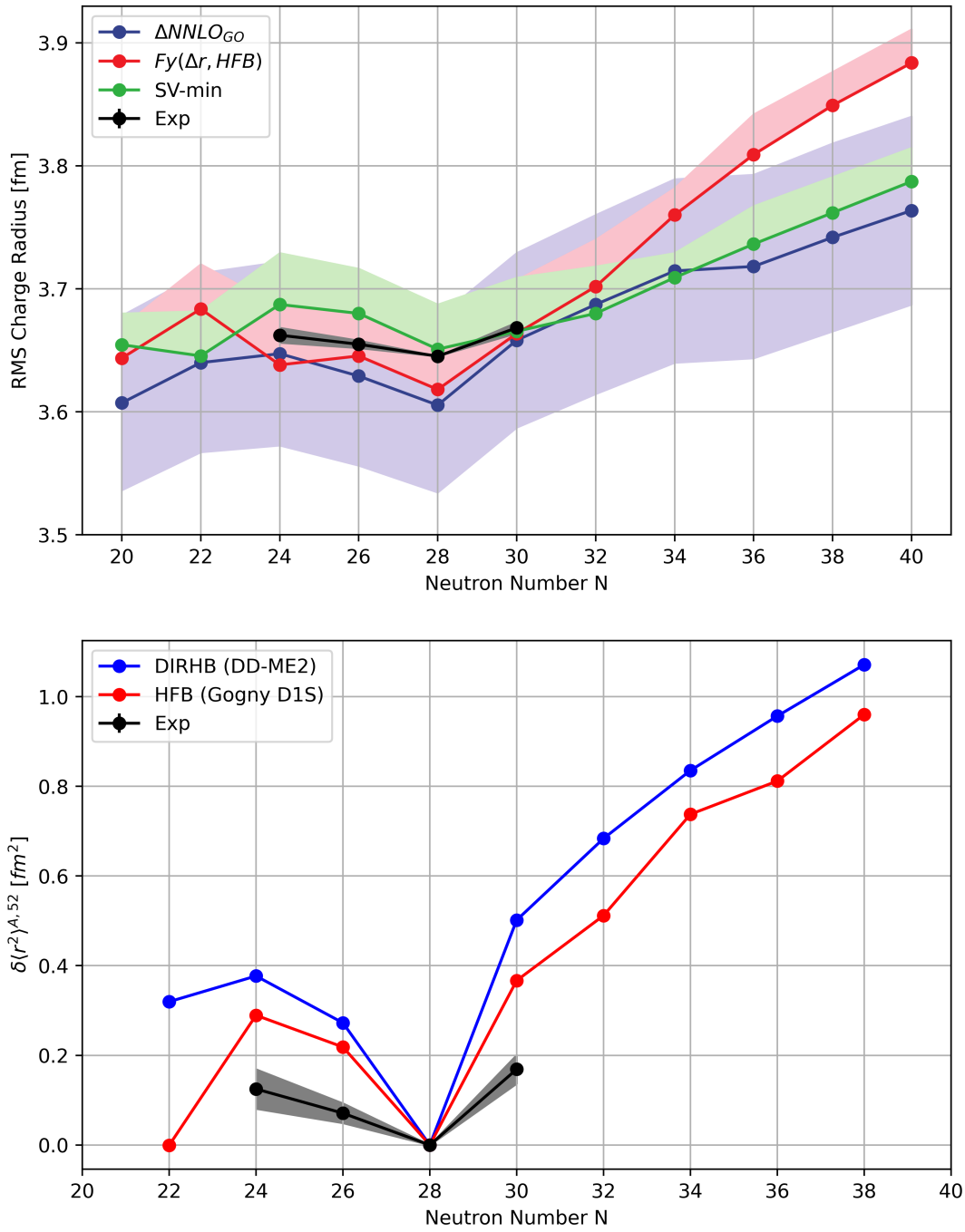

Figure 7.8: A plot to compare the root-mean-square charge radii determined experimentally from this work and theoretically by Kortelainen *et al.* [70] along the chromium isotope chain (top), and a plot to compare the experimentally determined changes in mean-square charge radii with those determined theoretically by Hemalatha [71]. The associated errors for the theoretical predictions (where reported) are presented as error bands. For the experimental values, error bars, which are too small to be visible, and an error band are used to present the statistical and systematic uncertainties, respectively. The absolute charge radius of ^{52}Cr is taken as that reported in Angeli and Marinova [11] and its associated error is taken to be zero.

From figure 7.8 it can be seen that there is good agreement between the predicted charge radii of ^{52}Cr as determined using the SV-min approach with the experimentally determined value, whereas both the ΔNNLO$_{GO}$ and Fy(Δr, HFB) approaches underestimate the value. More interesting is the trend as one moves along the isotope chain, for example, the rate of increase in charge radii between ^{52}Cr and ^{54}Cr is once again best reproduced using the SV-min approach, whereas the ΔNNLO$_{GO}$ and Fy(Δr, HFB) approaches both overestimate the rate of increase, however it is noteworthy that each of the theoretical approaches reproduces the charge radii of ^{54}Cr well. As one moves to the more neutron-deficient isotopes, the trend is best reproduced by the ΔNNLO$_{GO}$ and SV-min models, which show the charge radii to increase as one moves into the middle of the $1f_{7/2}$ neutron shell, whereas the Fy(Δr, HFB) predicts that the $N = 24$ isotope will be the smallest nucleus of those between the $N = 20$ and $N = 28$ shell closures.

With reference to the bottom plot of figure 7.8, it can be seen that the theoretical predictions of Hemalatha are able to reproduce the kink present at $N = 28$, as both models correctly predict the increase in the charge radii relative to the $N = 28$ isotope on either side of the shell closure, with the increase being steeper on the neutron-rich side than the neutron-deficient side. Although both models produce similar trends to those observed experimentally, both greatly overestimate the magnitude of the change in mean-square charge radii along the isotope chain, with no theoretical values shown to be in agreement with those determined experimentally. This is clear when comparing the gradients of the lines connecting the $N = 26$ and $N = 30$ isotopes to the $N = 28$ isotope determined theoretically and experimentally - the gradients determined by theory are much steeper than those determined experimentally.

Finally, recalling the importance of understanding isospin pairing mechanisms in self-conjugate nuclei, the change in mean-square charge radii of ^{48}Cr has been added to the plot presented in the work of Koszorus *et al.* [13] as shown in figure 7.9. It should be noted that the work of Charlwood *et al.* [72] is cited in the Koszorus paper when referencing manganese, however, for the plot in this thesis, the changes in mean-square charge radii of ^{50}Mn, ^{50m}Mn used were those reported in the more recent work of Heylen *et al.* [8] where updated values for the atomic factors were used. It can be seen that the charge radius of ^{48}Cr sits between that of ^{44}Ti and ^{50}Mn as expected. It is also observed that other spin-zero, $T = 1$ states of the self-conjugate nuclei appear to sit on an approximately smooth curve. With the additional data point for chromium, it will become possible to verify whether the $T = 1$ state of ^{46}V behaves the same as the $T = 1$ states of its even-even self-conjugate neighbours once the charge radius of this isotope has been established experimentally. The same is true for ^{50}Mn, however in this instance the

charge radius of ^{52}Fe will need to be determined. In either case, the data points for ^{46}V and ^{50}Mn should lie on the straight lines connecting the data point for chromium with those of titanium and iron, respectively.

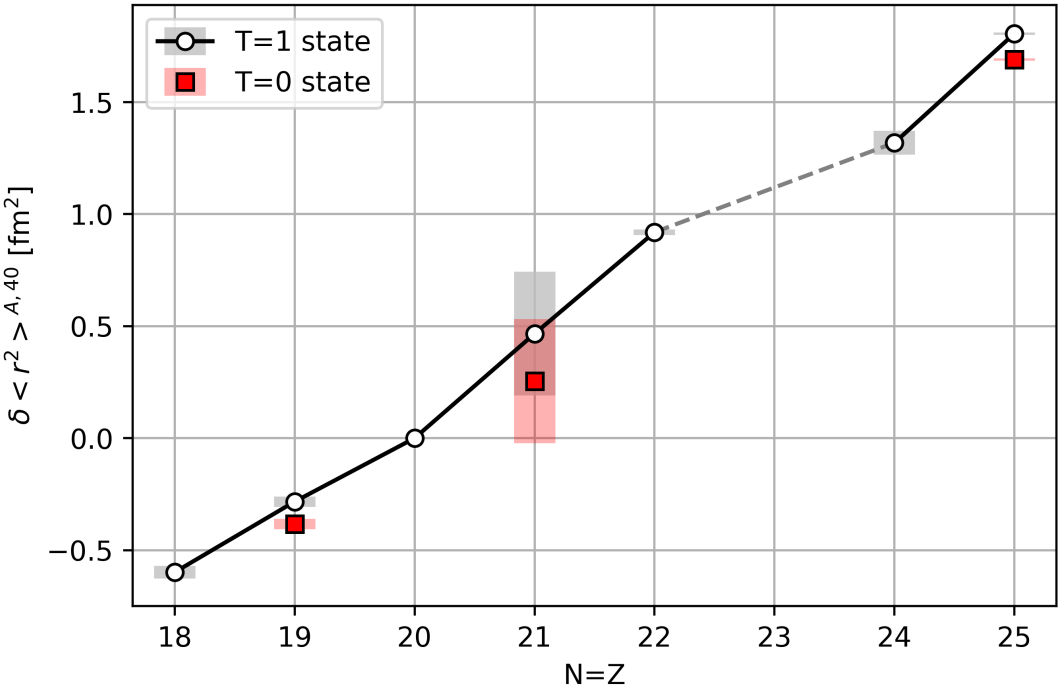

Figure 7.9: A plot to show the changes in the mean-square charge radii relative to ^{40}Ca for the self-conjugate nuclei spanning from ^{36}Ar to ^{50}Mn. This plot is styled like that from the work of Koszorus *et al.* [13] for ease of comparison. The shaded error bars represent the systematic errors associated with the changes in mean-square charge radii only - the error associated with absolute charge radii of the reference nuclides used to produce this plot was taken to be zero. Values are taken from Angeli and Marinova [11] (absolute charge radii of ^{38}Ar ^{40}Ca, ^{48}Ti, ^{55}Mn), Blaum *et al.* [73] (^{36}Ar), Koszorus *et al.* [9] (absolute charge radius of ^{39}K), Bissel *et al.* [12] (^{38}K, ^{38m}K), Koszorus *et al.* [13] (^{42}Sc, ^{42m}Sc), Gangrsky *et al.* [74] (^{44}Ti), and Heylen *et al.* [8] (^{50}Mn, ^{50m}Mn).

Chapter 8

Conclusion and Outlook

8.1 Conclusion

A series of laser spectroscopy experiments were performed at the IGISOL-IV facility, University of Jyväskylä, to probe the hyperfine structure along the chromium isotope chain, and determine how the sizes of the nuclei evolve as one moves into the $1f_{7/2}$ neutron shell. The hyperfine structure of various isotopes of chromium were investigated by probing two different fine structure transitions: the 358 nm ($3d^5\ (^6S)4s\ ^7S_3 \rightarrow 3d^4\ (^5D)4s4p(^3P)\ ^7P_4$) and 425 nm ($3d^5\ (^6S)4s\ ^7S_3 \rightarrow 3d^5\ (^6S)4p\ ^7P_4$) lines.

It was observed that the experimentally determined isotope shifts and those known from the literature were in very good agreement, with all but one being consistent within errors, and the other being consistent within $1.\dot{6}\sigma$ uncertainty. The newly reported isotope shifts reported for each isotope relative to ^{52}Cr for the 358 nm transition are: 1747(14) MHz for ^{48}Cr, 1285(27) MHz for ^{49}Cr, and 409(7) MHz for ^{51}Cr. The newly reported isotope shifts reported for each isotope relative to ^{52}Cr for the 425 nm transition are: $-253(7)$ MHz for ^{48}Cr, $-186(6)$ MHz for ^{49}Cr, and $-42(5)$ MHz for ^{51}Cr. It was also observed that experimental conditions, for example, the conditions within the charge-exchange-cell, can have a significant impact on the quality of the hyperfine spectra measured.

Using the experimentally determined values of isotope shift and known values of changes in charge radii relative to ^{52}Cr from the literature, it was possible to make a King plot to determine the mass and field shift factors associated with each transition. The mass shift factors determined are 1100(12) GHz u and 119(12) GHz u for the 358 nm and 425 nm transition, respectively, and the field shift factors determined are $-13(103)$ MHz fm^{-2} and $-505(80)$ MHz

fm^{-2} for the 358 nm and 425 nm transition, respectively. The field shift factor determined for the 358 nm transition is unsuitable for use when calculating the changes in mean-square charge radii and for this reason, the changes in mean-square charge radii were determined using the mass shift factor, field shift factor and isotope shifts determined using the 425 nm transition.

The changes in mean-square charge radii determined from both the January 2021 and July 2021 campaigns were consistent with one another and the values known in the literature. The newly reported values of the change in mean-square charge radii relative to ^{52}Cr for ^{48}Cr, ^{49}Cr, and ^{51}Cr are $0.125(14)[44]\,\mathrm{fm}^2$, $0.092(12)[32]\,\mathrm{fm}^2$, and $-0.005(10)[9]\,\mathrm{fm}^2$, respectively, where the statistical errors are reported in round brackets and the systematic errors are reported in square brackets. The absolute charge radii and changes in mean-square charge radii have been compared to theoretical predictions determined using state-of-the-art models, which have demonstrated varying degrees of success, with some being able to predict global trends in the region.

8.2 Future Work

The work completed for this thesis is useful and provides a better insight into the evolution of nuclear properties along the chromium isotope chain, however it is clear from the discussion above that additional work needs to be completed to build a more complete understanding of the behaviour of nuclei in this region.

The scope of this work does not cover further exploration of nuclear properties above the $N = 28$ shell closure. As discussed earlier in this thesis, there is a sharp increase in charge radii for the $N > 28$ nuclei in the calcium-nickel region regardless of which element is inspected. Obtaining charge radii measurements for $N > 30$ isotopes of chromium would further aid our understanding of nuclear behaviour on either side of the $N = 28$ shell closure. During this campaign, measurements of the hyperfine spectrum of ^{55}Cr were attempted, however, this was a fruitless endeavour and unfortunately, no resonance peaks were detected. A future campaign to measure the hyperfine spectrum of ^{55}Cr is therefore a priority.

In addition to measuring additional neutron-rich isotopes of chromium, measurements of chromium nuclei deeper in the $1f_{7/2}$ neutron shell, such as ^{47}Cr, would be beneficial. Additional charge radii measurements of the neutron-deficient isotopes of chromium are still required for a more complete understanding of how the charge radii evolve in this region. These additional mea-

surements will allow us to determine if the chromium charge radii continue to increase as one moves below the mid-shell as is the case for titanium, or whether a turning point is established at the mid-shell and the charge radii will begin to decrease, as is the case for calcium.

From the results presented in this thesis it is apparent that the transitions studied in this work had little sensitivity to the electric-quadrupole moments. As such, it would be beneficial to investigate the suitability of alternative transitions for use in any future campaign where the objective is to determine the type and magnitude of any nuclear deformation. For example, by introducing a second frequency doubling cavity into the experimental setup, it would be possible to frequency-quadruple the light output by the laser, this in turn increases the number of transitions that are accessible for study, providing that the power of the laser is sufficient following the loses associated with frequency doubling. It is anticipated that transitions with wavelengths above 205 nm, such as the 205.56 nm, 206.16 nm, and 206.55 nm lines would be suitable for future studies. These transitions are strong and involve spectroscopy of the ion, therefore eliminating the complications and efficiency losses associated with charge exchange. An offline test would determine their sensitivity to the quadrupole moment.

The data obtained in the January 2021 experimental campaign proved very difficult to model in part due to the large peak asymmetries present in the measured spectra. In order to gain a better understanding of how the intensity of the satellite peaks is related to the conditions within the charge-exchange-cell, an offline study could be performed wherein the temperature of the charge-exchange-cell is systematically increased and the impact this has on the measured spectra is quantitatively determined.

One of the key motivations for this work was to procure results that could be compared to the theoretical predictions made using contemporary nuclear models, and thus allow us to evaluate the success of these models. With the addition of the new charge radii reported in this thesis, it is now possible to further develop these contemporary models: the additional data provide new anchor points to be used when calibrating the theoretical results to the experimentally determined observables.

As was mentioned in the introduction, this series of experiments that form this thesis work are part of a larger campaign to collate additional data in the calcium-nickel region of the chart of nuclides. Measuring other elements in the region is a priority. Recent experiments have been performed to measure the cobalt and iron isotope chains. At the time of writing, the data

obtained from these experiments are still being analysed, but the complimentary results yet to be realised will certainly aid our understanding of the regional systematics in the calcium-nickel region.

"Given the pace of technology, I propose we leave math to the machines and go play outside."

– Calvin, Calvin and Hobbes.

Appendix A: Natural Line Width Derivation

Beginning with equation 3.5.7:

$$F(\omega) = \int_{-\infty}^{\infty} e^{-At/2} \cdot \cos(\omega_{10} t) \cdot e^{-i\omega t} dt, \tag{A.1}$$

using the identity:

$$\cos(\omega_{10} t) = \frac{1}{2}\left(e^{i\omega_{10} t} + e^{-i\omega_{10} t}\right), \tag{A.2}$$

the equation becomes:

$$F(\omega) = \frac{1}{2}\int_{-\infty}^{\infty} e^{-At/2} \cdot \left(e^{i\omega_{10} t} + e^{-i\omega_{10} t}\right) \cdot e^{-i\omega t} dt, \tag{A.3}$$

$$\therefore F(\omega) = \frac{1}{2}\int_{-\infty}^{\infty} e^{-At/2} \cdot \left(e^{i\omega_{10} t - i\omega t} + e^{-i\omega_{10} t - i\omega t}\right) dt, \tag{A.4}$$

$$\therefore F(\omega) = \frac{1}{2}\int_{-\infty}^{\infty} e^{-At/2} \cdot \left(e^{-i(\omega - \omega_{10})t} + e^{-i(\omega + \omega_{10})t}\right) dt, \tag{A.5}$$

$$\therefore F(\omega) = \frac{1}{2}\int_{-\infty}^{\infty} \left[e^{[-i(\omega - \omega_{10}) - A/2]t} + e^{[-i(\omega + \omega_{10}) - A/2]t}\right] dt, \tag{A.6}$$

As depopulation of the excited state must begin at a time $t = 0$, the integration limits are modified to become:

$$\therefore F(\omega) = \frac{1}{2}\int_{0}^{\infty} \left[e^{[-i(\omega - \omega_{10}) - A/2]t} + e^{[-i(\omega + \omega_{10}) - A/2]t}\right] dt, \tag{A.7}$$

$$\therefore F(\omega) = \frac{1}{2}\left[\frac{e^{[-i(\omega - \omega_{10}) - A/2]t}}{-i\left(\omega - \omega_{10}\right) - A/2} + \frac{e^{[-i(\omega + \omega_{10}) - A/2]t}}{-i\left(\omega + \omega_{10}\right) - A/2}\right]\Bigg|_{0}^{\infty}, \tag{A.8}$$

$$\therefore F(\omega) = \frac{1}{2}\left[\frac{e^{-[i(\omega-\omega_{10})+A/2]t}}{-i\left(\omega-\omega_{10}\right)-A/2} + \frac{e^{-[i(\omega+\omega_{10})+A/2]t}}{-i\left(\omega+\omega_{10}\right)-A/2}\right]\Bigg|_0^\infty, \tag{A.9}$$

as $e^{-\infty} = 0$ and $e^0 = 1$, when evaluated the expression above becomes:

$$\therefore F(\omega) = -\frac{1}{2}\left[\frac{1}{-i\left(\omega-\omega_{10}\right)-A/2} + \frac{1}{-i\left(\omega+\omega_{10}\right)-A/2}\right], \tag{A.10}$$

$$\therefore F(\omega) = \frac{1}{2}\left[\frac{1}{i\left(\omega-\omega_{10}\right)+A/2} + \frac{1}{i\left(\omega+\omega_{10}\right)+A/2}\right], \tag{A.11}$$

utilising the rotating wave approximation the non-resonant term becomes negligible leading to:

$$F(\omega) \approx \frac{1}{2}\frac{1}{i(\omega-\omega_{10})+A/2}, \tag{A.12}$$

which when multiplied by the complex conjugate gives:

$$|F(\omega)^2| \propto \left(\frac{1}{2}\frac{1}{i(\omega-\omega_{10})+A/2}\right)\cdot\left(\frac{1}{2}\frac{1}{-i(\omega-\omega_{10}+A/2)}\right), \tag{A.13}$$

$$\therefore |F(\omega)^2| \propto \frac{1}{4}\cdot\frac{1}{[i(\omega-\omega_{10})+A/2]\cdot[-i(\omega-\omega_{10})+A/2]}, \tag{A.14}$$

$$\therefore |F(\omega)^2| \propto \frac{1}{4}\cdot\frac{1}{-i^2(\omega-\omega_{10})^2+\frac{i(\omega-\omega_{10})A}{2}-\frac{i(\omega-\omega_{10})A}{2}+(A/2)^2}, \tag{A.15}$$

$$\therefore |F(\omega)^2| \propto \frac{1}{4}\cdot\frac{1}{(A/2)^2+(\omega-\omega_{10})^2}. \tag{A.16}$$

The normalisation condition:

$$\int_{-\infty}^{\infty} g(\omega-\omega_{10})d\omega = \int_{-\infty}^{\infty} g(v-v_{10})dv = 1, \tag{A.17}$$

gives the Lorentzian profile:

$$g(v-v_{10}) = \frac{A}{(A/2)^2+4\pi^2(v-v_{10})^2}, \tag{A.18}$$

using the relation

$$v = 2\pi\omega. \tag{A.19}$$

Bibliography

[1] Cheal B, Flanagan KT. Progress in laser spectroscopy at radioactive ion beam facilities. Journal of Physics G: Nuclear and Particle Physics. 2010;37:113101. Available from: http://dx.doi.org/10.1088/0954-3899/37/11/113101.

[2] Technische Universität Darmstadt. Laser Spectroscopy of Radioactive Isotopes - Survey;. Available from: https://www.ikp.tu-darmstadt.de.

[3] Kondev FG, Wang M, Huang WJ, Naimi S, Audi G. The NUBASE2020 evaluation of nuclear physics properties *. Chinese Physics C. 2021;45:030001. Available from: http://dx.doi.org/10.1088/1674-1137/abddae.

[4] de Laeter JR, Böhlke JK, Bièvre PD, Hidaka H, Peiser HS, Rosman KJR, et al. Atomic weights of the elements. Review 2000 (IUPAC Technical Report). 2003;75:683-800. Available from: https://doi.org/10.1351/pac200375060683.

[5] Garcia Ruiz RF, Bissell ML, Blaum K, Ekstrom A, Frommgen N, Hagen G, et al. Unexpectedly large charge radii of neutron-rich calcium isotopes. Nature Physics. 2016 Feb;12(6):594–598. Available from: http://dx.doi.org/10.1038/nphys3645.

[6] Miller AJ, Minamisono K, Klose A, Garand D, Kujawa C, Lantis JD, et al. Proton superfluidity and charge radii in proton-rich calcium isotopes. Nature Physics. 2019;15:432-6. Available from: https://doi.org/10.1038/s41567-019-0416-9.

[7] Kreim K, Bissell ML, Papuga J, Blaum K, Rydt MD, Ruiz RFG, et al. Nuclear charge radii of potassium isotopes beyond N=28. Physics Letters B. 2014;731:97-102.

[8] Heylen H, Babcock C, Beerwerth R, Billowes J, Bissell ML, Blaum K, et al. Changes in nuclear structure along the Mn isotopic chain studied via charge radii. Physical Review C. 2016 11;94:54321. Available from: https://link.aps.org/doi/10.1103/PhysRevC.94.054321.

[9] Koszorús A, Yang XF, Jiang WG, Novario SJ, Bai SW, Billowes J, et al. Charge radii of exotic potassium isotopes challenge nuclear theory and the magic character of N=32.

Nature Physics. 2021;17:439-43. Available from:
https://doi.org/10.1038/s41567-020-01136-5.

[10] Aufmuth P, Heilig K, Steudel A. Changes in mean-square nuclear charge radii from optical isotope shifts. Atomic Data and Nuclear Data Tables. 1987;37:455-90. Available from: https://www.sciencedirect.com/science/article/pii/0092640X87900283.

[11] Angeli I, Marinova KP. Table of experimental nuclear ground state charge radii: An update. Atomic Data and Nuclear Data Tables. 2013;99:69-95. Available from: https://www.sciencedirect.com/science/article/pii/S0092640X12000265.

[12] Bissell ML, Papuga J, Naïdja H, Kreim K, Blaum K, Rydt MD, et al. Proton-Neutron Pairing Correlations in the Self-Conjugate Nucleus ^{38}K Probed via a Direct Measurement of the Isomer Shift. Physical Review Letters. 2014 7;113:52502. Available from: https://link.aps.org/doi/10.1103/PhysRevLett.113.052502.

[13] Koszorús Vormawah LJ, Beerwerth R, Bissell ML, Campbell P, Cheal B, et al. Proton-neutron pairing correlations in the self-conjugate nucleus ^{42}Sc. Physics Letters B. 2021;819:136439. Available from:
https://www.sciencedirect.com/science/article/pii/S0370269321003798.

[14] Hammen M, Nörtershäuser W, Balabanski DL, Bissell ML, Blaum K, Budinčević I, et al. From Calcium to Cadmium: Testing the Pairing Functional through Charge Radii Measurements of $^{100-130}$Cd. Phys Rev Lett. 2018 Sep;121:102501. Available from: https://link.aps.org/doi/10.1103/PhysRevLett.121.102501.

[15] Gorges C, Rodríguez LV, Balabanski DL, Bissell ML, Blaum K, Cheal B, et al. Laser Spectroscopy of Neutron-Rich Tin Isotopes: A Discontinuity in Charge Radii across the $N = 82$ Shell Closure. Phys Rev Lett. 2019 May;122:192502. Available from: https://link.aps.org/doi/10.1103/PhysRevLett.122.192502.

[16] de Groote RP, Billowes J, Binnersley CL, Bissell ML, Cocolios TE, Day Goodacre T, et al. Measurement and microscopic description of odd–even staggering of charge radii of exotic copper isotopes. Nature Physics. 2020 Apr;16(6):620–624. Available from: http://dx.doi.org/10.1038/s41567-020-0868-y.

[17] Geldhof S, Kortelainen M, Beliuskina O, Campbell P, Caceres L, Cañete L, et al. Impact of Nuclear Deformation and Pairing on the Charge Radii of Palladium Isotopes. Physical Review Letters. 2022 4;128:152501. Available from:
https://link.aps.org/doi/10.1103/PhysRevLett.128.152501.

[18] Geiger H, Rutherford E. The scattering of α-particles by matter. Proceedings of the Royal Society of London Series A, Containing Papers of a Mathematical and Physical Character. 1910 4;83:492-504. Doi: 10.1098/rspa.1910.0038. Available from: https://doi.org/10.1098/rspa.1910.0038.

[19] Rutherford E. LXXIX. The scattering of α and β particles by matter and the structure of the atom. The London, Edinburgh, and Dublin Philosophical Magazine and Journal of Science. 1911 5;21:669-88. Doi: 10.1080/14786440508637080. Available from: https://doi.org/10.1080/14786440508637080.

[20] Krane KS, Halliday D. Introductory Nuclear Physics. Wiley; 1988.

[21] Woods RD, Saxon DS. Diffuse Surface Optical Model for Nucleon-Nuclei Scattering. Phys Rev. 1954 Jul;95:577-8. Available from: https://link.aps.org/doi/10.1103/PhysRev.95.577.

[22] Lilley J. Nuclear Physics : Principles and Applications. John Wiley Sons, Incorporated; 2001. Available from: http://ebookcentral.proquest.com/lib/liverpool/detail.action?docID=1211895.

[23] Mottelson BR, Nilsson SG. Classification of the Nucleonic States in Deformed Nuclei. Phys Rev. 1955 Sep;99:1615-7. Available from: https://link.aps.org/doi/10.1103/PhysRev.99.1615.

[24] Casten RF. The Deformed Shell Model or Nilsson Model. Oxford Academic; 2001.

[25] Nilsson SG. Binding states of individual nucleons in strongly deformed nuclei; 1955. Available from: https://cds.cern.ch/record/212345.

[26] Firestone RB. Table of isotopes. Richard B. Firestone. Virginia S. Shirley, ed 1999 update. 8th ed. A Wiley-Interscience publication. New York: Wiley; 1999.

[27] Navrátil P, Quaglioni S, Hupin G, Romero-Redondo C, Calci A. Unified *ab initio* approaches to nuclear structure and reactions. Physica Scripta. 2016;91:053002. Available from: http://dx.doi.org/10.1088/0031-8949/91/5/053002.

[28] Malbrunot-Ettenauer S, Kaufmann S, Bacca S, Barbieri C, Billowes J, Bissell ML, et al. Nuclear Charge Radii of the Nickel Isotopes $^{58-68,70}$Ni. Physical Review Letters. 2022 1;128:22502. Available from: https://link.aps.org/doi/10.1103/PhysRevLett.128.022502.

[29] Ekström A, Jansen GR, Wendt KA, Hagen G, Papenbrock T, Carlsson BD, et al. Accurate nuclear radii and binding energies from a chiral interaction. Phys Rev C. 2015 May;91:051301. Available from: https://link.aps.org/doi/10.1103/PhysRevC.91.051301.

[30] Somà V, Navrátil P, Raimondi F, Barbieri C, Duguet T. Novel chiral Hamiltonian and observables in light and medium-mass nuclei. Phys Rev C. 2020 Jan;101:014318. Available from: https://link.aps.org/doi/10.1103/PhysRevC.101.014318.

[31] Simonis J, Stroberg SR, Hebeler K, Holt JD, Schwenk A. Saturation with chiral interactions and consequences for finite nuclei. Phys Rev C. 2017 Jul;96:014303. Available from: https://link.aps.org/doi/10.1103/PhysRevC.96.014303.

[32] Hohenberg P, Kohn W. Inhomogeneous Electron Gas. Physical Review. 1964 11;136:B864-71. Available from: https://link.aps.org/doi/10.1103/PhysRev.136.B864.

[33] Colò G. Nuclear density functional theory. Advances in Physics: X. 2020 1;5:1740061. Doi: 10.1080/23746149.2020.1740061. Available from: https://doi.org/10.1080/23746149.2020.1740061.

[34] Colò G. Density Functional Theory (DFT) for atomic nuclei: a simple introduction. arXiv; 2018. Available from: https://doi.org/10.48550/arXiv.1807.02643.

[35] Fayans SA. Towards a universal nuclear density functional. Journal of Experimental and Theoretical Physics Letters. 1998;68:169-74. Available from: https://doi.org/10.1134/1.567841.

[36] Reinhard PG, Nazarewicz W. Toward a global description of nuclear charge radii: Exploring the Fayans energy density functional. Physical Review C. 2017 6;95:64328. Available from: https://link.aps.org/doi/10.1103/PhysRevC.95.064328.

[37] Laatiaoui M, Lauth W, Backe H, Block M, Ackermann D, Cheal B, et al. Atom-at-a-time laser resonance ionization spectroscopy of nobelium. Nature. 2016;538:495-8. Available from: https://doi.org/10.1038/nature19345.

[38] Smith PL, Heise C, Esmond JR, Kurucz RL. Atomic Spectral Line database; 1995. Available from: https://lweb.cfa.harvard.edu/amp/ampdata/kurucz23/sekur.html.

[39] Kramida A, Ralchenko Y, Reader J, NIST ASD Team. NIST Atomic Spectra Database; 2021. Available from: https://lweb.cfa.harvard.edu/amp/ampdata/kurucz23/sekur.html.

[40] Buchmann AJ, Henley EM. Intrinsic quadrupole moment of the nucleon. Physical Review C. 2000 dec;63(1). Available from: https://doi.org/10.1103

[41] Campbell P, Moore ID, Pearson MR. Laser spectroscopy for nuclear structure physics. Progress in Particle and Nuclear Physics. 2016;86:127-80. Available from: https://www.sciencedirect.com/science/article/pii/S0146641015000915.

[42] Cheal B, Gardner MD, Avgoulea M, Billowes J, Bissell ML, Campbell P, et al. The shape transition in the neutron-rich yttrium isotopes and isomers. Physics Letters B. 2007;645:133-7. Available from: https://www.sciencedirect.com/science/article/pii/S037026930601608X.

[43] Berengut JC, Dzuba VA, Flambaum VV. Isotope-shift calculations for atoms with one valence electron. Phys Rev A. 2003 Aug;68:022502. Available from: https://link.aps.org/doi/10.1103/PhysRevA.68.022502.

[44] Billowes J, Campbell P. High-resolution laser spectroscopy for the study of nuclear sizes and shapes. Journal of Physics G: Nuclear and Particle Physics. 1995;21:707-39. Available from: http://dx.doi.org/10.1088/0954-3899/21/6/003.

[45] Huang WJ, Wang M, Kondev FG, Audi G, Naimi S. The AME 2020 atomic mass evaluation (I). Evaluation of input data, and adjustment procedures*. Chinese Physics C. 2021;45:030002. Available from: https://dx.doi.org/10.1088/1674-1137/abddb0.

[46] King WH. Isotope Shifts in Atomic Spectra. Springer US; 1984. Available from: https://doi.org/10.1007/978-1-4899-1786-7.

[47] Bernath PF. Spectra of atoms and molecules. Oxford University Press; 2015.

[48] Rybicki GB, Lightman AP. Radiative processes in astrophysics / George B. Rybicki, Alan P. Lightman. Wiley-VCH; 2004. Includes bibliographical references and index.

[49] Vitanov NV, Shore BW, Yatsenko L, Böhmer K, Halfmann T, Rickes T, et al. Power broadening revisited: theory and experiment. Optics Communications. 2001;199:117-26.

[50] Hill C. Learning Scientific Programming with Python. Cambridge University Press; 2020.

[51] University of Jyväskylä. IGISOL;. Available from: https://www.jyu.fi/science/en/physics/research/infrastructures/accelerator-laboratory/nuclear-physics-facilities/the-exotic-nuclei-and-beams.

[52] Karvonen P, Moore ID, Sonoda T, Kessler T, Penttilä H, Peräjärvi K, et al. A sextupole ion beam guide to improve the efficiency and beam quality at IGISOL. Nuclear Instruments and Methods in Physics Research Section B: Beam Interactions with Materials and Atoms. 2008;266:4794-807. Available from: https://www.sciencedirect.com/science/article/pii/S0168583X08009191.

[53] Vilén M, Canete L, Cheal B, Giatzoglou A, de Groote R, de Roubin A, et al. A new off-line ion source facility at IGISOL. Nuclear Instruments and Methods in Physics

Research Section B: Beam Interactions with Materials and Atoms. 2020;463:382-3. Available from: https://www.sciencedirect.com/science/article/pii/S0168583X19302344.

[54] Nieminen A, Campbell P, Billowes J, Forest DH, Griffith JAR, Huikari J, et al. Cooling and bunching of ion beams for collinear laser spectroscopy. Nuclear Instruments and Methods in Physics Research Section B: Beam Interactions with Materials and Atoms. 2003;204:563-9. Available from: https://www.sciencedirect.com/science/article/pii/S0168583X0202133X.

[55] Vormawah LJ, Vilén M, Beerwerth R, Campbell P, Cheal B, Dicker A, et al. Isotope shifts from collinear laser spectroscopy of doubly charged yttrium isotopes. Phys Rev A. 2018 Apr;97:042504. Available from: https://link.aps.org/doi/10.1103/PhysRevA.97.042504.

[56] Anton KR, Kaufman SL, Klempt W, Moruzzi G, Neugart R, Otten EW, et al. Collinear Laser Spectroscopy on Fast Atomic Beams. Phys Rev Lett. 1978 Mar;40:642-5. Available from: https://link.aps.org/doi/10.1103/PhysRevLett.40.642.

[57] Sirah. Mattise Users Guide Version 1.8;. Available from: https://www.spectra-physics.com/mam/celum/celum_assets/sp/resources/Matisse_Users_Guide_Rev_18.pdf.

[58] Sirah. Datasheet Mattise 2 TS; 2020. Available from: https://www.sirah.com/wp-content/uploads/2021/01/Matisse-2-TS.pdf.

[59] Boyd RW. Nonlinear Optics. Elsevier Inc.; 2003. Available from: https://doi.org/10.1016/B978-0-12-121682-5.X5000-7.

[60] Furmann B, Jarosz A, Stefańska D, Dembczyński J, Stachowska E. Isotope shift in chromium. Spectrochimica Acta Part B: Atomic Spectroscopy. 2005;60:33-40. Available from: https://www.sciencedirect.com/science/article/pii/S058485470400285X.

[61] Ghilani CD, Wolf PR. Adjustment Computations: Spatial Data Analysis, Fourth Edition. Wiley; 2006.

[62] @PostcardProfessor. Nonlinear Least Squares; 2019. Available from: https://youtu.be/8evmj2L-iCY.

[63] de Groote RP, de Roubin A, Campbell P, Cheal B, Devlin CS, Eronen T, et al. Upgrades to the collinear laser spectroscopy experiment at the IGISOL. vol. 463; 2020. p. 437-40. Available from: https://www.sciencedirect.com/science/article/pii/S0168583X19302125.

[64] Bodnar O, Elster C. On the adjustment of inconsistent data using the Birge ratio. Metrologia. 2014;51:516. Available from: https://dx.doi.org/10.1088/0026-1394/51/5/516.

[65] Mertzimekis TJ, Stamou K, Psaltis A. An online database of nuclear electromagnetic moments. Nuclear Instruments and Methods in Physics Research Section A: Accelerators, Spectrometers, Detectors and Associated Equipment. 2016;807:56-60. Available from: http://www.sciencedirect.com/science/article/pii/S0168900215013352.

[66] Ertmer W, Johann U, Mosmann R. Measurement of the nuclear quadrupole moment of ^{53}Cr by laser-Rf double resonance. Zeitschrift für Physik A Atoms and Nuclei. 1982;309:1-4. Available from: https://doi.org/10.1007/BF01420143.

[67] Childs WJ, Goodman LS, von Ehrenstein D. Magnetic Hyperfine Interaction of Cr^{53}. Phys Rev. 1963 Dec;132:2128-35. Available from: https://link.aps.org/doi/10.1103/PhysRev.132.2128.

[68] Fricke G, Heilig K. Nuclear Charge Radii · 24-Cr Chromium: Datasheet from Landolt-Börnstein - Group I Elementary Particles, Nuclei and Atoms · Volume 20: "Nuclear Charge Radii" in Springer Materials. Schopper H, editor. Springer-Verlag Berlin Heidelberg;. Copyright 2004 Springer-Verlag Berlin Heidelberg. Available from: https://doi.org/10.1007/10856314$_2$6).

[69] Heilig K, Wendlandt D. Isotope shift in Cr I. Physics Letters A. 1967;25:277-8. Available from: https://www.sciencedirect.com/science/article/pii/0375960167909036.

[70] Kortelainen M, Sun Z, Hagen G, Nazarewicz W, Papenbrock T, Reinhard PG. Universal trend of charge radii of even-even Ca–Zn nuclei. Physical Review C. 2022 2;105:L021303. Available from: https://link.aps.org/doi/10.1103/PhysRevC.105.L021303.

[71] Hemalatha M. Nuclear charge radii of $^{46-62}$Cr isotopes and reaction cross sections for p-Cr. Physical Review C. 2022 11;106:54607. Available from: https://link.aps.org/doi/10.1103/PhysRevC.106.054607.

[72] Charlwood FC, Billowes J, Campbell P, Cheal B, Eronen T, Forest DH, et al. Ground state properties of manganese isotopes across the N=28 shell closure. Physics Letters B. 2010;690:346-51. Available from: https://www.sciencedirect.com/science/article/pii/S0370269310006520.

[73] Blaum K, Geithner W, Lassen J, Lievens P, Marinova K, Neugart R. Nuclear moments and charge radii of argon isotopes between the neutron-shell closures N=20 and N=28.

Nuclear Physics A. 2008;799:30-45. Available from:
https://www.sciencedirect.com/science/article/pii/S0375947407007841.

[74] Gangrsky YP, Marinova KP, Zemlyanoi SG, Moore ID, Billowes J, Campbell P, et al. Nuclear charge radii of neutron deficient titanium isotopes ^{44}Ti and ^{45}Ti. Journal of Physics G: Nuclear and Particle Physics. 2004;30:1089. Available from:
https://dx.doi.org/10.1088/0954-3899/30/9/009.